NASA Technical Memorandum105556

Evaluation of an Innovative High Temperature Ceramic Wafer Seal for Hypersonic Engine Applications

Bruce M. Steinetz
Lewis Research Center
Cleveland, Ohio

February 1992

NASA

EVALUATION OF AN INNOVATIVE HIGH TEMPERATURE CERAMIC WAFER SEAL FOR HYPERSONIC ENGINE APPLICATIONS

Bruce M. Steinetz
National Aeronautics and Space Administration
Lewis Research Center
Cleveland, Ohio 44135

ABSTRACT

A critical mechanical system in advanced hypersonic engines is the panel-edge seal system that seals gaps between the articulating engine panels and the adjacent engine splitter walls. Significant advancements in seal technology are required to meet the extreme demands placed on the seals, including the simultaneous requirements of low leakage, conformable, high temperature, high pressure, sliding operation. In this investigation, the design, development, analytical and experimental evaluation of a new ceramic wafer seal that shows promise of meeting these demands will be addressed.

A high temperature seal test fixture was designed and fabricated to measure static seal leakage performance under engine simulated conditions. Ceramic wafer seal leakage rates are presented for engine-simulated air pressure differentials (up to 100 psi), and temperatures (up to 1350 °F), sealing both flat and distorted wall conditions, where distortions can be as large as 0.15 in. in only an 18 in. span. Seal leakage rates are low, meeting an industry-established tentative leakage limit

for all combinations of temperature, pressure and wall conditions considered. A seal leakage model developed from externally-pressurized gas film bearing theory is also presented. Predicted leakage rates agree favorably with the measured data for nearly all combinations of temperature and pressure. Discrepancies noted at high engine pressure and temperature are attributed to thermally-induced, non-uniform changes in the size and shape of the leakage gap condition.

The challenging thermal environment the seal must operate in places considerable demands on the seal concept and material selection. Of the many high temperature materials considered in the design, ceramics were the only materials that met the many challenging seal material design requirements. Of the aluminum oxide, silicon carbide, and silicon nitride ceramics considered in the material ranking scheme developed herein, the silicon nitride class of ceramics ranked the highest because of their high temperature strength; resistance to the intense heating rates; resistance to hydrogen damage; and good structural properties.

Baseline seal feasibility has been established through the research conducted in this investigation. Recommendations for future work are also discussed.

TABLE OF CONTENTS

TABLE OF CONTENTS

LIST OF FIGURES

Chapter 1

Chapter 2

LIST OF TABLES

CHAPTER 1

1. INTRODUCTION

Key to the development of a single stage earth-to-orbit vehicle is an advanced propulsion system that must be integrally designed with the vehicle airframe as conceptually shown in Figure 1.1. To maintain sufficiently high specific impulse and reach orbital velocity (Mach 25) hydrogen-burning, ramjet/scramjet engines such as shown in Figure 1.2 are being developed. To prevent the extremely hot, pressurized engine flow path gases from escaping past the movable panels (see Fig. 1.2), high temperature, flexible, sliding seals are required around the perimeter of the moving panels. Panel-edge seals, the focus of this investigation are required along both sides of the movable panels extending the length (≈20 ft) of the engine.

Engine chamber temperatures and pressures vary significantly with axial engine station, vehicle speed, engine cycle and fuel-to-air ratio. Calculations have shown that at a Mach 6 flight condition engine pressure differentials can reach 100 psi with engine static temperatures higher than 5000 °F. These conditions illustrate the severe aero-thermal environment in which the seals must operate.

Complicating the sealing challenge further is the need for the panel-edge seals to seal against severely distorted engine sidewalls. The high heating rates and pressures of hypersonic flight can cause the weight-minimized engine sidewalls to deflect in some cases upwards of 0.15 in. Minimizing leakage past the movable panels requires that the panel-edge seals be sufficiently compliant and preloaded to seal against the engine wall curvature.

BACKGROUND ON HIGH TEMPERATURE SEALS

Only a few references are made in the literature to high-temperature (>1000 °F), compliant, sliding seals. Much of the applicable high temperature seal technology has been developed for turbojet two-dimensional convergent/divergent nozzles. High-excursion nozzle seals were designed and successfully tested as part of the Augmented Deflector Exhaust Nozzle (ADEN) program, (Ref. 1.1). In this nozzle, the convergent/divergent flap edge seals shown in Figure 1.3 sealed pressure differentials between 20 to 30 psi with calculated sidewall deflections of the order of 0.030 in. and engine flow-path total temperatures as high as 3300 °F. The seals were cooled by a cover gas that maintained estimated seal metal

(Inconel 718) temperatures below 1200 °F. An excellent review of variable geometry nozzle seals and nozzle seal technology is given by Kuchar in Reference 1.2.

A novel exhaust nozzle hinge seal developed under an Air Force contract (Ref. 1.3) permits operation at higher chamber pressures than previously possible while maintaining significant distortion capabilities. In this bimetallic seal arrangement, two metal layers are bonded together so that their differing rates of thermal expansion cause the seal to bend in a preferred direction when heated by exhaust gases. Using a bonded nickel-alloy/stainless steel construction that allows the seal to be twice as thick and operate up to 50 psi chamber pressures, this seal can accommodate deflections up to 0.050 in. with a temperature rise of 1000 °F.

Nozzle panel-edge seals for a hydrogen-burning ramjet engine were designed by the author and successfully tested at NASA Lewis Research Center. The design consisted of a wavespring-preloaded, pressure-actuated edge clip seal made of superalloy sheet metal (RENE '41) capable of deforming 0.06 in. to seal against the distorted engine sidewalls. The seals operated successfully for over 150 hot, short-duration engine

firings with measured seal temperatures of nearly 1000 °F and pressure differentials up to 12 psi.

Reference 1.4 contains analytical and experimental investigations of advanced seal concepts developed for hypersonic airframe control surfaces and engine inlets. And finally, Reference 1.5 describes four hypersonic engine seal concepts and presents experimental leakage measurements which serves as the basis for the current investigations.

HYPERSONIC ENGINE SEAL DESIGN REQUIREMENTS

One of the paramount design concerns of hypersonic engine seal designers is to prevent hot engine flowpath gases and potentially explosive hydrogen-oxygen mixtures from escaping behind the seal systems and damaging the engine panel support and articulation systems. There are several design philosophies in sealing the engine chamber, each having its advantages and disadvantages. The first approach is to attempt to completely seal the engine chamber preventing any flowpath gases from getting behind the articulating engine panel-edge and -hinge seals. This is considered a high risk approach since the

seals must be virtually leak-tight under all circumstances.

The second more conservative approach is the balanced-pressure method in which the cavity behind the movable engine panels is pressurized slightly above engine flowpath pressures. In this approach, the cavity behind the horizontal engine panel and ceramic wafer seal shown in Figure 1.4 would be pressurized at a pressure 10 to 15 psi above the local engine flow path pressure. In this arrangement, the seals limit purge-gas flow. The purge flow gas that does get by the seals cools them. Because the pressure differentials across the movable panels are held to a minimum, the pressure loads the seals must support are greatly reduced. The advantages cited come with a cost, however. The purge system requires separate pressurized zones behind the movable engine panels adding the weight and complexity of zone partitions that articulate with the engine panels, and the plumbing and pressure control systems.

A third hybrid approach combines features of both of these previous approaches. Using a dual seal system as shown in Figure 1.5, the cavity between the two seals is positively pressurized with an inert gas at a pressure

above the local axial engine pressure. This positive purge not only inerts the seal area and prevents leakage of the potentially explosive mixtures from getting behind the seals, but the purge can also be used to effectively cool the seal. A positive purge was analytically shown in Reference 1.6 to effectively cool the ceramic wafer seal even under the intense engine heating rates of Mach 10 flight. Using this third approach, the heavy and complex backside partitioning system is eliminated. Final selection between these general sealing approaches will be based on criteria such as minimum weight and complexity and maximum reliability while satisfying the specific seal design criteria.

Only preliminary estimates have been made for many of the specific panel-edge seal design criteria. Some of these first order estimates are listed below and indicate some of the major seal development issues that must be addressed.

SEAL DESIGN CRITERIA

1. Minimize seal leakage (industry established estimates, Ref. 1.5, have indicated a tentative leakage limit of 0.004 lb/s-ft of seal).

2. Operate in the high (200-1500 Btu/sq-ft-sec) heat flux environment utilizing minimum coolant resources.

3. Conform to and seal against distorted adjacent engine walls (0.15 in. deflection in an 18 in. span).

4. Sustain minimal sliding damage over engine life (estimated sliding distance is of the order of 10^4 to 10^5 in.).

5. Require minimal actuation forces to overcome seal drag forces.

6. Integrate easily with panel-hinge seals forming a continuous seal across the hinge.

7. Maintain material stability in the chemically hostile hydrogen-oxygen environment.

SEAL DESIGN

The wafer seal considered in this study is mounted in seal channels on the sides of the articulating engine panels and is actively preloaded against the engine sidewalls. Depending on which general seal approach is selected, the seals either minimize engine flow-path gas leakage behind the movable engine panels or minimize loss of the balanced-pressure purge gas into the engine flowpath. At engine stations where anticipated temperatures exceed the maximum-use temperature of the seal material, some form of active cooling such as film or transpiration cooling must be used to maintain the seal at an acceptable operating temperature.

The ceramic wafer seal shown in Figure 1.4 is made of stacked ceramic wafers mounted in a seal channel along the edge of the movable engine panel. The seal conforms to engine wall distortions by relative sliding of adjacent wafers. Various techniques can be used to transversely preload the ceramic wafers against the engine wall. In this figure a series of actively-cooled, pressurized metal bellows forces the wafers to follow the serpentine-distorted engine sidewall. The ceramic wafer

material, size, shape, and tolerances are described in detail in the future chapters of this report.

The present dissertation consists of three "complete" studies related to the design, development, analytical and experimental evaluation of the ceramic wafer engine seal. Chapter 2 describes the development of a unique high temperature test fixture for evaluating the performance of the wafer seal under engine-simulated pressure differentials and temperatures, sealing flat and distorted engine walls. As will be discussed, there are many common design issues in developing advanced high temperature seal test fixtures and implementing the seal into advanced heat engines.

In Chapter 3, the high temperature leakage performance of the seal is assessed using the high temperature test rig. A leakage rate data-base is presented for the seal sealing engine pressures up to 100 psi, temperatures up to 1350 °F, sealing both flat and distorted engine sidewalls. A flow model is developed that relates leakage flow to engine pressure differential, gas properties, gap conditions, and seal geometry.

Chapter 4 describes high temperature engine seal material design criteria and examines the "performance" of a broad range of high temperature materials relative to these criteria. A material ranking scheme is developed and applied to the final qualifying class of high temperature materials, engineered ceramics. The ranking scheme allows designers to objectively select amongst commercially available ceramic materials, the one having the best balance of high temperature properties as applied to hypersonic engine seal design. The results of the material trade-study provides valuable guidance for material selection for final development of the ceramic wafer engine seal.

REFERENCES FOR CHAPTER 1

1.1 "Advanced V/STOL Propulsion Component Development: Nozzle Deflector Final Report," R77AEG441-VOL-1, General Electric, Aug. 1977. (Avail. NTIS, AD-B021511L.)

1.2 Kuchar, A.P., "Variable Convergent-Divergent Exhaust Nozzle Aerodynamics," Aircraft Propulsion Systems Technology and Design, Oates, G.C. editor, American Institute of Aeronautics and Astronautics, Inc., Washington, DC, pp. 301-338 (1989).

1.3 Holowach, J. and Lee, G.D., "Bimetallic Air Seal for Exhaust Nozzles," U.S. Patent 4,813,608 (1989).

1.4 Dursch, H.W., Nedervelt, P.D. Newquist, C.W., and Burns R.A., "National Aerospace Plane (NASP) Airframe Technology Option Five, Sealing Concepts," D180-31720-1, Boeing Advanced Systems, July 21, 1989.

1.5 Steinetz, B.M., DellaCorte, C., Sirocky, P.J., "On The Development of Hypersonic Engine Seals," NASA TP-2854 (1988).

1.6 Tong, M., and Steinetz, B.M., "Thermal and Structural Assessments of a Ceramic Wafer Seal in Hypersonic Engines," NASA TM-103651 (1990).

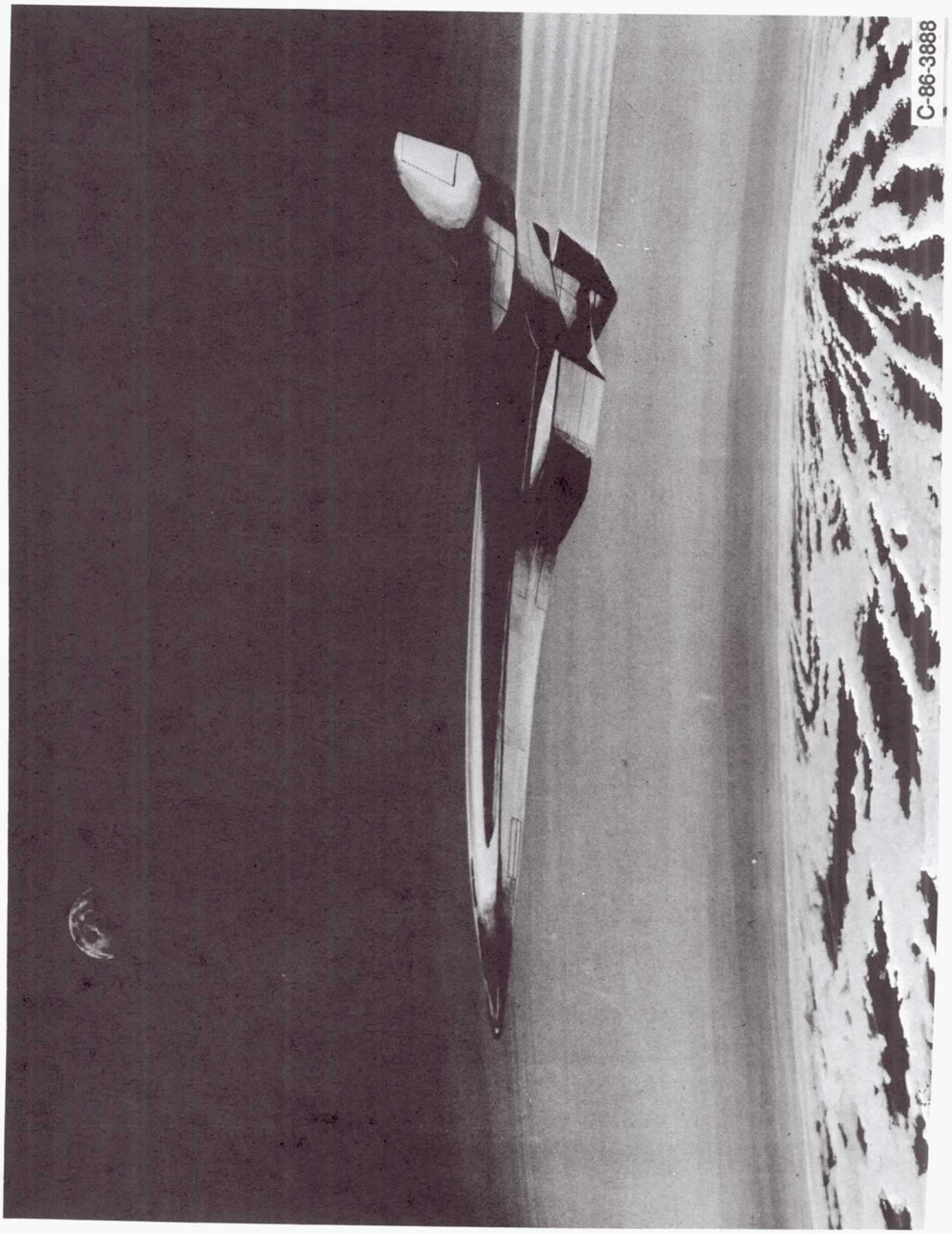

Figure 1.1.—Hypersonic vehicle powered by ramjet/scramjet engines.

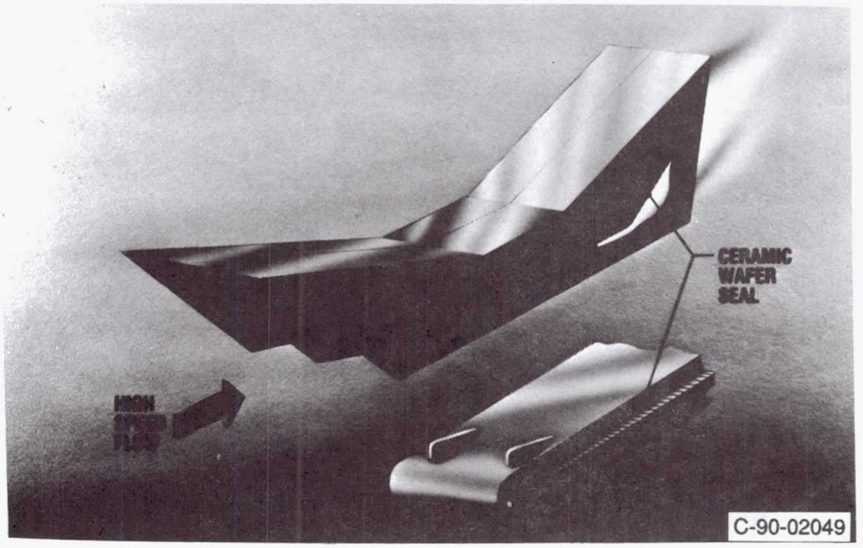

Figure 1.2.—Schematic of hypersonic engine showing the integrated articulating engine panels and panel-edge seal.

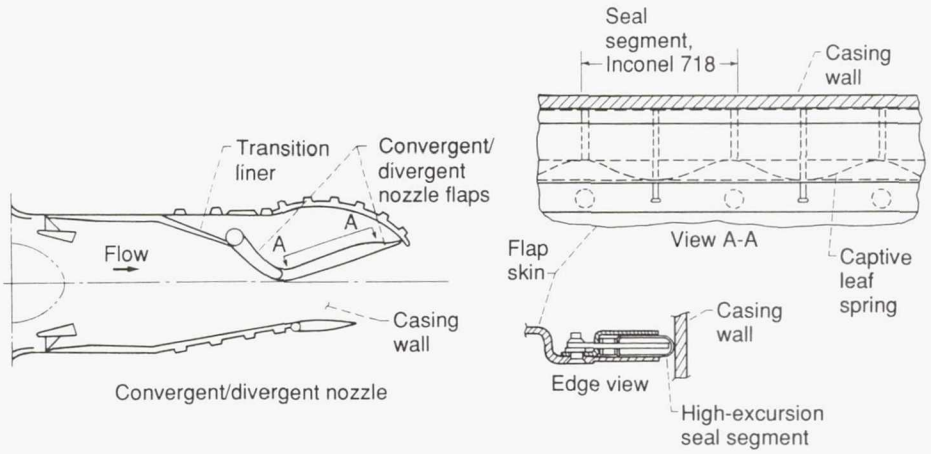

Figure 1.3.—Advanced fighter jet two-dimensional converging/diverging nozzle and seals.

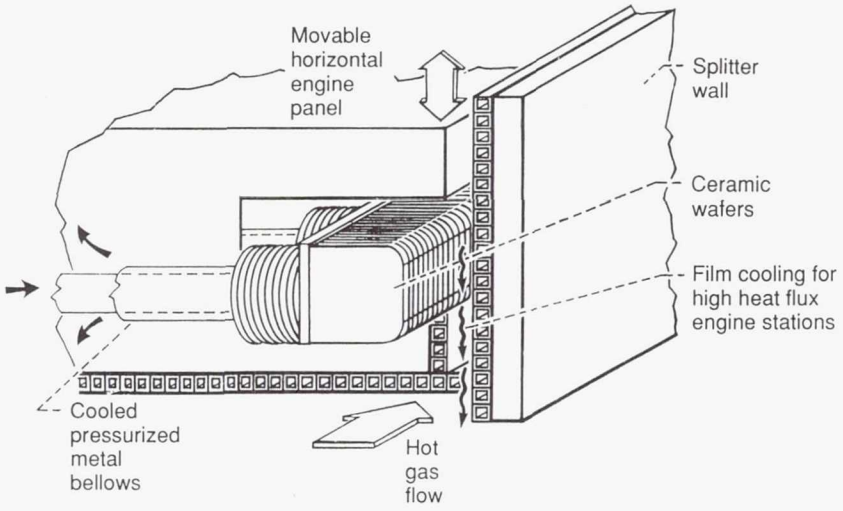

Figure 1.4.—Isometric of ceramic wafer engine seal installed in the articulating engine panel.

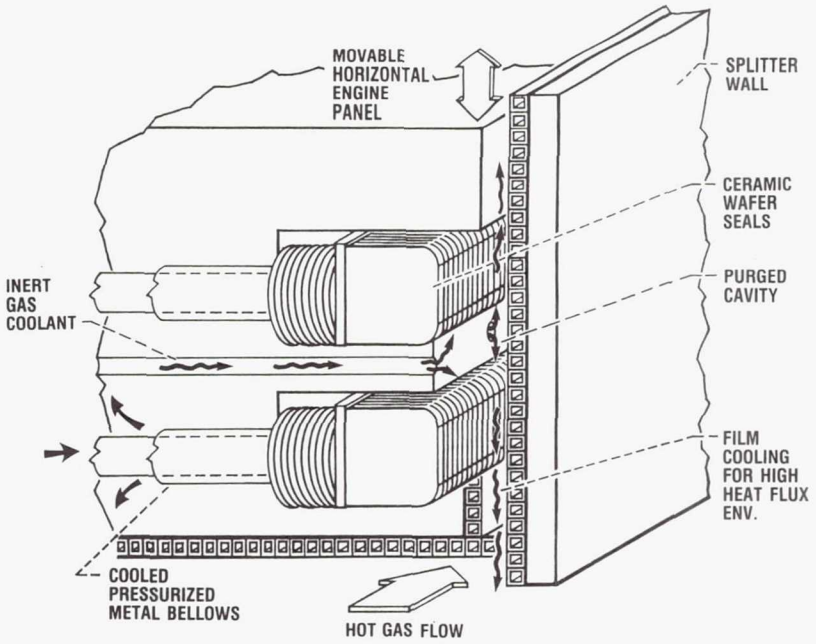

Figure 1.5.—Isometric of dual ceramic wafer engine seals with central positive purge.

CHAPTER 2

2. A TEST FIXTURE FOR MEASURING HIGH-TEMPERATURE HYPERSONIC ENGINE SEAL PERFORMANCE

INTRODUCTION

The seal design requirements of advanced propulsion systems including hypersonic engines being considered for the National Aerospace Plane and advanced two-dimensional, vectored-thrust turbojet fighter engines are challenging. The simultaneous requirements to operate hot while sealing combustion temperature gases with minimal coolant requires advanced design concepts combined with high temperature materials technology. The performances of these key mechanical components must be evaluated using advanced test techniques such as will be described herein, prior to costly engine testing.

Seal concepts being developed for the National Aerospace Plane (NASP) engine are required to seal the many linear feet of gaps between the movable engine panels and the stationary engine sidewalls or splitter walls. These panel-edge seals must prevent the extremely hot, pressurized flow-path gases from escaping past the movable engine panels. Engine performance calculations made in Reference 2.1 determined that the seals must seal static gas temperatures ranging from 600 °F to over

5000 °F, while sealing pressure differentials up to 100 psi. Further complicating the seal's task is the need to accommodate and seal engine-sidewall lateral distortions as large as 0.15 in. in only 18 in. of span.

The objective of this chapter is to describe the key design features of a new high temperature linear seal test fixture at NASA Lewis Research Center developed to characterize engine seal performances under conditions of controllable high temperatures and pressures; preloads; and engine sidewall conditions. Some representative seal performance data are included by way of example.

SEAL RIG DESIGN CRITERIA AND OBJECTIVES

A test rig has been built to address the following important engine seal technology development issues:

1. Measure seal leakage rates under engine-simulated gas temperatures ranging from room temperature to 1500 °F, and pressure differentials ranging from 0 to 100 psi.

2. Characterize the sensitivity of seal leakage to lateral seal preload (from 0 to 80 psi contact

pressure) and to variable axial preload, (from 0 to 100 lb).

3. Characterize seal sensitivity to important seal-design and materials issues such as differences in coefficients of thermal expansion between the seal and the engine panel.

4. Evaluate seal-to-engine panel integration techniques including methods of minimizing seal end leakage.

5. Validate seal leakage flow models at high temperatures.

DESCRIPTION OF SEAL TEST FIXTURE

Seals that are nominally three foot long are tested in the test fixture shown in Figure 2.1. The test seal is mounted in a closely mating seal channel nominally 0.50 in. high as shown in the figure cross section. The seals are preloaded from behind using a series of high temperature Inconel bellows that force the seal against the engine-simulated sidewall that is removed for clarity

in the schematic. Engine gases are simulated by the introduction of heated, pressurized air from below.

Heated Gas Supply: Air or inert gas is heated by in-line electric resistance heaters and supplied to the rig plenum chamber prior to impinging on the candidate test seal. A 0.5 in. square ceramic wafer seal is shown in the figure for illustrative purposes. Up to three parallel input flow-paths (see base of test rig in Fig. 2.1) are used to accommodate the considerable range of flows anticipated for the various seal concepts to be tested. Each parallel leg can deliver 0.03 lb/s flow at 1500 °F for a total of 0.09 lb/s flow. Using shop air supply, pressure differentials up to 100 psi can be applied.

To prevent an over temperature condition in the in-line heaters for the low flows expected for some of the candidate seals, several preventive measures are taken. A low flow alarm and shut-down sequence is used in the control system to kill power to the heaters in the event that flow goes below a preset minimum. Second, the air heater control system incorporates an over-temperature alarm system that kills power to the heaters if exhaust temperatures get too high. The thermocouple used to

sense this temperature is placed close to the heater exhaust. And finally an electrically-isolated thermocouple is placed in contact with the heating element in each stage of the heaters, as shown in Figure 2.2. If the coil temperature exceeds a predetermined "redline" temperature, power is automatically killed to the heater preventing a run-away condition. The thermocouple is electrically isolated by potting it in a thin-wall alumina sleeve. The whole assembly is inserted and sealed in the heater using a pressure-tight fitting.

Surface Mount Heaters: High watt-density conduction heaters are strapped on to the top and bottom of the test rig. Three 3.5 kW heaters are used to ramp the rig temperature up to the desired test temperature using a digital ramp-soak controller. Due to the efficiency of thermal-conduction, these surface heaters supply most of the heat to the rig during heat-up. Employing surface heaters on the top and bottom minimize the thermal gradients and any unnecessary thermal distortions through the 5.5 in. high Inconel test fixture.

When heating the test rig, a ramp-soak profile is followed that prevents the surface heater temperatures

from exceeding the rig bulk temperature by more than 200 °F. A typical temperature-time heating profile for the rig using both surface and air heaters is shown in Figure 2.3. The test fixture is heated to 1500 °F in just over 5 hr.

Rig Insulation: To achieve the high test temperatures, the test rig is insulated with a high temperature, low conductivity (1 Btu/ft-hr-°F) board insulation. As shown in Figure 2.4, 2 in. thick alumina insulating board is fitted closely around the outside of the rig with no gaps or spaces. The front wall of the rig and its insulating board are removed here for clarity.

Leakage Measurement: Leakage rates are measured upstream of the in-line heaters. Leakage is measured in this manner for several reasons. Measuring the mass flow prior to heating to 1500 °F precludes the need to pre-cool the gas before measuring it with room temperature flowmeters. Eliminating the need to capture the leaked gas and then pre-cool it saves considerable expense and complexity. Measuring the leakage flow upstream of the seal also gives a conservative estimate of the actual seal leakage rate. The leakage rate that is measured

includes both the seal leakage and any trace leakage at various connections in the rig and around the seal ends.

To qualify the seal integrity of the large threaded joints and the high temperature thread sealing-compound used, a simple experiment was conducted. A pressurized rubber bladder was installed in place of the test seal. As the engine pressure was applied each of the threaded joints was leak-checked with a soap solution. Each joint checked-out successfully.

Pressure Measurement: The pressure differential applied across the seal is evaluated using pitot static pressure taps immediately upstream of the seal. Gage pressure measurements are used since the seal vents to atmospheric conditions and the exiting flow velocities are low. The pressures are measured using solid-state capacitance type transducers. Pressure is supplied to the transducers using suitably long (>7 in.) tubing, to prevent high temperatures from reaching the transducer. Measurements are taken at multiple axial stations so an accurate average pressure differential is obtained.

Pressures are also measured in the seal cavity behind the seal to determine fluid forces exerted by the simulated

engine chamber pressure on the backside of the seal. Pressure supplied to the lateral preload bellows is also measured, from which a seal contact stress is calculated.

Temperature Measurement: Gas temperatures impinging on the seal are measured using fast-acting open-bead thermocouples just upstream of the seal. The thermocouple beads are inserted in the gas stream to measure true gas temperature. For averaging purposes, multiple thermocouples are used along the length of the 3 ft seal. Thermocouples are also placed at the exhaust of the heaters. Temperature readings from these thermocouples are used in independent feedback control circuits for each of the heaters.

Key hardware temperatures such as the seal, the Inconel metal bellows, and the rig bulk temperature are also measured using thermocouples. In all cases, type K (Chromel-Alumel; 2000 °F) thermocouples are used. Wherever thermocouples or pitot static pressure taps are inserted into the pressurized rig special high temperature fittings are used to prevent parasitic leakage. These fittings are made by Conax Co.[1] and use a

---

[1] Note: Mention of manufacturers is made only for reference purposes and does not constitute a product endorsement by NASA or the U.S. Government.

proprietary fitting design with magnesium-oxide (lava) type glands capable of 1800 °F operation.

Seal Preload and Measurement: An important parameter requiring investigation is the seal preload required to adequately seal the pressurized gas. Both lateral preload (e.g., transverse to the seal axis) and axial preload are measured in the rig. Lateral preload is applied using series of welded-leaf, flexible Inconel 718 metal bellows (see Fig. 2.5). These 0.5 in. diameter bellows are mounted on 1.0 in. centers and are pressurized from a common manifold. In-line with each of the bellows pressure supply tube is a hand valve (not shown) that can be used to select the number of active bellows.

A thin (0.03 in. thick) strip of Inconel is placed between the nose of the sealed bellows and the back of the candidate seal. This strip distributes the preload to portions of the seal between the bellows. An average seal contact pressure is determined by pro-rating bellows pressure (as measured in the manifold supply) by the ratio of the bellows area to the backside seal area. If all of the bellows are active the average contact pressure is two-fifths the bellows supply pressure.

Axial preload is applied using specially designed actuators located at both ends of the rig that are on center with the seal axis. A key component of this system, is the large-stroke, hermetically-sealed axial preloader shown in Figure 2.6(a) and 2.6(b). This bellow/piston arrangement was designed to several key design criteria, including: 1. allow axial motion up to 0.35 in. per side to accommodate differential expansion between the ceramic seal and the metal rig; 2. prevent any axial leakage out of the rig; and 3. transmit compressive or tensile preloads up to 100 lb without significant frictional losses or hysteresis.

As shown in the cross section, the piston push rod end is welded to the inside closed end of the bellows. The outer diameter of the Inconel 718 bellows is welded to the Inconel outer tube. The Inconel outer tube then is mated to the rig using the Conax type fitting. The Inconel push rod is piloted in a hole on center line of the seal and lubricated with a light coating of high temperature boron nitride solid lubricant to minimize frictional drag.

The seal is preloaded from both ends instead of just one to minimize the effects of friction between the seal and

the seal channel. In other words, force applied to the end of the seal is continuously reacted by friction forces as one moves axially down the seal. Using two actuators in essence cuts in-half the total accumulated friction that each actuator must overcome.

A 100 lb pneumatic piston exerts the axial load on the preload system through a calibrated load cell mounted in the load train. Engine pressure exerted internally on the bellows results in a force that must be subtracted out when recording the axial load applied to the end of the seal. All of the measurements made on the test rig are displayed on a computer screen and electronically stored on computer disks for future interpretation.

End Leakage Control: Unlike circular seals, linear seals unavoidably have two ends. Treatment of the ends is critical to obtaining accurate measurement of the seal's leakage performance. Based on experience with previous rig designs, end leakage can virtually be eliminated by "building-in" the ends of the seal into the test rig. As shown in Figure 2.1, 1 in. of seal on both ends extends beyond the 3 ft test zone. In these built-in ends, there is no inter-panel gap (0.20 in.) that the seal must seal. The face of the rig and the seal are both flush with the

cover plate. The seal is firmly preloaded against the cover plate with the lateral bellows preload system that are also in these end regions. The leakage follows the path of least resistance which is the center 3 ft test zone. If there is any trace leakage from the end cavities, its effects are minimized by testing the long 3-ft test lengths and calculating an average leakage rate in terms of leakage rate per unit seal length.

Adjacent Wall Condition: A simple method of prescribing various wall conditions is used in the rig. A front wall or cover plate is made with two precision machined surfaces. One side is finished flat overall. Bolting this side toward the seal results in an inter-panel gap width of 0.20 in. over the full three foot length, (accounting for the thin ≈0.016 in. high temperature head gasket). The opposite side has a sinusoidal wave machined onto it. The wave bulges inward toward the seal with a peak of 0.150 in. at the center (see Fig. 2.1). When bolted against the seal, the inter-panel gap width is 0.05 in. at the center sinusoidally increasing to the full 0.20 in. at both ends. The flow area for the straight gap condition is 7.2 in^2. The flow area for the wavy wall condition is 4.5 in^2.

DESIGN FOR HIGH TEMPERATURE SERVICE

Designing test fixtures for elevated temperature operation requires attention to be paid to certain design elements not often required for conventional design. For instance the rig must be properly sized to meet safety criteria of high temperature pressure vessels. Also allowances must be made for the significant growths that will occur as the fixture heats to the operating temperatures. Provisions must also be made to disassemble any threaded fasteners following high temperature service.

Stress Analysis: In sizing the test fixture, a finite element stress analysis of the test rig was performed. The loads used in the finite element model included a 140 psi seal preload pressure bearing against the front wall, and a 100 psi simulated engine pressure applied to the "wetted" surfaces upstream of the test seal. These represent the maximum engine pressure and seal preload envisioned for the test sequence. The stress fringes shown in Figure 2.7 were calculated using the MARC finite element code. The maximum Von Mises stress found was 1200 psi at the fixed end of the front wall which was caused by bending of the front wall.

The stress found above was compared to the allowable strength as recommended by the ASME Boiler and Pressure Code. In References 2.2 and 2.3, the design stress is the lesser of one-third the tensile strength at operating temperature (Ref. 2.4), or two-thirds the yield strength at operating temperature (Ref. 2.4). The first criterion is the more conservative of the two resulting in an allowable design stress of 20 ksi (e.g., 1/3 of 60 ksi tensile strength) for Inconel X-750 at 1500 °F. This allowable stress is significantly greater than the maximum stress calculated for the test fixture. Hence it was concluded that the rig was properly sized. Comparing the design stress to the Von Mises stress, a factor of safety of 17 is found.

In addition to having high yield and ultimate strengths at temperature, Inconel X-750 has a very high creep rupture strength. At 1500 °F, its 1000 hr creep rupture strength of 20 ksi (Ref. 2.4) ranks with the best of the high temperature metals. By comparison this creep rupture strength is almost four times that of Inconel 600 and five times that of 304 series stainless steel. These features in addition to its excellent oxidation resistance make Inconel X-750 an excellent material for the high temperature fixture.

Thermal Expansion Considerations:

Heater Joint in Rig: In the original design, three in-line air heaters used to heat incoming air were to be screwed directly into the bottom of the test fixture. The standard material for these heaters is 304 series stainless steel that has a higher coefficient of thermal expansion (CTE) than Inconel X-750. At 1500 °F the CTE's of 304 series stainless steel and Inconel X-750 are 11x and $9x10^{-6}$ in./in. °F, respectively (Ref. 2.4). Though this difference is relatively small, a temperature rise of just over 1400 °F causes significant stresses. As shown exaggerated in Figure 2.8 at the location where the stainless steel pipe leaves the rig base, the pipe is unsupported and significant bending stresses develop.

A thermal stress analysis was conducted for the joint between the pipe and the rig. In the analysis the stainless steel pipe and the Inconel rig were allowed to expand at their own rates, resulting in the stresses shown in Figure 2.9. The finite element analysis conducted used axisymmetric elements, hence only the left cross section of the pipe and rig joint are shown. The 22 ksi Von Mises stress found in the corner where the pipe leaves the rig was more than twice the stainless

steel's ultimate tensile strength at 1500 °F. The neighboring 51 ksi stress in the Inconel X-750 rig is only slightly less than the 60 ksi ultimate tensile strength for this material at 1500 °F. Also indicated in the figure are the locations of the largest compressive and tensile axial, hoop and radial stresses.

A solution to allow use of the purchased components was to substitute an Inconel 600 pipe nipple in place of the heaters as is shown in Figure 2.10. A 304 stainless steel pipe coupling was used to connect the stainless steel heater to the pipe nipple. The CTE of the Inconel pipe nipple was the same as the rig so no thermal mismatch exists there. Although there still is a CTE mismatch between the Inconel nipple and the stainless steel coupling, it is not a problem since the coupling is free to grow unimpeded. A special high temperature pipe thread sealant is used (XPAND-SET pipe compound) throughout the system that actually expands slightly when cured to fill any possible openings that may form between the pipe coupling and the pipe nipple.

Large Scale Thermal Growth: Similar to the seal lengths required in the engine, the test fixture was built to test seals 3 ft long. Calculations predicted that the

40-in. Inconel fixture heated to 1500 °F would grow over 0.5 in. This is the growth measured when the rig reaches operating temperature. To accommodate thermal growth of this magnitude special features were incorporated into the rig:

Rig Tie-down: Ignoring thermal growth will normally result in unforgiving hardware failures because the thermal strain energy will be released in one way or another. To allow the rig to grow unimpeded, slotted feet were used on both ends of the rig. Light tension on the bolts used to secure the rig to the table allowed the rig to expand and contract without binding during a temperature cycle.

Piping Manifold: A flexible piping manifold system was implemented in the rig as is shown below the bench in Figure 2.4. The manifold allows the heaters to move axially with the rig growth mentioned above without placing bending loads and unnecessary stresses on the hot heater pipes. Similarly oversize clearance holes are made in the bench top to allow heater movement. The manifold also allows the pipes to grow along their axes.

Axial Preload System: The systems on both sides of the rig used to preload the seals along their axes are also allowed to float with the rig. As shown in Figure 2.4, the right-side preloader including the load cell and pneumatic actuator are bracketed to the base of the rig. Mounting them this way ensures that the axial load measured in the load cell will not be clouded by load developed by the significant thermal loads that would be produced if the system were mounted to the bench.

Threaded Fasteners: Threaded fasteners hold the front wall onto the rig and hold the seal retainer (e.g., the "L"-shaped piece above the seal in Fig. 2.1) in place. After running the rig hot several times, the seal retainer had to be removed for adjustment. Nearly a third of the cap screws holding the retainer in place had seized, requiring them to be drilled out. Close inspection of the surfaces beneath the heads of the A286 cap screws indicated that the heads were seizing against the Inconel seal retainer. This seizing can be caused by several factors including mutual oxidation growth and diffusion bonding between the two mating surfaces.

To overcome similar difficulties in the future, a sequence of tests were conducted with available antiseize compounds and other proven fastener treatment methods to determine an acceptable method of preventing excessive break-away torques after high temperature operation. In these tests, a series of A286 cap screws (3/8-24 UNF) with various treatments specified in Table 2.1 were screwed into an Inconel X-750 disk (representing the seal retainer material). Prior to assembly, the test disk was drilled and tapped and the threads were preoxidized in a furnace for 3 hr at 1500 °F. The resulting color of the test disk was the common greenish-grey Inconel oxidation color. Based on experience at NASA Lewis and within the engine community, pre-oxidizing Inconel components generally reduces the likelihood of seizing threaded components together.

A majority of the cap screws were also preoxidized for 3.5 hr at 1400 °F. The resulting color was a velvety charcoal grey. (Note: Use of the A286 cap screw above 1200 °F is recommended for only short exposures for rated performance. The cap screws are used in the test rig with a de-rated maximum preload.) In many of the tests conducted, an Inconel X-750 washer was placed beneath the head of the cap screw. The Inconel washers were oxidized

in the same manner as the Inconel disk. Washers introduce a second load bearing interface in the load stack that should statistically improve the chances of breaking the connection after heating.

The cap screws were tightened to an assembly torque of 360 in-lb. To simulate a worst-case temperature exposure, the disk and cap-screw test piece was placed in a furnace at 1500 °F for 17 hr. After the disk was allowed to cool to room temperature, the torques required to break the connection were measured using a calibrated dial-type torque wrench. The results of these tests are presented as a bar-chart in Figure 2.11 for easy comparison. The data represent one screw of each treatment, except for treatment number 9 where two screws were used and the average torque is reported.

The break-away torque measured for the cap screw coated with the nickel "antiseize" (specimen 3) was the highest found for all of the tests. Breakaway torques for the nickel antiseize and the copper antiseize (specimens 4 and 5) combined with a washer were lower, but were still 1/3 and 1/4 more than the assembly torque of 360 in-lb.

In some cases, the break-away torques were slightly lower than the assembly torque. As experienced in high temperature bolted-flange connections, this is in part due to relaxation of the asperity contacts of mating threads with temperature.

Preoxidizing the cap screw, coating it with silver antiseize and a light coating of boron nitride and using a preoxidized washer proved to be the most effective approach for assembly and disassembly after heating. This is the thread treatment used for the cap screws and for the studs and nuts for the front wall. (Note: Boron nitride forms boric oxide at elevated temperatures that can weaken some metals over long exposure times. Hence, this thread treatment may not be the best for applications where the high temperature service time is significantly longer than the short run times here.)

Though some breakaway torques for the treatment in which the screw was preoxidized or preoxidized and coated with boron nitride powder had lower disassembly torques, these treatments did not allow easy assembly. In one case, for instance, the cap screws actually seized on assembly presumably because no grease was present. The grease in the silver antiseize facilitates assembly and the

lubricous silver coating and boron nitride powder maintains low break-away torque after the heating cycle.

TEST FIXTURE DEMONSTRATION

The design features incorporated in the test fixture allows a broad range of candidate engine seal concepts to be tested. The test rig is easily configured to test the ceramic wafer seal, the braided ceramic roped seal, or the ceramic ball/ceramic sleeve thermal barrier seal described in Reference 2.1, amongst others. The rig can accommodate each of these seals' dimensions and tolerances as well as axial and lateral preloads.

Seal Specimen: For purposes of demonstrating the high temperature capability of the test rig, the ceramic wafer seal depicted in Figure 2.12 was installed and tested. The ceramic wafer seal consists of a stack of ceramic wafers mounted in the seal channel and preloaded against the adjacent wall using the lateral bellows preload system described. The ceramic wafers used in these tests are made of high density aluminum oxide (Al_2O_3) ceramic. The wafers are 0.500 ± 0.001 in. square and are 0.125 ± 0.001 in. thick. The wafer faces are smooth (<20 μin. RMS) and parallel to within 0.001 in. so that

leakage between adjacent wafers would be minimized. The wafer corners are rounded with a 0.09 in. corner radius to prevent the wafers from digging into the engine panel and to minimize wafer corner stresses. At both ends of the seal stack (e.g., where the seal is "built-in" to the test fixture), wafers having square corners were used to prevent extraneous seal end-leakage.

Test Results: Leakage rates for the ceramic wafer seal sealing 1350 °F air are shown versus pressure drop in Figure 2.13. In this test the seal sealed against a simulated engine wall distortion in which the adjacent wall bulged in toward the seal. The gap was 0.05 in. in the center varying sinusoidally to 0.20 in. at both ends. The peak-to-peak wall distortion was 0.15 in. in only an 18 in. span.

Prior to heating, the wafers were first preset to the preferred sealing position (e.g., in contact with the front wall and in contact with the top of the seal channel) using the lateral preload (≈50 psi seal contact pressure) and the engine pressure. The wafers were axially compressed with 10 lb (or 40 psi contact pressure for the 0.5 in. square seal) using both left and right axial preloaders.

As shown in Figure 2.13 the seal performed well. The seal's leakage rate was below the tentative leakage limit of 0.004 lb/s-ft (shown as horizontal dashed line) for the full pressure range tested. (Note: The tentative leakage limit cited is a goal leakage limit arrived at by the hypersonic engine community for seal concept screening purposes, Ref. 2.1.) Furthermore, the seal leakage for these test conditions was repeatable. Shown in the figure are two complete increasing-decreasing pressure cycles that lie on the smooth curve.

SUMMARY AND CONCLUSIONS

A high temperature test fixture for evaluating the performance of advanced hypersonic engine seals has been installed and successfully checked-out at NASA Lewis Research Center. The rig tests candidate seals 3 ft long as typically required for hypersonic engine panels. The test fixture can subject seals to temperatures up to 1500 °F and pressures differentials up to 100 psi. Furthermore, seal performance in sealing either straight or engine simulated distorted sidewalls can be measured. Sidewall distortions as large as 0.15 in. in only 18 in. of span can be tested in the rig. The sensitivity of leakage performance to lateral or axial loading can also be measured using specially designed high temperature bellows preload systems.

Designing the test fixture for high temperature operation required attention to be paid to several important design criteria not often required for conventional design. Materials selected for the rig have high tensile and creep strengths at temperature. The primary material used for the rig was Inconel X-750. Another issue confronted was avoidance of potentially high thermal stresses that can occur using materials with different

coefficients of thermal expansion (CTE). An example of the potentially dangerous stresses that can result was demonstrated herein for a contemplated heater-to-rig joint. Finite element analyses performed at a critical joint between the relatively high CTE stainless steel air heater pipe and the relatively low CTE Inconel rig uncovered high thermal stresses which led to an improved joint approach.

The 0.5 in. axial expansion of the 3 ft long rig at 1500 °F influenced several design features of the test fixture. The rig and the axial preload systems were allowed to float. And, the piping manifold system was designed to be flexible to allow the heaters to accommodate rig growth. In both of these cases freedom of movement prevents development of excessive thermal stresses.

The high temperature threaded fasteners used in the test fixture need some form of treatment to prevent seizure and excessively high breakaway torques. Furnace tests at 1500 °F with multiple available thread treatments demonstrated that the best treatment was preoxidizing all of the components including the washer, and coating the threads with silver antiseize and a light coating of

boron nitride powder. This method has been successful in preventing fastener seizure in subsequent high temperature runs.

The test fixture's performance was demonstrated using a unique flexible high temperature ceramic wafer seal. The seal's leakage performance was measured at 1350 °F, at pressure differentials ranging from 10 to 100 psi sealing against an engine simulated distorted wall condition. The seal performed well with a leakage rate significantly below the tentative leakage criterion, for the heating and loading sequence used.

On the basis of these findings, the following results were obtained:

1. A unique high temperature seal test fixture meeting all of the specified design criteria has been successfully demonstrated.

2. Stresses within the seal test fixture are less than 1/10th the allowable design stresses recommended by the ASME boiler code.

3. Thermal stresses predicted for a contemplated stainless steel air-heater/Inconel X-750 rig joint exceeded the stainless steel tensile strength at 1500 °F. The implemented approach of using a stainless steel pipe coupling to join the heater to an Inconel 600 pipe nipple extending from the test rig overcomes the excessive stress problem.

REFERENCES FOR CHAPTER 2

2.1 Steinetz, B.M., DellaCorte, C., and Sirocky, P.J., "On The Development of Hypersonic Engine Seals," NASA TP-2854 (1988).

2.2 Boiler and Pressure Vessel Code, Section VIII, Division 1. American Society of Mechanical Engineers (1980).

2.3 Boiler and Pressure Vessel Code, Section VIII, Division 2. American Society of Mechanical Engineers (1980).

2.4 Kattus, J.R., "Inconel X-750," Aerospace Structural Metals Handbook, Metals and Ceramics Information Center, Battelle Labs, Columbus, OH, Vol. 4, Article 4105 (1990).

Table 2.1 Detailed listing of the A286 fastener treatments prior to assembly and high temperature exposure.

Treatment No.	Thread treatment	Washer
1	As received cap screw. No oxidation. Control sample	No
2	Preoxidized cap screw.	No
3	Preoxidized cap screw. Nickel antiseize[1]	No
4	Preoxidized cap screw. Nickel antiseize[1]	Yes
5	Preoxidized cap screw. Copper antiseize[2]	Yes
6	Preoxidized cap screw. Boron Nitride powder[3]	Yes
7	Preoxidized cap screw. Nickel antiseize[1] and Boron Nitride[3] powder.	Yes
8	Preoxidized cap screw. Silver antiseize[4].	Yes
9	Preoxidized cap screw. Silver antiseize[4] and Boron Nitride[3] powder.	Yes
10	Nonoxidized cap screw with 1 μm layer sputtered silver solid lubricant.	Yes
11	Nonoxidized cap screw with 1 μm layer sputtered silver solid lubricant. Silver antiseize[4]	Yes

Assembly compounds:

[1]Nickel antiseize, nickel and aluminum powder mixed with grease. Rated temperature: 2400 °F. Available as Never-Seize from Bostik Co., Cat. No. NSBT8-N, Middleton, MA.

[2]Copper antiseize, copper powder mixed with grease. Rated temperature: 1800 °F. Available as Felpro C5A antiseize lubricant from Fel-Pro, Part No. 51007, Skokie IL.

[3]Boron Nitride powder. Rated temperature: >2000 °F. Available from Standard Oil Engineered Materials, Part No. SHP-325, Niagara Falls, NY.

[4]Silver antiseize. Silver powder mixed with grease. Rated temperature: 1500 °F. Available as Silver Goop from Crawford Fitting Co. Solon, OH.

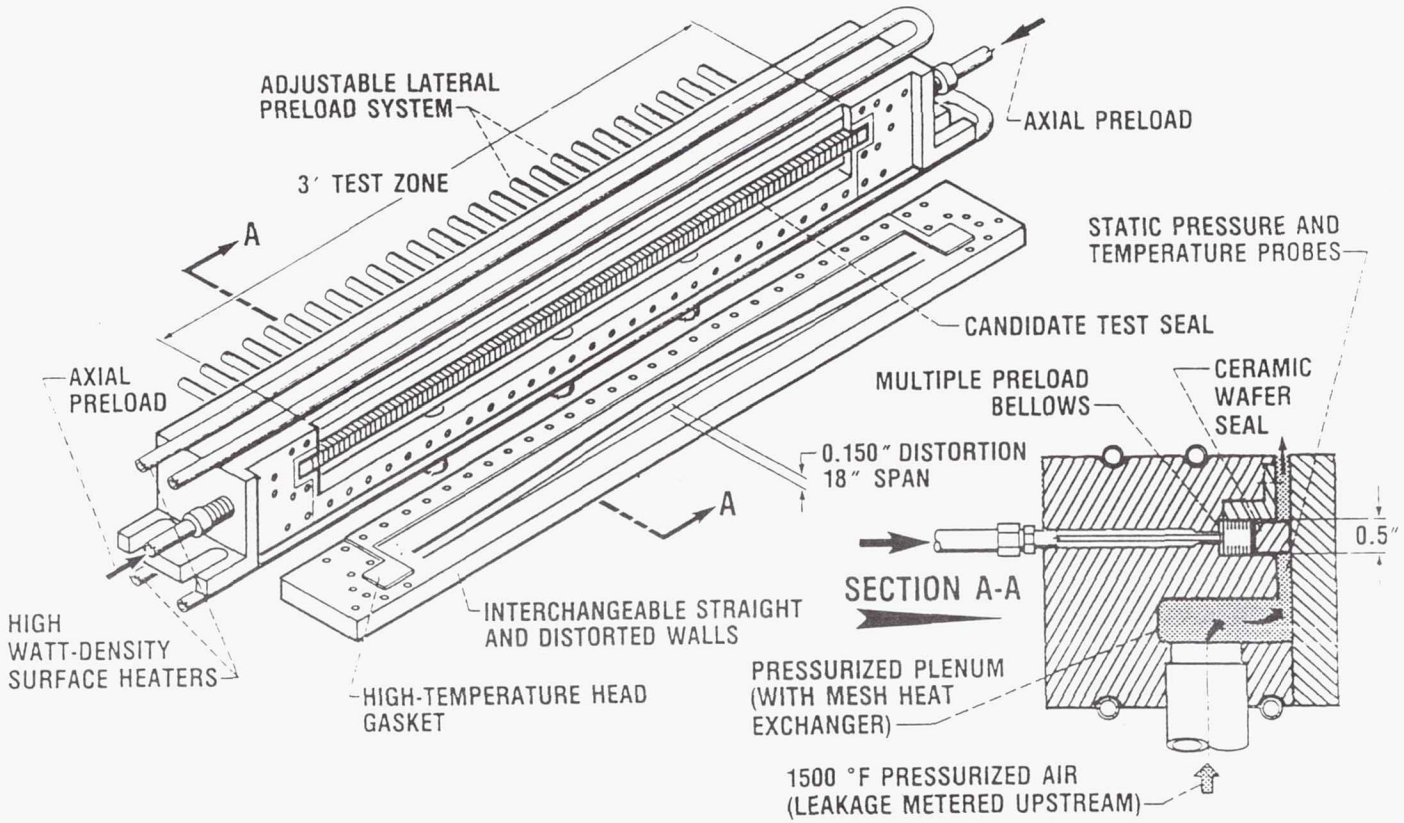

Figure 2.1.—Schematic of high temperature panel-edge seal test fixture.

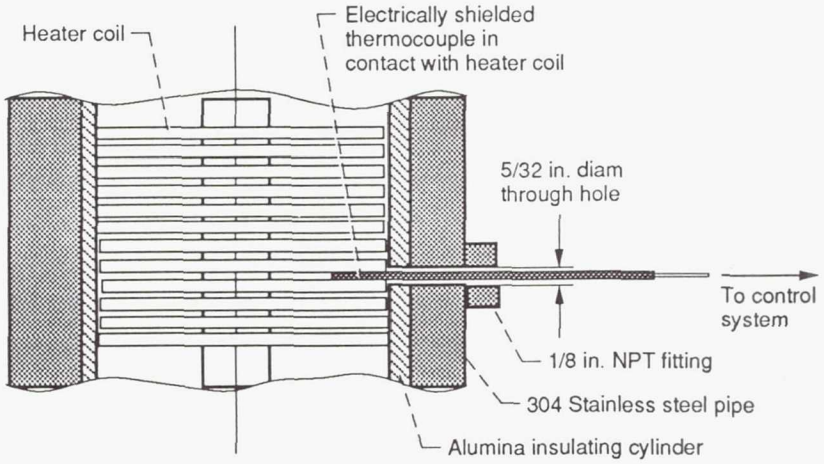

Figure 2.2—Air heater over-temperature sensing technique, enlarged for clarity.

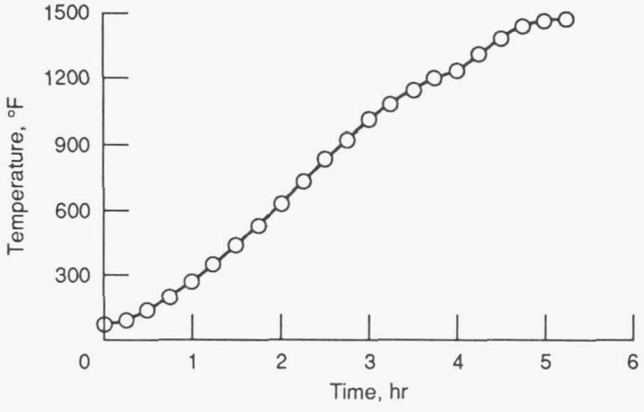

Figure 2.3.—Temperature-time rig heating profile using both surface-mount and in-line air heaters.

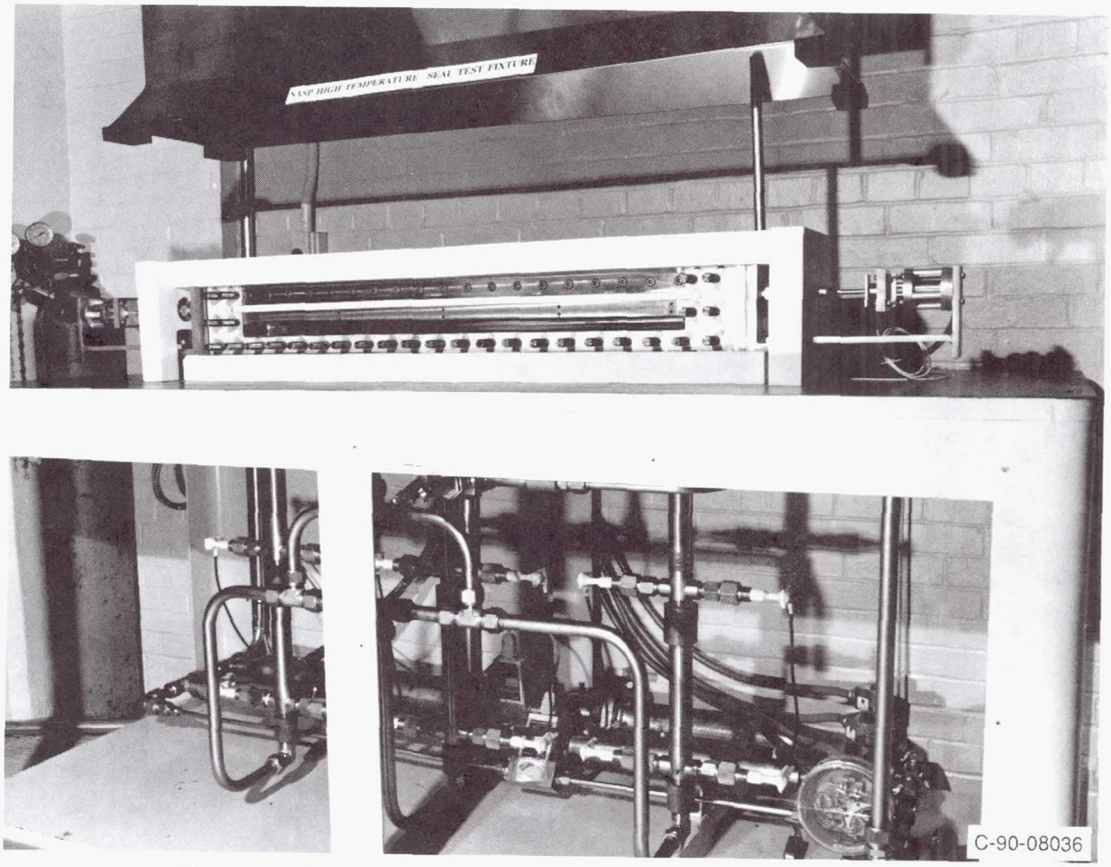

Figure 2.4.—Photo of high temperature seal test rig, front wall removed for clarity.

C-90-08039

Figure 2.5.—Photo of Inconel welded-leaf lateral-preload bellows.

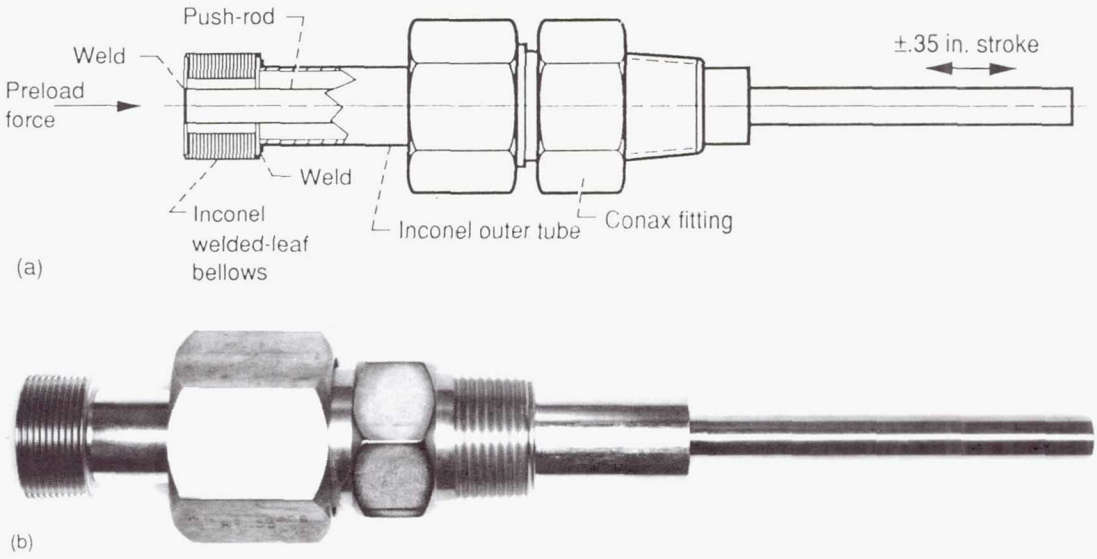

Figure 2.6.—Schematic (a) and photo (b) of high-temperature, hermetically sealed axial preloader.

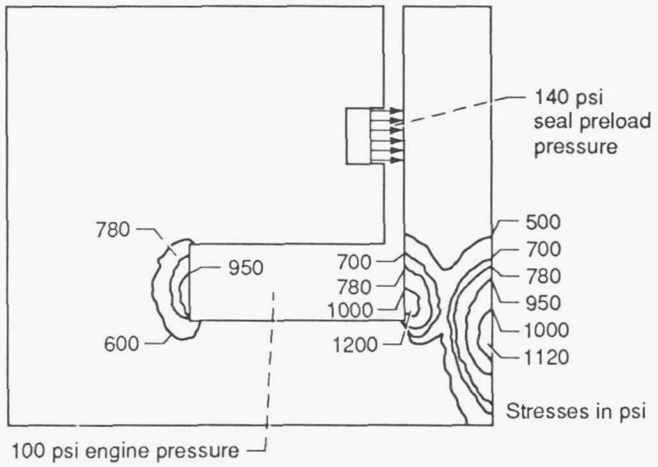

Figure 2.7.—Seal fixture Von Mises equivalent stress contours under maximum loading conditions.

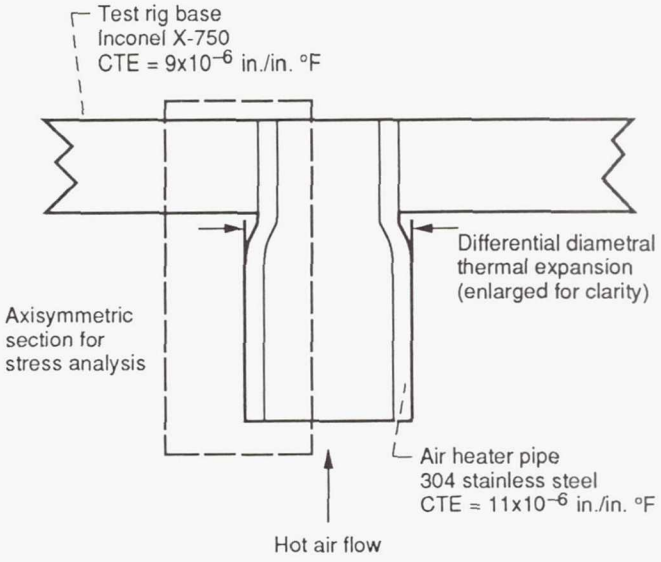

Figure 2.8.—Schematic of joint between heater-pipe and rig-base showing potential effects of mismatch in thermal expansion coefficients at temperature.

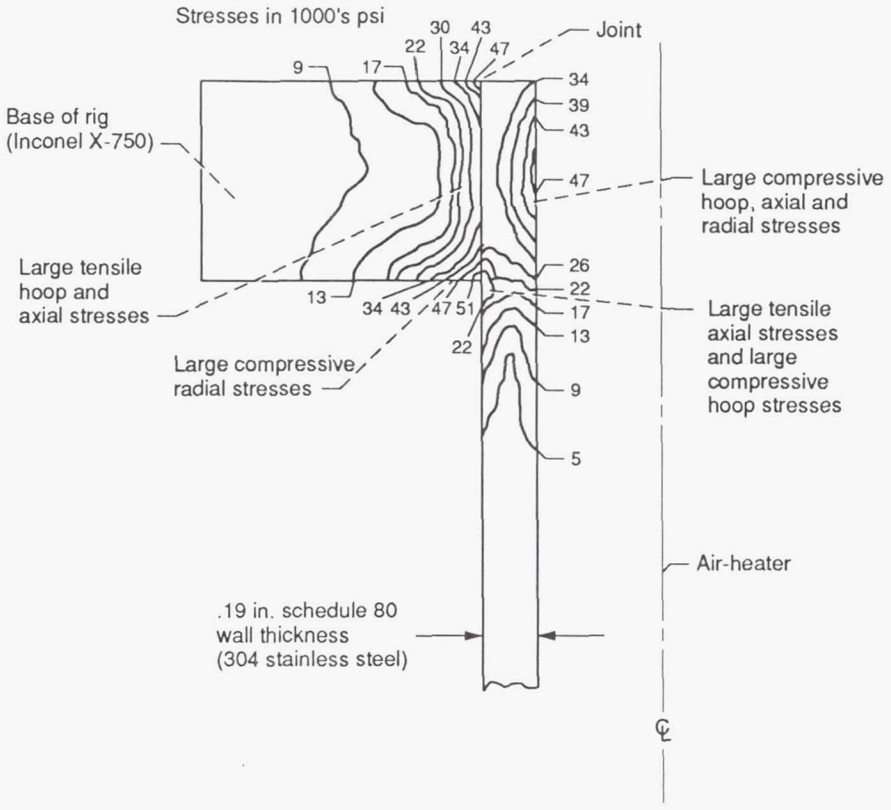

Figure 2.9.—Heater-pipe and rig-base Von Mises equivalent stress contours caused by mismatch in heater and rig thermal expansion coefficients at 1500 °F.

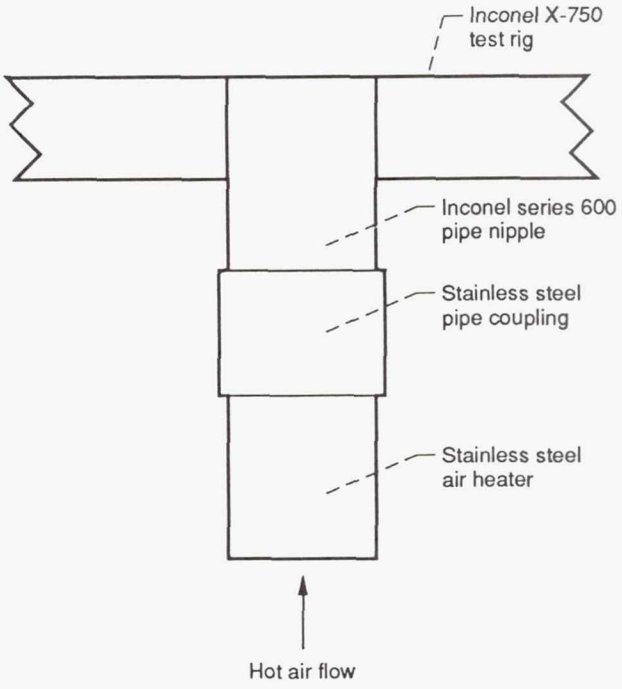

Figure 2.10.—Implemented heater attachment approach to avoid thermal stress problem caused by mismatch in thermal expansion coefficients.

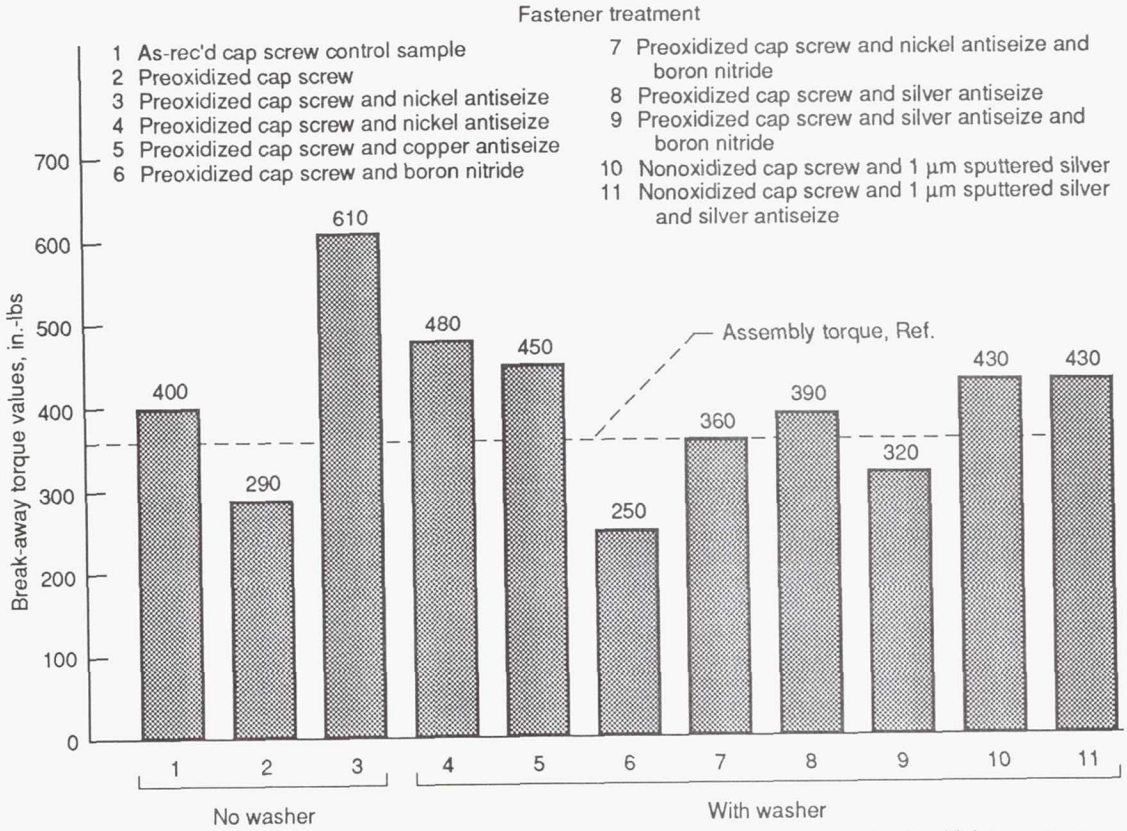

Figure 2.11.—Cap screw break-away torque values for various fastener treatments after high temperature exposure.

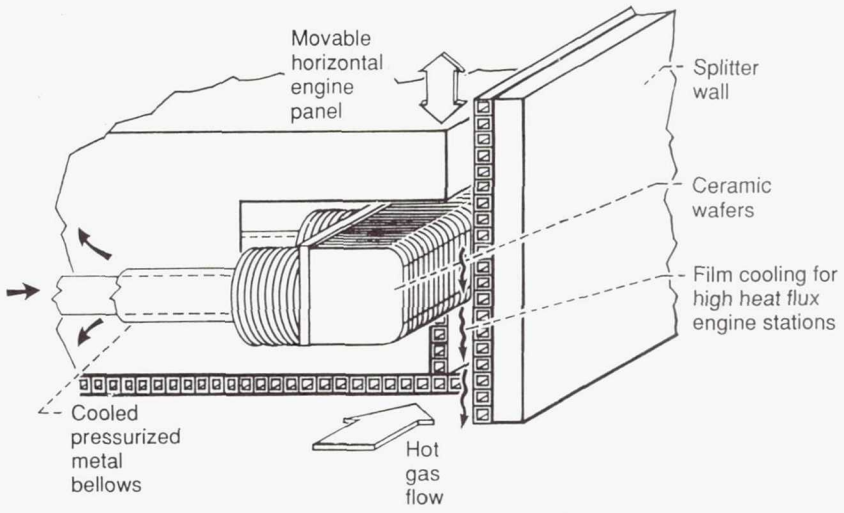

Figure 2.12.—Isometric of ceramic wafer seal.

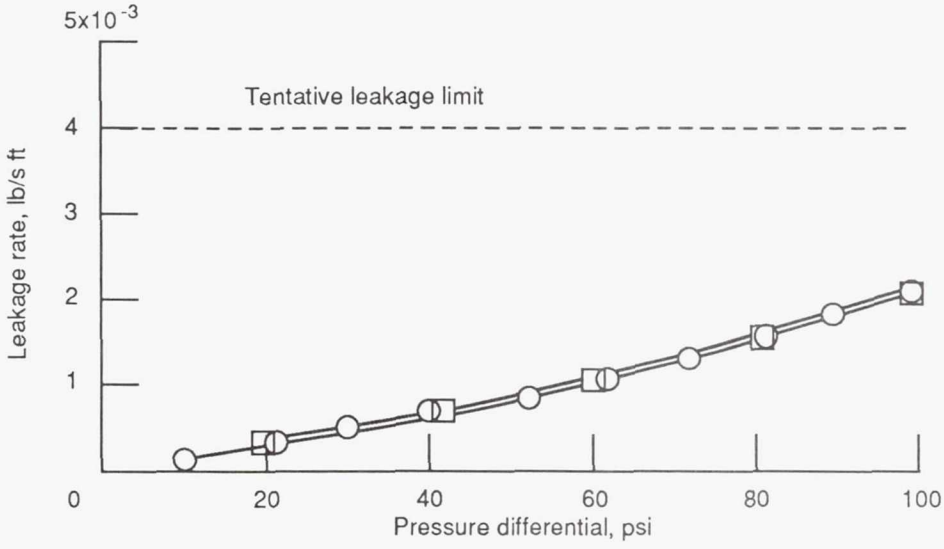

Figure 2.13.—Ceramic wafer seal leakage rate versus pressure drop for 1350 °F air, sealing against engine simulated distorted wall condition.

CHAPTER 3

3. HIGH TEMPERATURE PERFORMANCE EVALUATION OF THE HYPERSONIC ENGINE CERAMIC WAFER SEAL

INTRODUCTION

Prior to costly engine testing, the performance of the ceramic wafer seal described in previous chapters (also see Refs. 3.1 to 3.4) must be assessed under test conditions where the key variables (e.g., pressure, temperature, wall condition, etc.) can be controlled and monitored. The ceramic wafer seal was selected as the leading candidate amongst four seal concepts examined in Reference 3.1, because of the seal's low room temperature leakage rates.

Employing the unique high temperature test capability described in detail in the previous chapter, the objectives of the investigation described herein are to: 1. demonstrate the performance of the wafer seal and required preload techniques at engine simulated temperatures and pressures; 2. assess materials issues such as differences in coefficients of thermal expansion on leakage rates; 3. assess seal leakage rates as a function of pressure, temperature and adjacent wall condition; and to 4. develop a database of seal leakage rates to validate seal leakage modeling.

Seal leakage models are useful tools for seal designers for several reasons. Using validated seal leakage models, designers are able to estimate the percent of engine core flow leaked past the engine panels as a function of the mission profile, seal length and engine pressures and temperatures. Engine designers can use closed-form seal leakage equations in global engine performance computer codes to predict the effect of seal leakage on engine performance. Leakage models serve a second perhaps more important purpose of estimating the coolant flow rates for engine stations such as the combustor where some form of positive purge is required to cool the seal and inert backside engine cavities.

APPARATUS AND PROCEDURES

Test Set-Up: High temperature leakage measurements were made for the ceramic wafer seal using a specially developed panel-edge seal test fixture described earlier in this work (also Ref. 3.2). For reference purposes, a brief overview of the test fixture and test procedures are repeated herein. Three foot seal specimens were mounted in the Inconel test fixture shown in schematic in Figure 3.1. The seal and rig were heated using a series of electric-resistance surface conduction and air heaters

that could heat the rig to 1500 °F. Metered pressurized air is supplied to the base of the seal through the in-line air-heaters.

The wafer seal is mounted in a close tolerance seal channel. The channel tolerance was set at 0.004 in. larger than the wafer seal height using the adjustable "L"-shaped seal retainer shown in cross section in Figure 3.1. The seal is preloaded against the adjacent wall representing the engine splitter wall using a series of pressurized Inconel metal bellows. Seal contact pressures up to 50 psi were examined.

On both ends of the seal, specially developed hermetically sealed axial preloaders were used to apply uniform axial loads to the seal minimizing inter-wafer leakage. The special bellows design allowed uniform preload to be applied to the seal ends without introducing end leakage paths, even though significant differential (up to 0.2 in. over the 3 ft long seal) thermal growths were observed.

Seal Specimen: The ceramic wafer seal tested herein is shown in the movable engine panel in Figure 3.2. The ceramic wafer seal consisted of a stack of ceramic wafers

mounted in the seal channel and preloaded against the adjacent wall using the lateral metal bellows preload system described. The ceramic wafers used in these tests are made of high density aluminum oxide (Al_2O_3) ceramic. The wafers are 0.500±0.001 in. square and are 0.125±0.001 in. thick. The wafer faces are smooth (<20 μin. RMS) and parallel to within 0.001 in. so that leakage between adjacent wafers would be minimized. The wafer corners are rounded with a 0.06 to 0.09 in. corner radii to prevent the wafers from digging into the engine panel and to minimize wafer corner stresses. At both ends of the seal stack (e.g., where the seal is "built-in" to the test fixture), wafers having square corners were used to prevent extraneous seal end-leakage.

Adjacent Wall Condition: A simple method of prescribing various engine wall conditions was used during these tests. A front wall or cover plate is made with two precision machined surfaces. One side is finished flat overall. Bolting this side toward the seal results in an inter-panel gap width of 0.20 in. over the full 3 ft length, (accounting for the thin ≈0.016 in. high-temperature head gasket). The opposite side has a sinusoidal wave machined onto it. The wave bulges inward toward the seal with a peak of 0.15 in. at the center

(see Fig. 3.1). When bolted against the seal, the inter-panel gap width is 0.05 in. at the center sinusoidally increasing to the full 0.20 in. at both ends. The flow area for the straight gap condition is 7.2 in.^{2}. The flow area for the wavy wall condition is 4.5 in.^{2}.

Procedure: Leakage rates were measured for the seal for each wall condition at four temperatures from room temperature to 1350 °F. For each wall condition and each temperature, the engine simulated pressure was varied typically from 100 psi down to 10 psi and then back up to 100 psi for at least one complete pressure cycle. In several cases the seal leakage rates were measured for multiple pressure cycles to establish seal leakage repeatability.

Prior to heating to temperature, the wafers were first preset to the preferred sealing position (e.g., in contact with the front wall and in contact with the top of the seal channel) using the engine pressure and the lateral preload (≈50 psi seal contact pressure). The wafers were axially compressed with 10 lb (or 40 psi contact pressure for the 0.5 in. square seal) using both left and right axial preloaders.

Instrumentation: As discussed in detail in Reference 3.2, leakage measurements were made using a heated capillary tube calibrated flow meter with accuracy better than 1 percent. Pressure measurements were made upstream of the seal using a series of capacitance pressure transducers with better than 0.5 percent accuracy. Gage pressure measurements were made since the seal leakage was exhausted to ambient conditions. Air temperature measurements were made using micro-gage open-bead thermocouples inserted in the flow just upstream of the seal. Lateral preload was measured by measuring pressure in the manifold supplying pressure to the lateral bellows. Axial preloads were measured using calibrated load cells mounted in series with the axial preload system.

RESULTS AND DISCUSSION

EXPERIMENTAL RESULTS

Pressure and Temperature Effects: The ceramic wafer leakage rates were measured over the anticipated engine pressure loads at several engine simulated temperatures. Leakage rates for the seal sealing against the flat wall conditions are shown in Figure 3.3 at air temperatures of 73, 200, 940, and 1350 °F. The low to moderate temperatures correspond to engine inlet temperatures under high speed flight conditions. The high temperature gas corresponds to engine gas temperatures 1 to 2 ft forward of the engine combustion chamber at a Mach 8 flight condition.

The seal leakage rates for each of the temperatures examined were below the industry-established tentative leakage limit of 0.004 lb/s-ft (see Ref. 3.1) shown as the dashed horizontal line for reference purposes in each of the figures. Leakage rates generally decreased with increasing temperature up to moderate temperatures at which point the trend reversed and a slight increase in leakage rates was observed. A potential explanation for

this leakage temperature-dependence is given below where the measured and predicted leakage rates are compared.

Adjacent Wall Effects: The leakage rates for the seal sealing against an engine simulated distorted wall condition are shown in Figure 3.4 as a function of engine pressure and at engine simulated temperatures of 76, 530, 1000, and 1350 °F. Similar to the trends found when sealing against the flat wall, the leakage rates decrease with increasing temperature up to 1000 °F. Then for intermediate to high temperatures the seal leakage rates increase with increasing temperature.

Comparing the leakage rates for the two wall conditions examined, the leakage rates for the seal sealing against the flat wall are slightly more than those measured sealing against the distorted wall condition, as is shown in Figure 3.5 for an applied pressure differential of 100 psi. The reason for this observed trend can be understood from the total effective area the seal is sealing in both wall conditions. Because the distorted wall pushes in against the seal the total effective area to be sealed is only 4.5 $in.^2$ versus 7.2 $in.^2$ for the uniform or flat wall condition.

The seal performed well through the sequence of tests described. The ceramic wafer seal met the tentative leakage limit for all combinations of applied engine pressure differentials, temperatures, and simulated wall conditions. It is emphasized to achieve these performance results certain important conditions must be met.

Precision machined wafers must be used to ensure intimate contact with their neighbors and with adjacent sealing surfaces. The need for precision machined surfaces was demonstrated by a test at room temperature in which one wafer with poor wafer-face parallelism was accidentally installed. Leakage rates for this seal build were up to 20 percent higher than those shown herein. It is also emphasized that the seal achieves the performance results shown when in its preferred sealing position against the top channel surface and against the adjacent wall.

THEORETICAL RESULTS

A closed form seal leakage flow model has been developed to predict seal leakage response over the wide range of engine pressures and temperatures. The leakage model is based on externally pressurized gas film bearing theory

modified to account for the special features of the seal. Details of the model development are given in the Appendix Section of this chapter. The important results obtained in the Appendix are summarized next.

Leakage Pressure-Dependence: The compressible nature of the gas for the high 7.8:1 pressure ratios found in the seal results in a leakage flow rate expression dependent on the difference in the squares of the supply and exhaust pressure, (e.g., a parabolic pressure dependence). The measured leakage rates though slightly parabolic in nature are less so than predicted by the unmodified constant film-height gas-film bearing theory.

As demonstrated in the Appendix, the constant film-height leakage flow equation over-predicts the measured seal leakage by a considerable margin (≈53 percent), at the highest pressure differential of 100 psi. The cause of this discrepancy lies in the constant film-height assumption. As the applied engine pressure increases considerable forces develop to reduce the film-heights between the seal wafers and the adjacent sealing surfaces. Modifying the flow equations to allow for variable film-height as a function of applied pressure differential allows a close prediction within 6 percent

of the measured leakage rates even for the highest pressure differential of 100 psi.

The seal leakage rate per unit length developed in the Appendix is shown in Equation (1):

$$\dot{m}/L = \frac{(P_s^2 - P_o^2)}{24\mu RT}\left(\frac{h^3_{1,v}}{H_1} + \frac{h^3_{2,v}}{H_2} + \frac{Ngh^3_{CTE}}{LH_2}\right) \qquad (1)$$

There are three potential seal leakage paths: 1. between the wafer and the top surface of the seal channel accounted for by the $h_{1,v}$ term; 2. between the seal nose and the adjacent wall accounted for by the $h_{2,v}$ term (e.g., where the v denotes variable film height); and 3. at high temperatures between the inter-wafer gaps caused by differential seal and engine panel thermal expansion, accounted for by the h_{CTE} term. The other variables in the model describe the seal's length, L; height H_2; contact dimension with the top channel H_1; inter-panel gap width, g; and number of wafer interfaces N, as described in the Appendix. The leading coefficient includes terms for the gas properties, gas temperature, and pressure differential applied across the seal.

Leakage Temperature-Dependence: The leakage flow equation has been used to predict the leakage as a function of temperature and pressure. The results of these calculations are shown in Figures 3.6, 3.7 and 3.8 along with the measured results. In each of these curves the measured results are shown with a solid line and the predictions made using the equation are shown with the dashed line. As is well known, gas viscosity increases with temperature. Throughout these analyses the power law of gas viscosity: $\mu = \mu_o(T/T_o)^{2/3}$ (Ref. 3.5) was used for the air viscosity in Equation (1).

In Figure 3.6, the measured and predicted leakage rates are compared for a fixed engine pressure differential of 20 psi. The correlation between the predicted and measured leakage rates is very good for the full temperature range. In Figure 3.7 the measured and predicted leakage rates are compared for a fixed engine pressure differential of 40 psi. The correlation between the predicted and measured leakage rates is reasonable for this pressure differential. The maximum discrepancy between the measured and predicted was slightly over 20 percent and occurred at intermediate temperatures of about 500 °F. This discrepancy narrowed to about 14 percent at gas temperatures of 1350 °F.

Comparisons are made between the measured and predicted leakage rates at the maximum expected pressure differential of 100 psi in Figure 3.8. Examining Figure 3.8, it is noted that the both the measured trends of decreasing leakage followed by slightly increasing leakage rates are both modeled by Equation (1). For this pressure case the maximum discrepancy between the predicted and measured is about 38 percent at 500 °F. However, at 1350 °F the discrepancy between measured and predicted was only 18 percent.

Discrepancies as noted above can be caused by several sources. The most probable cause is thermally-induced non-uniform changes in the size and shape of the film-heights (h_i). Since the flow responds to changes in gap height cubed one can see why thermally induced changes in contact condition can lead to a appreciable changes in leakage. As an example, analytically changing gap height by 11 percent results in a 38 percent change in leakage. This observation underscores the need to maintain small gaps through optimal loading, wafer design, and tolerances.

It is noted that even though some modeling discrepancies are observed, the absolute magnitude of the leakage rates

are still below the industry-established tentative leakage limit, shown by the horizontal dashed line in the figures.

Gas Property Dependence: Throughout the engine the seal will be required to seal a variety of gases and gas mixtures. Furthermore it is contemplated to use the seal in two different sealing approaches in the engine. In areas such as the engine inlet where the ambient flow temperatures are below the seal operating temperature and where hydrogen is not present, the seal can be used in the traditional manner of minimizing parasitic core flow losses past the movable engine panels.

In the engine combustion area, the seal designer's paramount concern is to prevent the leakage of the extremely hot flow path gases containing unburned mixtures of hydrogen-oxygen from leaking behind the movable engine panels. Leakage of these potentially explosive gases could cause destruction to or loss of the engine. In these critical areas it is contemplated to use a dual ceramic wafer seal approach (described in Chapter 1) with the cavity between the dual seals pressurized with an inert gas purge nominally 10 to 15 psi above the ambient engine core pressures. In this

approach the seal functions to limit the purge gas (see Fig. 3.2) flow into the engine combustion chamber minimizing loss coolant which is at a premium. The two key advantages of this approach is that the purge gas inerts the backside engine cavity precluding leakage of hydrogen gases and the purge gas cools the seal. The study conducted in Reference 3.4 demonstrated that using a minimal purge flow of 70 °F helium the seal (made of silicon carbide) could be kept below it operating temperature for a near maximum engine heating rate of 1160 Btu/sq-ft-sec.

A variety of gases including helium and nitrogen have been considered to serve the dual role of inerting the backside cavities and cooling the seal. Helium is a prime candidate because of its low density and good cooling effectiveness (e.g., heat capacity). Equation (1) can be used to estimate the relative flow rates of various gases for similar pressure, temperature and gap conditions. The gas properties are modelled in Equation (1) by the viscosity, μ, and gas constant, R. An expression for the relative flow rates of two gases (e.g., A and B) can be found by taking the ratio of these gas properties and using the relation that the gas

constant R is simply the universal gas constant R^* divided by the gas's molecular weight, MW:

$$\frac{(\dot{m}/L)_A}{(\dot{m}/L)_B} = \frac{MW_A}{MW_B}\,\frac{\mu_B}{\mu_A} \qquad (2)$$

The above expression can be used to estimate the relative leakage rate of helium, for instance, relative to the air leakage rates measured herein. Substituting values for both gas's molecular weights and viscosities at room temperature (Ref. 3.5) we note that for other things held constant the helium leakage rate would be 0.126 (or approximately 1/8th) that of the air leakage rates measured herein:

$$\frac{(\dot{m}/L)_{He}}{(\dot{m}/L)_{Air}} = \frac{4}{29}\,\frac{1.22x10^{-5}}{1.34x10^{-5}} = 0.126 \qquad (3)$$

Wafer Size Effects: The half-inch wafer selected for this study was suitable for the space available along the edge of the panels being considered for the engine. It

is observed from Equation (1) that increasing the contact dimensions H_1 and H_2 between the seal and adjacent surfaces can have a beneficial effect on seal leakage. Increasing the wafer size and making either a large square wafer or a rectangular wafer would according to Equation (1) linearly decrease the seal leakage rates.

Using rectangular instead of square wafers offers the added benefit of improving the wafers "piloting" ability within the seal channel by increasing the seal wafers length-to-height ratio. Both of these benefits however must be optimized within seal weight and space limitations established by the overall engine design.

SUMMARY AND CONCLUSIONS

Leakage rates of a high temperature flexible ceramic wafer seal have been assessed using a specially designed static high temperature panel-edge seal fixture. The seal is designed to seal the many feet of linear gaps between movable structural panels and adjacent splitter walls of advanced hypersonic ramjet/scramjet engines. The seal is made of precision machined wafers mounted in a closely conforming seal channel machined in the movable engine panel. The seal derives its flexibility to accommodate the large distortions in the counterface adjacent engine panels through relative sliding of adjacent wafers. The seal is preloaded from behind using a series of high temperature Inconel bellows that maintain the seal in contact with the adjacent wall.

Typical of the engine, 3 ft lengths of the seal were tested under simulated pressure differentials, temperatures and wall conditions. The seal was tested at pressures ranging from 10 to 100 psi and at temperatures from room temperature to 1350 °F. The seal's ability to accommodate simulated engine wall and gap conditions was measured using two wall configurations. For the flat wall condition the seal sealed a uniform 0.20 in. inter-

panel gap (e.g., the space between the horizontal and vertical engine panels). For the distorted wall condition the seal sealed an engine simulated gap in which the inter-panel gap varied sinusoidally from 0.05 in. at the center increasing to the full 0.20 in. at both left and right ends.

A seal leakage flow model was developed based on Reynolds equation and externally pressurized gas film bearing theory. The leakage model allows designers to estimate seal leakage response under various gas, pressure, and temperature conditions. The model can also be used to estimate the effects of seal size on seal leakage rates.

Seal leakage is very sensitive to variations in film height between the seal and mating seal surfaces varying with film height cubed. Discrepancies were noted between the predicted and measured leakage rates as a function of pressure drop when assuming a constant film-height between the seal and the adjacent sealing surfaces. Introducing a variable (e.g., decreasing) film height with increasing pressure differential corrected the noted discrepancies.

The seal model accounts for the three potential leakage flow paths. Two of the paths are between the seal nose and adjacent engine panel and between the seal and the downstream (e.g., top) surface of the seal channel. The third path observed at temperature is between the wafers through small gaps that open between wafers caused by a mismatch in thermal expansion coefficients between the ceramic wafer seal and the metal simulated engine-panel.

A force balance performed on the ceramic wafer seal demonstrated that the engine pressure exerts self-seating forces on the seal urging the seal toward the desired seal location. The force urging the seal against the adjacent engine sidewall is caused by the difference in the engine pressure exerted on the back of the seal and the parabolically decreasing pressure profile existing on the seal nose. The force urging the seal against the downstream surface of the seal channel is caused by the differences in the engine pressure exerted on the upstream side of the seal and the composite: ambient pressure and the parabolically decreasing pressure between the seal and the seal channel.

On the basis of these findings, the following results were obtained:

1. The ceramic wafer seal leakage rates were below the 0.004 lb/s-ft industry established tentative leakage limit for air pressure differentials up to 100 psi and temperatures up to 1350 °F. The seal leakage rates were below the leakage limit for both the flat wall condition (sealing a uniform 0.20 in. inter-panel gap) and for the engine simulated distorted wall condition (sealing a significant peak-to-peak wall distortion of 0.15 in. in only an 18 in. span).

2. Seal leakage mass flow rates decrease with increasing temperature for low to intermediate temperature (e.g., 1000 °F) as increasing gas viscosity limits flow through the small seal gaps. For temperatures above 1000 °F a small increase in the seal leakage mass flow rate is observed and is attributed to small inter-wafer gaps opening due to a mismatch in thermal expansion between the ceramic wafers and the metal simulated engine-panel.

3. Based on the seal leakage model developed, the leakage mass flow rates for gases other than

the air tested can be estimated from the air data collected herein. The leakage mass flow rate of the second gas can be scaled from the air data by multiplying the measured air flow by the ratio of the second gas's molecular weight to that of air and by the ratio of the viscosity of air to the viscosity of the second gas.

APPENDIX - LEAKAGE MODEL FOR CERAMIC WAFER SEAL

Nomenclature:

$\dot{m}/L$	=	seal mass flow per unit length
P	=	pressure, abs.
T	=	temperature, abs.
g	=	inter-panel gap width
H_1 , H_2	=	seal-to-wall contact dimensions
h_1 , h_2	=	seal film heights
R	=	gas constant
n	=	polytropic exponent
c_p , c_v	=	heat capacities
U	=	seal velocity (≈ 0)
u	=	leakage gas velocity profile
t	=	time
A , B	=	constants
L	=	seal length
s , w	=	lengths as defined in Figure 3.9
N	=	number of wafer interfaces
F	=	force
M	=	moment
x , y	=	coordinate directions

Greek:

α	=	coefficient of thermal expansion
ρ	=	gas density
μ	=	gas viscosity
μ_o	=	gas viscosity at room temperature

Subscripts:

1 , 2	=	seal top and seal nose surfaces
s	=	supply
o	=	exhaust
eff	=	effective
CTE	=	coefficient of thermal expansion
v	=	variable film height

Model Development

An analytical expression is developed herein to estimate the leakage rates of the ceramic wafer seal. The model is developed based on externally pressurized linear gas-film bearing theory. Similarities between the flow past the seal and through gas-film bearings include similar pressure ratios (8:1), geometry, and low Reynolds number flow, as will be demonstrated herein. Using Reynolds equation as a starting point, the leakage flow model is developed with some modifications required to account for

some subtleties of the seal. The necessary flow variables and geometry terms used throughout this derivation are shown graphically in Figure 3.9.

During room temperature tests two leakage paths were identified for the wafer seal, between the nose of the seal and the adjacent engine splitter wall (denoted by h_2) and between the top of the wafers and the adjacent top surface of the seal channel (denoted by h_1). The method used to identify these leakage paths was carefully placing small amounts of soap solution at each of these interfaces and examining the origins of the bubbles. Referring to Figure 3.9 these leakage paths are shown enlarged for clarity. As will be demonstrated below these leakage were small and were less than 0.001 in. in size.

Pressure measurements indicated that the pressure in the cavity behind the seal wafers is equal to the supply pressure P_s, since the wafers are actually lifted out of contact with the lower surface of the seal channel. Thus the driving potential for both of the leakage paths mentioned is the engine supply pressure, P_s. Therefore the seal leakage mass flow rate is simply the sum of these two parallel leakage paths:

$$\dot{m}/L = \dot{m}_1/L + \dot{m}_2/L \qquad \text{(A1)}$$

Expressions for each of these components of the mass flow rate are derived from the basic Reynolds flow equation (Ref. 3.6) where the flow is assumed to be laminar (e.g., where the fluid inertia is neglected because of the low flow speeds):

$$\frac{\partial}{\partial x}\left(\rho h^3 \frac{\partial P}{\partial x}\right) + \frac{\partial}{\partial y}\left(\rho h^3 \frac{\partial P}{\partial y}\right) = 6\mu U \frac{\partial}{\partial x}(\rho h) + 12\mu \frac{\partial(\rho h)}{\partial t} \qquad \text{(A2)}$$

The first term on the right side can be dropped since there is no high speed relative motion $(U = 0)$ between the seal and the adjacent wall. For reference purposes the seal will be moved across the wall at speeds of the order of 1 in./sec which is not sufficient to generate a film between the seal and the wall. The transient term is dropped since only the steady-state solution is desired. The side-flow term $(\partial P/\partial y)$ is also dropped since the seal is long in relation to the effective gaps.

Solution of the remaining differential equation requires a relation between the density and the pressure. For generality the polytropic expression is assumed:

$$\left(\frac{\rho}{\rho_o}\right)^n = \frac{P}{P_o} \qquad \text{(A3)}$$

where n is the polytropic exponent. The two limiting cases for this expression are obtained with $n = 1$ for the isothermal flow assumption (e.g., $\partial T/\partial x = 0$) and $n = c_p/c_v$ for the adiabatic flow assumption (e.g., n equals 1.4 for air).

As others have found (Refs. 3.6 to 3.8) the gas flow can be treated isothermally. Any difference in temperature between the gas and adjacent surfaces is quickly eliminated because of three important factors: 1. the thermal mass of the gas is small relative to that of the adjacent surfaces; 2. the thin film allows heat to conduct quickly through the film; and 3. the flow velocity is small so the temperature difference is eliminated near the seal inlet. Hence for practical cases the isothermal flow assumption ($n = 1.0$) is valid.

Since gas flowing through these small gaps is quickly quenched to the bulk seal/wall temperature, this is the temperature used for the gas in the analyses. Following the isothermal assumption, the compressibility expression relating density and pressure is the ideal gas law:

$$P = \rho RT \tag{A4}$$

Substituting this expression into the simplified Equation (A2) results in the following differential equation to be solved for the pressure distribution:

$$\frac{\partial}{\partial x}\left(Ph^3 \frac{\partial P}{\partial x}\right) = 0 \tag{A5}$$

The above equation can be further simplified since the film height is assumed constant across the wafer surface (e.g., $\partial h/\partial x = 0$), and by noting:

$$\frac{1}{2}\frac{\partial^2 P^2}{\partial x^2} = \frac{\partial}{\partial x}\left(P\frac{\partial P}{\partial x}\right) \tag{A6}$$

Following the above derivations, the following simplified differential equation results:

$$\frac{\partial^2 P^2}{\partial x^2} = 0 \qquad \text{(A7)}$$

Solving this equation results in equations for pressure as a function of x for the region upstream of the seal and in narrow gap between the seal and the adjacent wall:

$$P^2 = \begin{cases} P_s^2 - Ax & \textit{Upstream of seal} \\ P_o^2 + B(w - x) & \textit{Through film gap} \end{cases} \qquad \text{(A8)}$$

(Note: For simplicity the following derivation is for the interface between the wafer nose and the adjacent wall. The final equations developed can be modified for the interface between the seal top and seal channel by simply interchanging the required length scales as defined in Fig. 3.9).

The two constants A and B are determined by matching the pressure and mass flow rate across the seal step:

$$A = \frac{1}{g^3}\left[\frac{P_s^2 - P_o^2}{\left(\frac{s}{g^3}\right) + \left(\frac{H_2}{h_2^3}\right)}\right] \tag{A9}$$

$$B = \frac{1}{h_2^3}\left[\frac{P_s^2 - P_o^2}{\left(\frac{s}{g^3}\right) + \left(\frac{H_2}{h_2^3}\right)}\right] \tag{A10}$$

The unit mass flow through the small gap separating the seal and the adjacent wall is found by integrating the velocity profile over the film height h :

$$\dot{m}/L = \int_0^h \rho u dy \tag{A11}$$

The laminar velocity profile u is parabolic and using the nonslip conditions along the seal (e.g., $u = 0$

at $y = 0$) and at the wall (e.g., $u = 0$ at $y = h$) yields:

$$u = \frac{-y(h-y)}{2\mu} \frac{\partial P}{\partial x} \qquad \text{(A12)}$$

Substituting the velocity distribution into the mass flow equation and integrating yields:

$$\dot{m}/L = \frac{-h^3 \rho}{12\mu} \frac{\partial P}{\partial x} \qquad \text{(A13)}$$

Substituting the ideal gas law relation for density and noting that:

$$2P\frac{\partial P}{\partial x} = \frac{\partial P^2}{\partial x} \qquad \text{(A14)}$$

results in:

$$\dot{m}/L = \frac{-h^3}{24\mu RT}\frac{\partial P^2}{\partial x} \qquad \text{(A15)}$$

Differentiating Equation (A8) with respect to x in the region between the seal nose and adjacent wall and substituting the results into Equation (A15) gives:

$$\dot{m}_2/L = \frac{h_2^3}{24\mu RT}\frac{P_s^2 - P_o^2}{\left(\left(\frac{h_2}{g}\right)^3 s + H_2\right)} \qquad \text{(A16)}$$

Examining the ratio h_2/g in the denominator for dimensions typical of the seal one finds that this term for all practical purposes can be ignored. For dimensions typical of the current investigation the ratio of the film thickness (h_2) to the inter-panel gap width (g) is only 0.004. Cubing this small number essentially removes this term from the denominator, since s and H_2 are of the same magnitude.

Simplifying the above expression results in the basic leakage flow equation for flow $(\dot{m}_2/L)$ between the seal nose and the adjacent wall. A similar derivation can be done for flow $(\dot{m}_1/L)$ through the interface between the top of the seal and the top of the seal channel.

Substituting the results of these derivations into Equation (A1) yields:

$$\dot{m}/L = \frac{(P_s^2 - P_o^2)}{24\mu RT}\left(\frac{h_1^3}{H_1} + \frac{h_2^3}{H_2}\right) \qquad \text{(A17)}$$

Check of Assumptions: The assumptions made in applying this theory to the seal leakage were: that the flow was laminar (e.g., Reynolds number <500); that the seal was long (e.g., $L >> h_i$); and that the seal was smooth in relation to the seal gap height (e.g., wafer roughness $< h_i$). These assumptions are now checked using measured maximum flow conditions.

For the seal at maximum pressure differential of 100 psi:

$\dot{m}/L$ = 0.004 lb_m/s-ft

L = 3 ft

μ = 1.22 x 10^{-5} lb_m/s-ft

R_{air} = 53 lb ft/lb_m-°R

T = 76 °F

H_1 = 0.025 ft (0.3 in.)

H_2 = 0.0417 ft (0.5 in.)

P_s = 114.7 psi

P_o = 14.7 psi

The Reynolds number for either of the parallel paths can be written in know quantities as:

$$Re = \frac{\dot{m}_i/L}{\mu} = 160 \qquad \text{(A18)}$$

Since Re is less than 500 the flow is within the laminar regime. Rearranging the basic mass flow rate equations yields an estimate of the effective seal gap height where again it is assumed the two leakage gap heights are equal:

$$h_{eff} = \sqrt[3]{\frac{24\mu RT\,\dot{m}/L}{(P_s^2 - P_o^2)}\left(\frac{H_1 H_2}{H_1 + H_2}\right)} = 0.000039\ ft = 0.00047\ in. \quad \text{(A19)}$$

Since the seal length is much greater than the effective gap height, the second assumption is satisfied. Also the effective seal gap is greater than the roughness of the smooth (32 μin.) wafer surfaces.

Leakage Pressure-Dependence

According to the flow Equation (A17) the leakage flow rate varies with the difference in the squares of the pressure. Plotting the seal leakage rates predicted by the above relation results in the parabolic leakage rate curve shown in Figure 3.10. Also plotted in the figure is the measured room temperature leakage rate. For this case the film thicknesses h_1 and h_2 used in the model were assumed equal and back-calculated from Equation (A9) using the leakage rate measured at an applied pressure differential of 40 psi.

Good correlation between the measured and predicted leakage rates was observed for pressure differentials less than 50 psi. However the leakage model over

predicts the measured leakage rates by 53 percent, at pressure differentials of 100 psi.

The likely cause of the discrepancy is the film heights h_i are not constant but are actually reduced in size as the pressure differential applied across the seal is increased. Figure 3.11 depicts the forces leading to smaller film thickness as the pressure differential is increased. The pressure profiles along the nose and along the top of the seal are parabolic (as shown in Eq. (A8)) and are lower in magnitude than the engine supply pressure P_s exerted along the back and bottom surfaces of the seal. A force balance in each of these two directions provides expressions for the pressure induced contact forces. The resultant forces per unit length in the vertical and horizontal directions for the maximum applied pressure differential of 100 psi are 31 lb/in. and 18 lb/in., respectively. These forces combined with the counter-clockwise moment act to preload the seal wafer against its mating surfaces leading to smaller effective film thicknesses.

Using Equation (A19) effective film heights were calculated as a function of pressure drop across the seal. As is shown in Figure 3.12 the film height

decreases nearly linearly with increasing pressure differential. A least squares regression analysis performed resulted in a strong (correlation coefficient of $R^2 = 0.98$) correlation for a straight line fit through the data points.

The resulting linear equation is:

$$h_{1,v} = h_{2,v} = 4.95x10^{-5} - 1.131x10^{-7}(P_s - P_o)$$
$$h_{i,v} = ft \qquad \text{(A20)}$$
$$P_s \, , \, P_o = lb/sq\text{-}in.$$

Implementing this variable film thickness into Equation (A17) one can recalculate mass flow versus pressure drop. The resulting predicted leakage rates are shown in Figure 3.13. The agreement between measured and predicted leakage rates is very good. The maximum observed discrepancy is only 6 percent at the full 100 psi pressure differential, a significant improvement over the 53 percent discrepancy observed with the fixed film height assumption.

Leakage Temperature-Dependence

The measured leakage rates are plotted versus temperature in Figure 3.14 for a fixed pressure differential of 40 psi. Several trends are noted in this curve. For low to moderate temperatures the leakage rates decrease with increasing temperature. At intermediate temperatures the leakage rates are constant with temperature. Between moderate to high temperatures the leakage rates begin to increase slightly.

A careful examination of the properties of the seal reveals why the leakage rates do not continue to decrease with temperature as suggested by the basic leakage equation (Eq. (A17)).

Thermal Expansion Differences: The coefficient of thermal expansion (CTE) of the aluminum-oxide wafers used in these investigations is nominally half the CTE of the test rig made of engine simulated material (e.g., Inconel). As the three foot rig heats up it axially expands more than the ceramic wafers. During tests it was observed that axial preload applied by the axial preload systems was unable to maintain the wafer faces in contact, except at the extreme ends of the seal. The

resisting friction forces were generated by the high engine pressures combined with the high friction coefficient of the aluminum oxide ceramic. (Note: Clearly, reduced ceramic fiction coefficients possible with advanced solid lubrication techniques under development should improve preload and hence seal leakage performance.) Therefore at the maximum temperature of 1350 °F the differential axial expansion between the wafers and the rig was 0.23 in. Uniformly dividing this differential expansion over the 288 wafers (0.125-in. thick) results in an inter-wafer gap of 0.00079 in. This inter-wafer gap is of the same order of magnitude as the film-heights calculated between the seal and the adjacent wall surfaces, and must be accounted for in the model.

Flow between wafers similar to flow around the wafers can be modelled using the externally pressurized gas film bearing theory.

Flow between wafers represents a third parallel leakage path which can be added to the basic leakage flow Equation (A17) resulting in:

$$\dot{m}/L = \frac{(P_s^2 - P_o^2)}{24\mu RT}\left(\frac{h^3_{1,v}}{H_1} + \frac{h^3_{2,v}}{H_2} + \frac{Ngh^3_{CTE}}{LH_2}\right) \quad \text{(A21)}$$

In this equation the effective inter-wafer spacing is found from:

$$h_{CTE} = (\alpha_{engine\ panel} - \alpha_{wafers})\frac{L\Delta T}{N} \quad \text{(A22)}$$

where N is the number of wafer interfaces (e.g., the number of wafers minus 1), L is the seal length and ΔT is the temperature rise. The film thicknesses $h_{1,v}$ and $h_{2,v}$ are subscripted with a "v" to denote variable film thickness as a function of applied pressure in accordance with Equation (A20). The term g in Equation (A21) is the inter-panel gap width as indicated in Figure 3.9. Comparisons are made between the leakage rates predicted from Equation (A21) and measured leakage rates in the Results and Discussion section of this chapter.

REFERENCES FOR CHAPTER 3

3.1 Steinetz, B.M., DellaCorte, C., and Sirocky, P.J., "On The Development of Hypersonic Engine Seals," NASA TP-2854 (1988).

3.2 Steinetz, B.M., "A Test Fixture for Measuring High-Temperature Hypersonic Engine Seal Performance," NASA TM-103658 (1990).

3.3 Steinetz, B.M., DellaCorte, C., and Tong, M., "Seal Concept and Material Performance Evaluation for the NASP Engine," NASA CP-7045, Vol. VI, Structures, pp. 39-58 (1989).

3.4 Tong, M., and Steinetz, B.M., "Thermal and Structural Assessments of a Ceramic Wafer Seal in Hypersonic Engines," NASA TM-103651 (1990).

3.5 White, F, Fluid Mechanics, McGraw-Hill, New York (1979).

3.6 Ausman, J.S., "Gas Lubricated Bearings," Advanced Bearing Technology, NASA SP-38, E.E. Bisson and W.J. Anderson, eds., pp. 109-138 (1964).

3.7 Constantinescu, V.N., Gas Lubrication, American Society of Mechanical Engineers, New York (1969).

3.8 Licht, L., "Extension of the Conducting Sheet Analogy to Externally Pressurized Gas Bearings," Journal of Basic Engineering, vol. 83, no. 2, pp. 209-212 (1961).

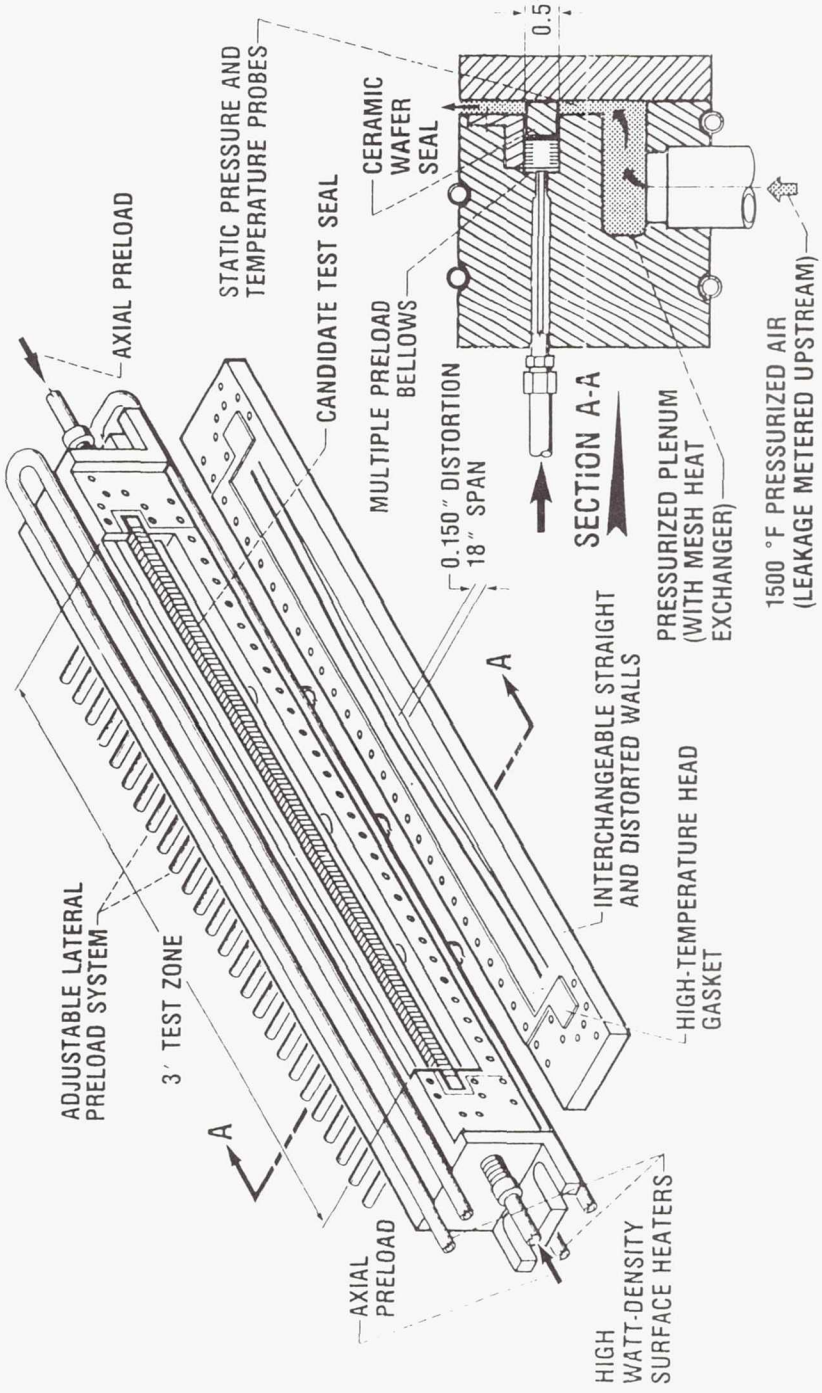

Figure 3.1.—Schemetric of high temperature panel-edge seal test fixture.

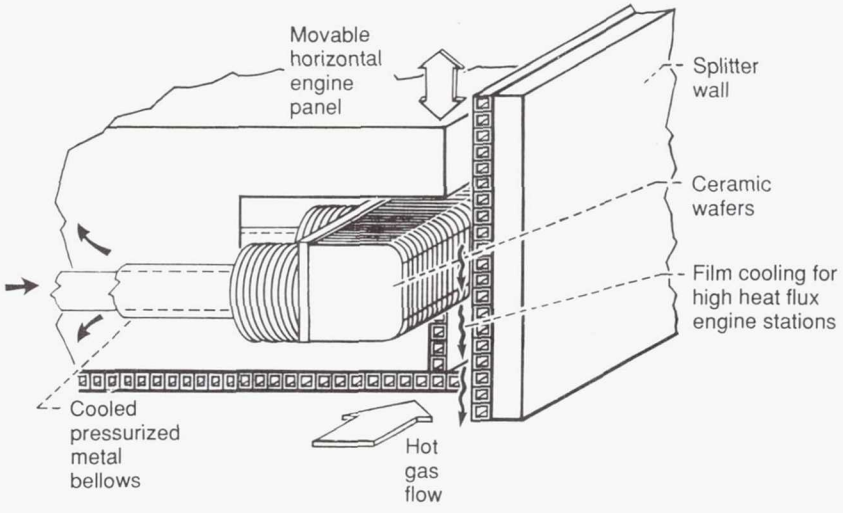

Figure 3.2.—Isometric of ceramic wafer seal installed in the movable engine panel.

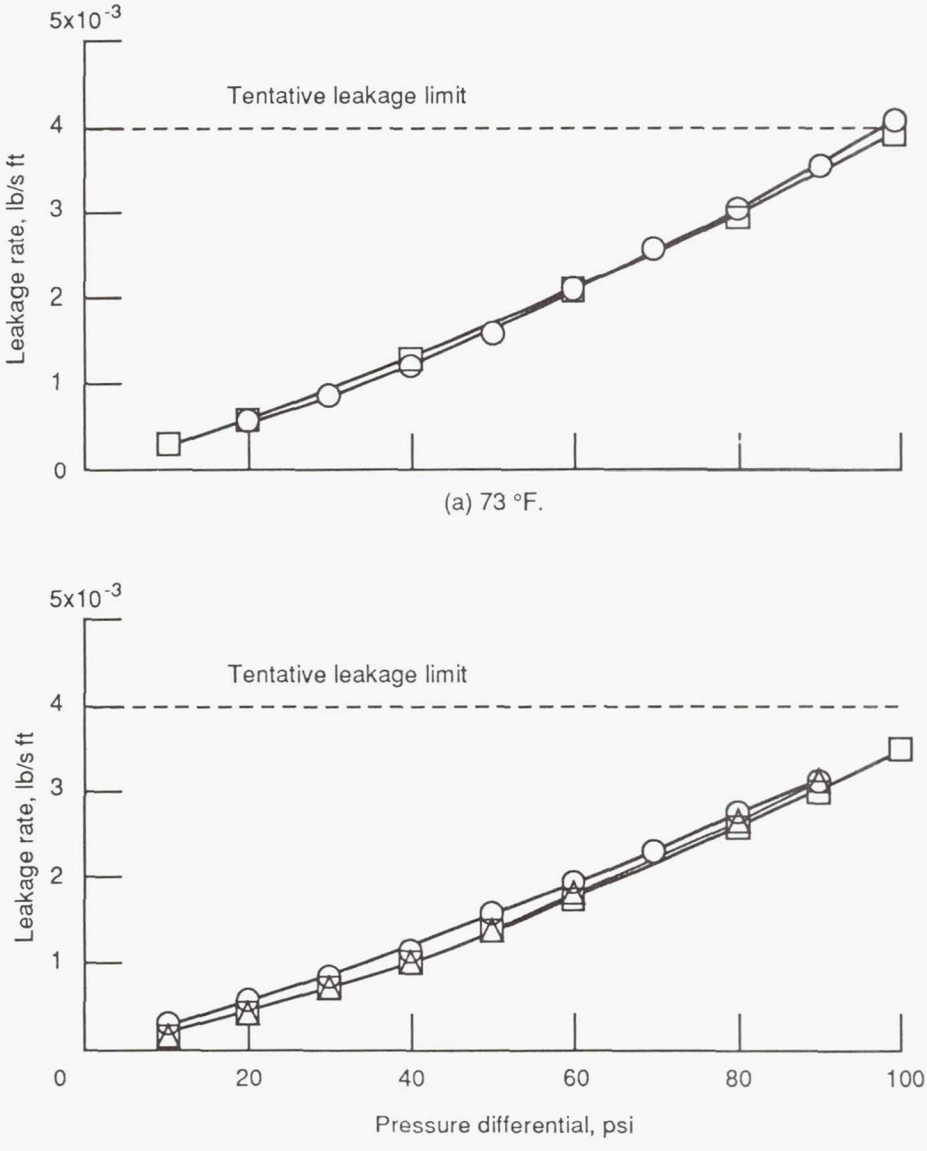

Figure 3.3.—Measured seal leakage rates versus simulated engine pressure differential sealing against the flat wall condition.

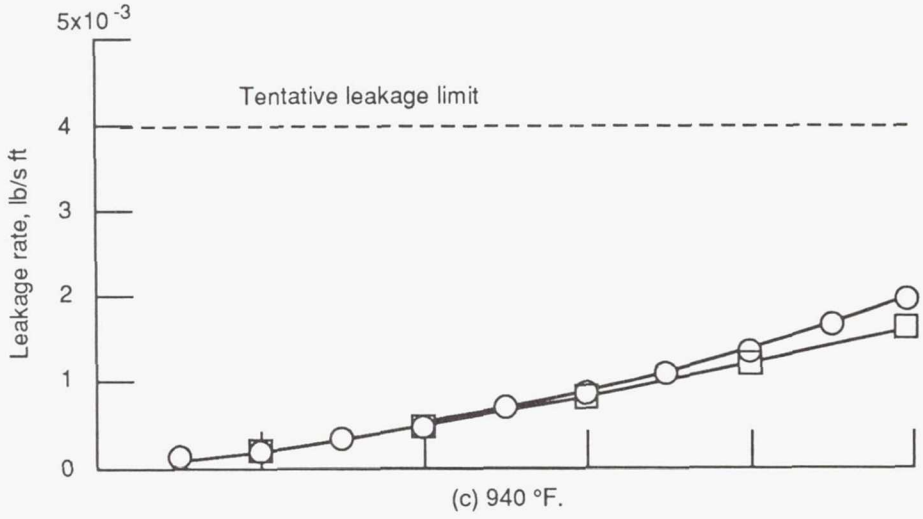

(c) 940 °F.

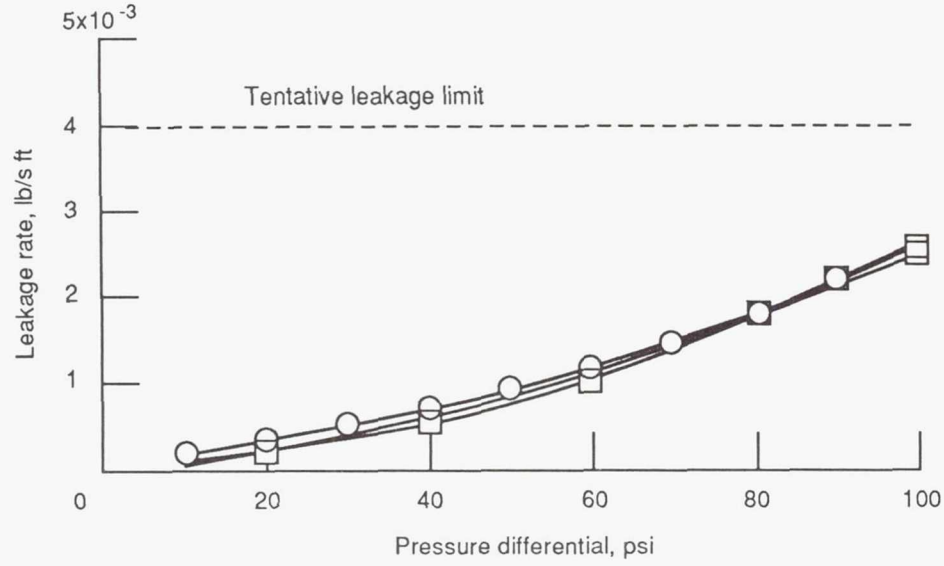

(d) 1350 °F.

Figure 3.3.—Continued.

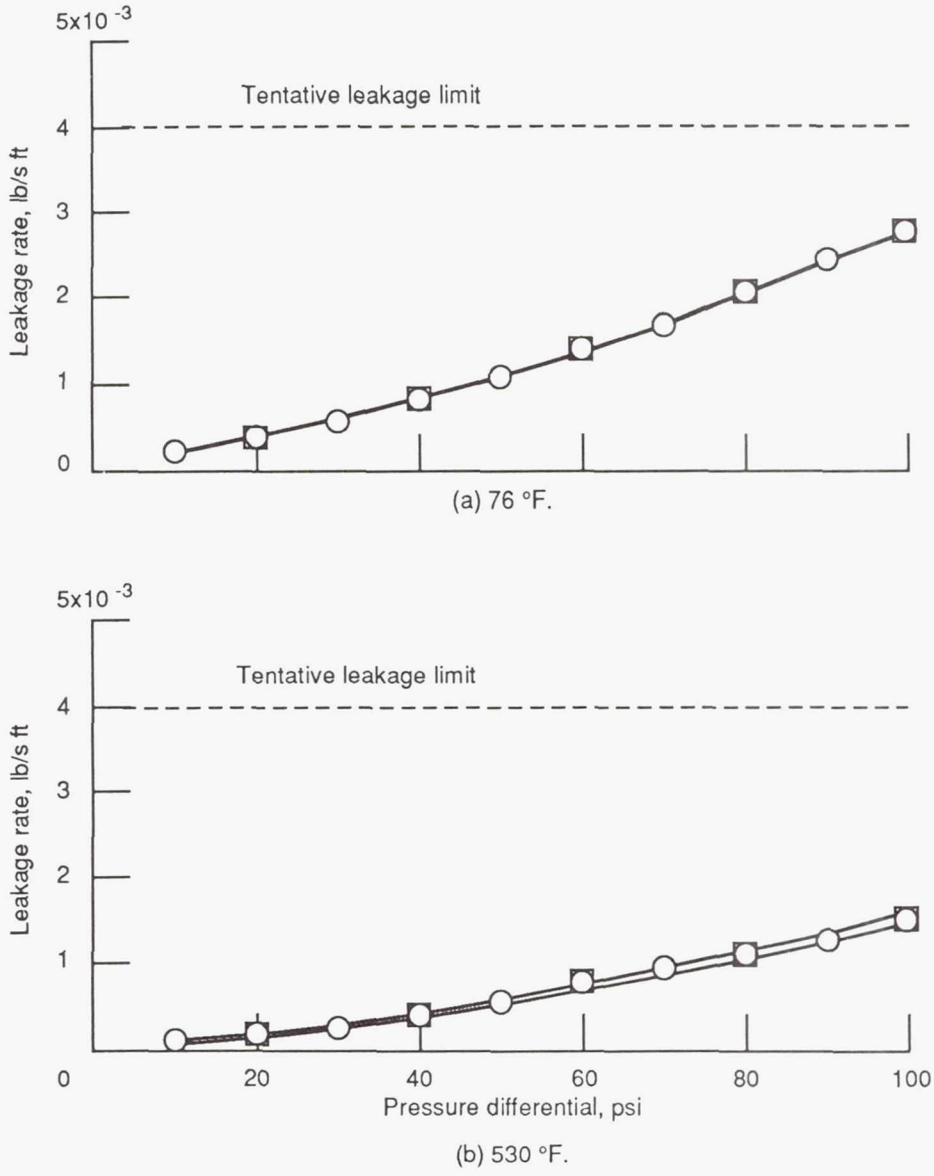

Figure 3.4.—Measured seal leakage rates versus simulated engine pressure differential sealing against the distorted wall condition.

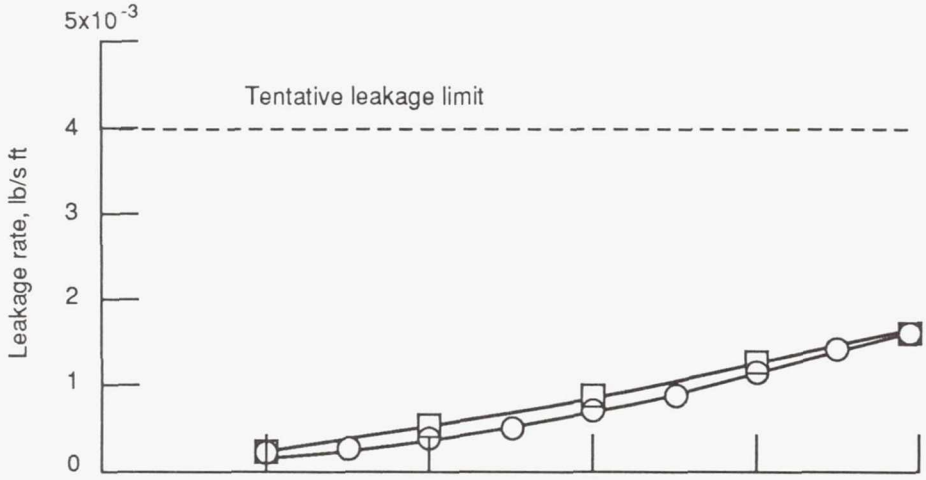

(c) 1000 °F.

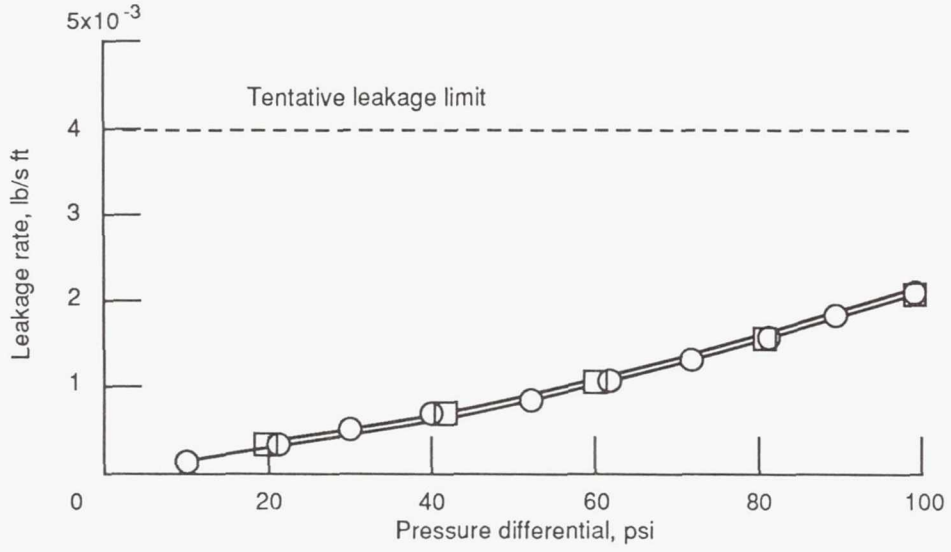

(d) 1350 °F.

Figure 3.4.—Continued.

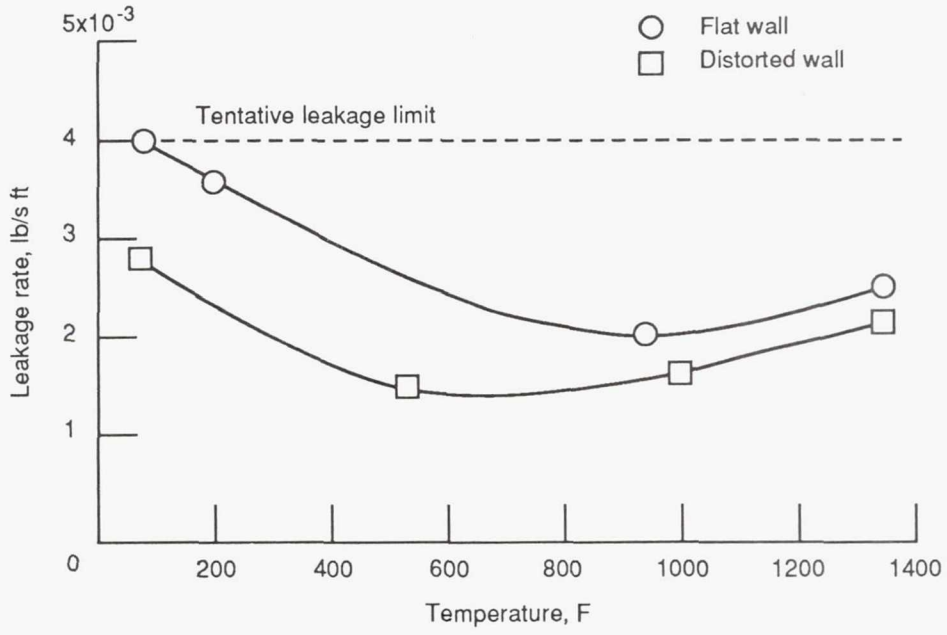

Figure 3.5.—Measured leakage rates versus temperature for flat and distorted wall conditions at a simulated engine pressure differential of 100 psi.

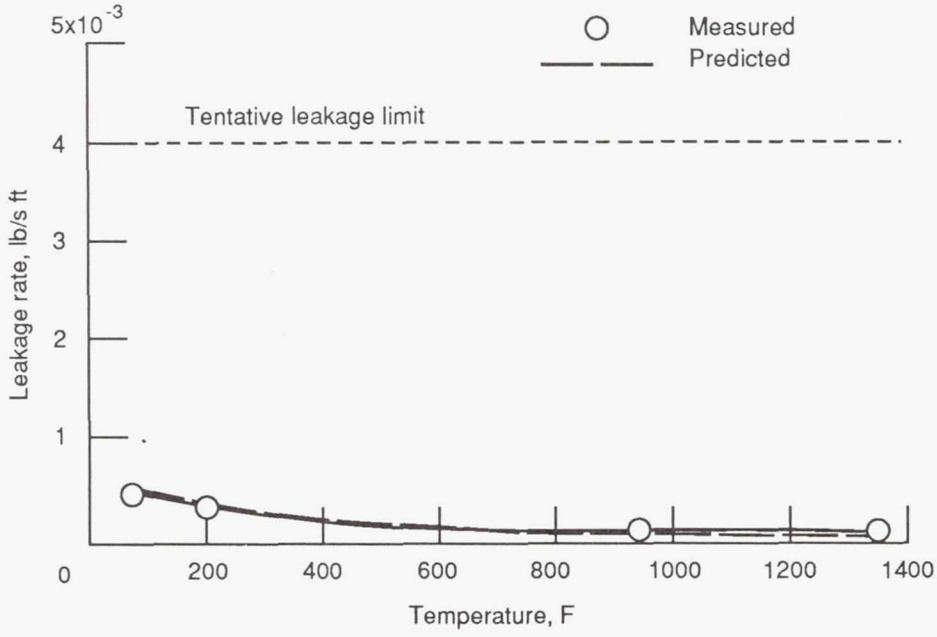

Figure 3.6.—Comparison of measured and predicted leakage rates as a function of temperature for a fixed engine pressure differential of 20 psi.

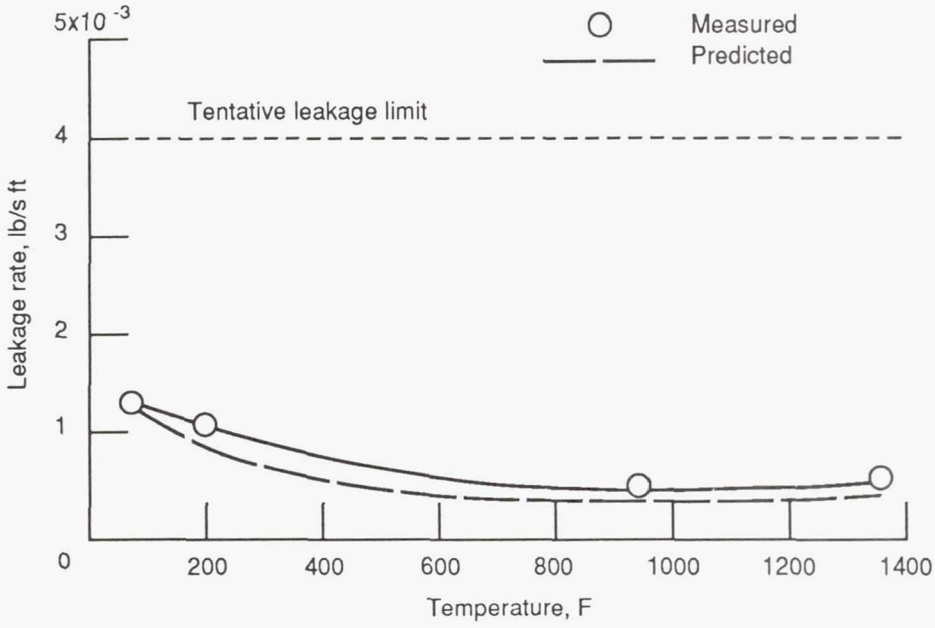

Figure 3.7.—Comparison of measured and predicted leakage rates as a function of temperature for a fixed engine pressure differential of 40 psi.

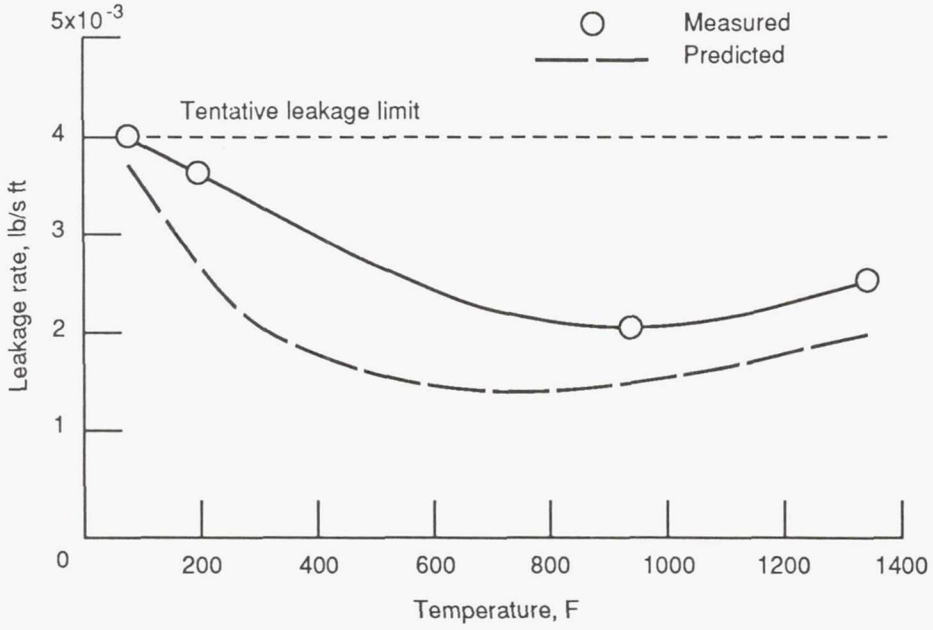

Figure 3.8.—Comparison of measured and predicted leakage rates as a function of temperature for a fixed engine pressure differential of 100 psi.

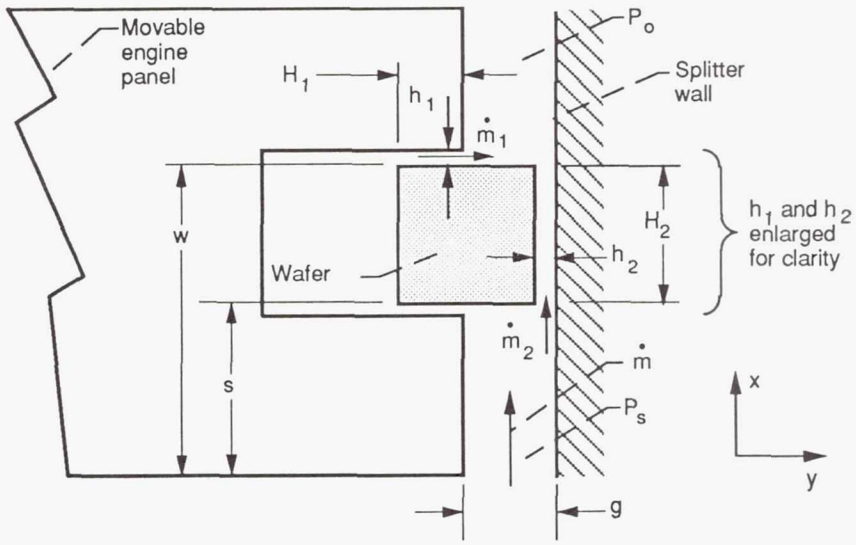

Figure 3.9.—Ceramic wafer seal flow model variables.

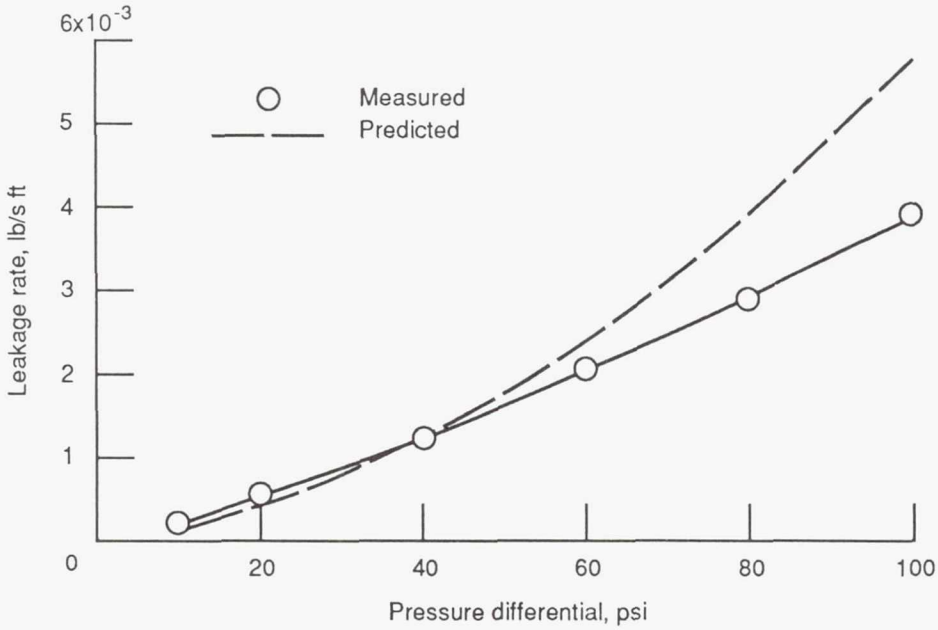

Figure 3.10.—Comparison of measured and predicted leakage rates versus simulated engine pressure differential using fixed film height assumption.

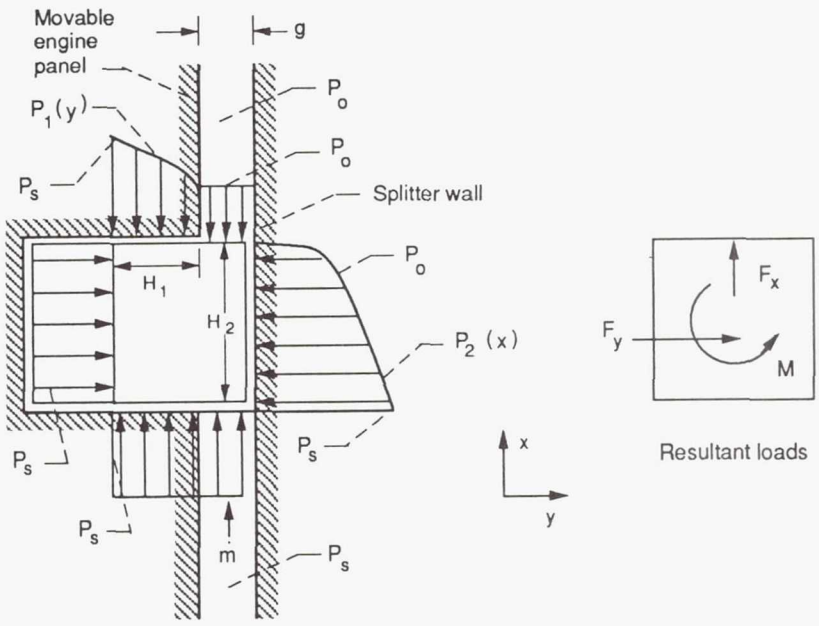

Pressure distribution

$$\sum \frac{F_y}{L} = \frac{F_y}{L} = \int_o^{H_2} \left(P_s - P_2(x)\right) dx$$

$$\sum \frac{F_x}{L} = \frac{F_x}{L} = \int_o^{H_1} \left(P_s - P_1(y)\right) dy + \int_{H_1}^{H_1+g} \left(P_s - P_o\right) dy$$

$$\sum \frac{M}{L} = \frac{M}{L} = \int_o^{H_2} \left(P_s - P_2(x)\right) x dx + \int_o^{H_1} \left(P_1(y) - P_s\right) y dy + \int_{H_1}^{H_1+g} \left(P_o - P_s\right) y dy$$

Pressure profiles: $$P_1(y) = \left\{P_o^2 + \frac{\left(P_s^2 - P_o^2\right)}{H_1}(H_1 - y)\right\}^{1/2}$$

$$P_2(x) = \left\{P_o^2 + \frac{\left(P_s^2 - P_o^2\right)}{H_2}(H_2 - x)\right\}^{1/2}$$

Resultants:

$$\frac{F_y}{L} = \left(P_s - \frac{2}{3}\frac{\left(P_s^3 - P_o^3\right)}{\left(P_s^2 - P_o^2\right)}\right) H_2$$

$$\frac{F_x}{L} = \left(P_s - \frac{2}{3}\frac{\left(P_s^3 - P_o^3\right)}{\left(P_s^2 - P_o^2\right)}\right) H_1 + \left(P_s - P_o\right) g$$

$$\frac{M}{L} = \frac{P_s}{2}\left(H_2^2 - H_1^2\right) + \frac{2}{3}\frac{P_o^3}{\left(P_s^2 - P_o^2\right)}\left(H_2^2 - H_1^2\right) - \frac{4}{15}\frac{\left(P_s^5 - P_o^5\right)}{\left(P_s^2 - P_o^2\right)^2}\left(H_2^2 - H_1^2\right)$$

$$- \frac{\left(P_s - P_o\right)}{2}\left(2 H_1 g + g^2\right)$$

Figure 3.11.—Wafer seal pressure induced loads.

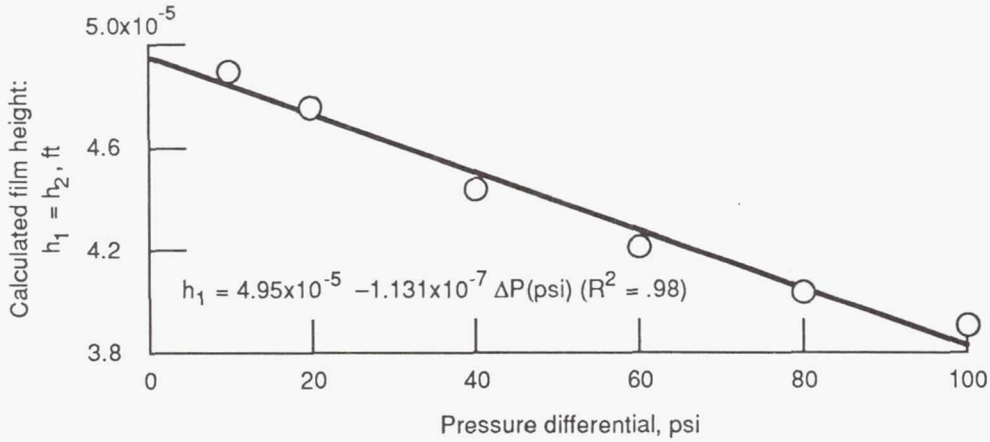

Figure 3.12.—Calculated film height versus simulated engine pressure differential.

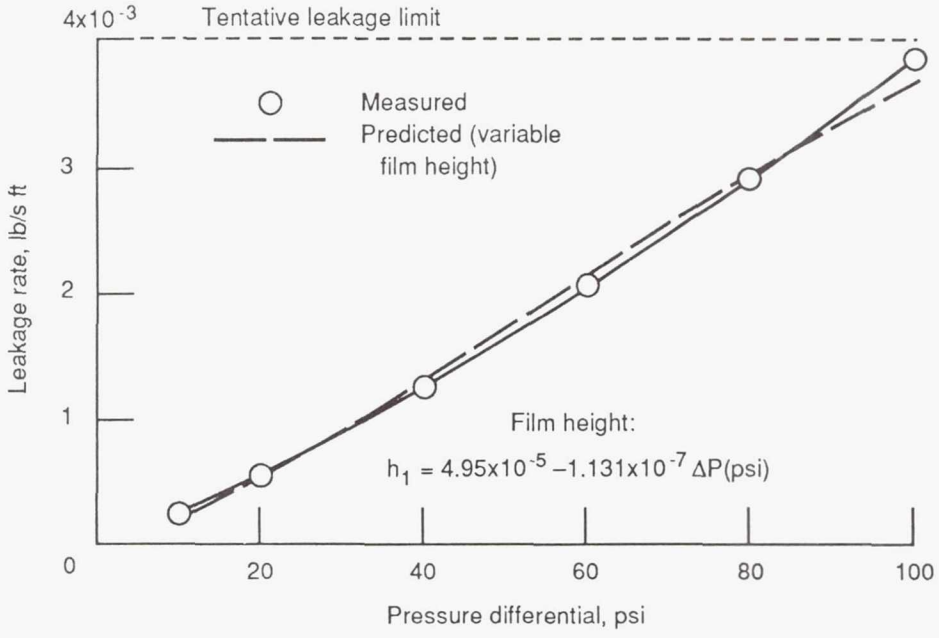

Figure 3.13.—Comparison of measured and predicted leakage rates versus simulated engine pressure differential using variable film height assumption.

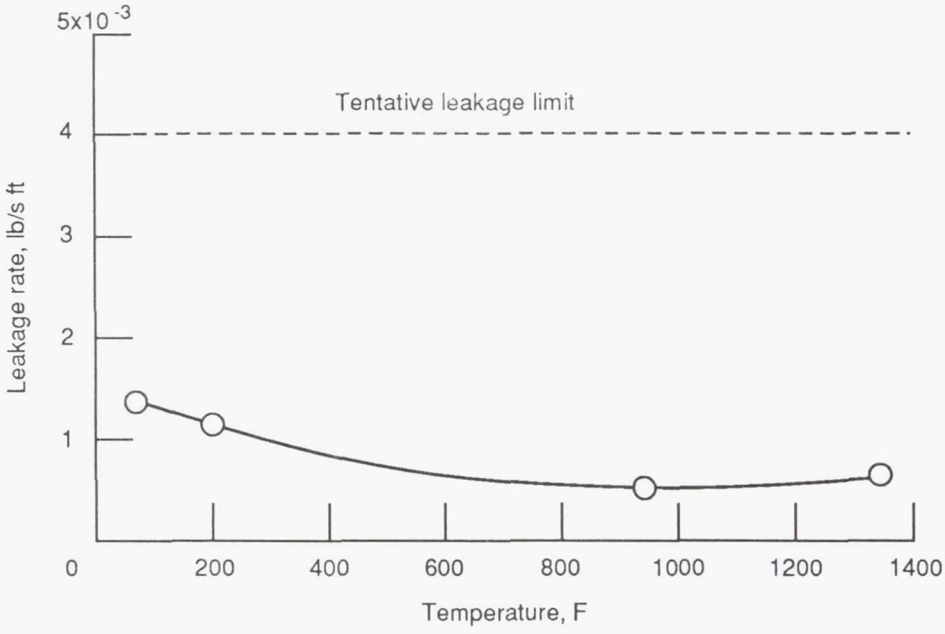

Figure 3.14.—Measured leakage rates as a function of temperature for a fixed engine pressure differential of 40 psi.

CHAPTER 4

4. EVALUATION AND RANKING OF CANDIDATE CERAMIC WAFER ENGINE SEAL MATERIALS

INTRODUCTION

Selecting the best materials for the panel-edge seals described in previous chapters, (also see Refs. 4.1 to 4.4), the seal designer is faced with difficult choices to make. The seal must be strong and light-weight, must survive the thermally aggressive environment, must resist hydrogen embrittlement and oxidation, and must resist chipping and abrasion damage while sliding against the adjacent engine panels.

While investigating materials suitable for the high temperature service conditions of the wafer seal (Figure 4.1), four groups of materials were considered. These materials included carbon-carbon composites, refractory metals, superalloy metals, and engineered ceramics.

Carbon-carbon composites exhibit very high operating temperatures (up to 3000 °F), and have very high strength-to-weight ratios but are rapidly consumed by oxidation. Refractory metals such as Columbium have high

operating temperatures (≈2300 °F) but are heavy and also oxidize rapidly. Both of these materials were rejected as wafer materials because of their poor oxidation performance and the need for failure-prone protective coatings.

Selected superalloy metals are resistant to oxidation and hydrogen embrittlement but have limited maximum operating temperatures (<1800 °F), requiring considerable cooling. Because of their high weight-density, superalloy materials result in heavy seal designs.

Engineered ceramics have been advanced over the past decade and show promise of meeting the challenging seal design criteria. These ceramics can operate at temperatures 800 °F above superalloy materials, and have high specific strength (e.g., strength divided by weight-density) at temperatures exceeding 2200 °F. Ceramic materials are resistant to abrasion due to their high hardness. However, ceramics are brittle by nature and must be properly selected and applied.

Several types of ceramics including aluminum oxides, silicon carbides and silicon nitrides have been improved through improved processing techniques that minimize

volume and surface fracture initiation sites. Techniques employed include reducing grain size, maintaining very high purity, using improved sintering agents, and following strict quality control. Making tradeoffs between these types of ceramics is sometimes difficult since material property data are difficult to assemble because only recently are standard tests being performed over the full temperature range. In assembling property data, one must be careful in that some manufactures will quote material properties (e.g., fracture toughness and flexural strength) using test methods which are known to give overly optimistic results.

Once the material properties are assembled, a means for objectively selecting between competing materials is required to select the best material prior to final detailed and costly design analyses and tests.

The objectives of this study are to investigate and compare a range of thermal, structural, and chemical properties of a selected number of engineered ceramics and objectively rank the relative performance of these materials as they apply to the design of hypersonic engine seals.

MATERIAL REQUIREMENTS

A seal material is required to fulfill several important criteria to be considered viable for hypersonic engine seal design. Listed below are some of these criteria:

1. Operate hot at temperatures $\geq$2000 °F.

2. Have low weight density to minimize seal and subsystem weight to help meet vehicle weight goals and enable the single-stage-to-orbit mission.

3. Have good thermal properties such as high thermal conductivity and high thermal diffusivity to operate in the high heating rates (up to 1500 Btu/sq-ft-s) of hypersonic engines, requiring minimal coolant.

4. Have high strength to sustain the engine thermal and structural loads. Have an acceptable variability of strength properties to provide adequate component reliability for the several thousand of seal elements required in an engine.

5. Have high fracture toughness to resist chipping and fracture during sliding operation.

6. Resist chemical attack including oxidation and hydrogen embrittlement at the high engine gas temperatures.

7. Resist thermal shock during either the extreme heating or cooling transients anticipated during engine operation.

8. Resist leakage flow between wafers by having thermal expansion rates approximating those of the engine panels.

RESULTS AND DISCUSSION

MATERIAL PROPERTY COMPARISONS

Three types of monolithic ceramics were considered in this investigation including aluminum oxide, silicon carbide and silicon nitride. The aluminum oxide was a cold-pressed and sintered Greenleaf[2] Technical Ceramics,

---

[2] Note: Mention of manufacturers is made only for reference purposes and does not constitute a product endorsement by NASA or the U. S. Government.

designated 99 percent-pure grade. The silicon carbide considered was a sintered-alpha material from Carborundum Co., designated Hexoloy SA grade. The sintered-alpha material was chosen because of its high thermal conductivity. This silicon carbide has a conductivity 60 percent higher than high temperature superalloy metals even at high temperature. Three silicon nitrides were considered: two cold pressed and sintered versions from Kyocera Ceramic (designated SN-220 and SN-251); and a reaction-bonded silicon nitride from Garrett Ceramic Components Div., designated GN-10. In subsequent sections of this study, key material properties of these ceramics are compared and a procedure for selecting a material having the optimum balance of material properties is developed.

OPERATING TEMPERATURE

Listed in Table 4.1 are the operating temperatures of ceramics considered in this investigation along with room and high temperature properties compiled from a variety of sources. Of the three types of ceramics considered, aluminum oxide has the highest operating temperature in air environments. Aluminum oxide being an oxide ceramic is stable to temperatures up to 3000 °F. Silicon carbide

maintains useful properties up to 2300 to 2500 °F and silicon nitride ceramics maintain useful properties from 1650 to 2500 °F depending on the type of ceramics considered. The SN-220 material has a 1650 °F upper temperature limit and hence is not further considered in this investigation.

FLEXURAL STRENGTH

Average flexural strengths (four-point bend) for aluminum oxide, silicon carbide and the silicon nitrides meeting the 2000 °F operating temperature requirement are plotted in Figure 4.2 at room temperature and 2200 °F. Three- and four-point bend tests data are typically published in the literature instead of the tension test data because of the relative simplicity and cost savings of specimen manufacture and test, Reference 4.5. In the four-point bend test, a flat specimen is supported and loaded at two points each (Ref. 4.5) loading the center gage section with a uniform bending stress. The four-point bend tests result in more representative strength values because of the larger volume of material that is fully stressed between the two center loading pins. Ceramic specimens following statistical failure behavior are more likely to fail as the specimen volume is increased. The stressed-

volume of the typical four-point bend test specimen is very close to the ceramic wafers, therefore the flexural strengths in Figure 4.2 are considered representative of the expected strengths in the wafer elements.

The Garrett GN-10 and the Kyocera SN-251 silicon nitride materials have the highest flexural strengths of all of the ceramics considered at room temperature and at 2200 °F. High strength is required to sustain the thermal and mechanical stresses induced in the ceramic wafers. In Reference 4.4, a thermal structural analysis was conducted for the silicon carbide material under the Mach 10 engine heating rates. This study concluded that the steady state stresses were 24 ksi, and were below the average tensile strength of 35 ksi (Ref. 4.6) for silicon carbide at 2200 °F. The limited safety margin, the potential for higher transient thermal stresses, and the dispersion associated with ceramic strength data, however, indicated that alternative materials should be considered.

FRACTURE TOUGHNESS

Another important property of ceramic materials is the fracture toughness, K_{1C} (Ref. 4.5). A material's K_{1C} is

a measure of stress intensity at the tip of a crack that will cause a crack to propagate and lead to failure. Therefore the higher the material's fracture toughness the more difficult it is for a crack to propagate. The fracture toughnesses of the ceramic materials considered are plotted in Figure 4.3.

The fracture toughness of silicon nitride is again the highest as a material class. The high fracture toughness combined with the relatively low elastic modulus makes this material more resistant to fracture relative to the other ceramics considered. The SN-251 material has the highest fracture toughness of 6.3 ksi$\sqrt{in}$.

WEIBULL MODULUS

Ceramic materials are brittle by nature and furthermore can have a significant scatter in their strength data. Reference 4.5 demonstrates the typical scatter in strength for ceramics relative to high temperature superalloy metals and shows that the variability can be twice that of metals. Ceramic material strength data follows a Weibull distribution, where strengths do not fall evenly around a median.

One measure of the size of the strength data-scatter is given by the Weibull modulus, often referred to in the literature by "m." The Weibull modulus is the slope of the probability of failure versus the material's strength with the data plotted on log-log coordinates . A higher Weibull modulus indicates a relatively narrow scatter of data, and subject to a certain reliability allows one to more closely predict the likelihood of component survivability subject to given loading condition. Weibull modulus can also be viewed as a measure of the flaw size distribution. For a detailed discussion of Weibull statistics one may refer to (Ref. 4.7). The Weibull modulii for the four ceramic materials are plotted in Figure 4.4 at room temperature in an air

environment. The SN-251 silicon nitride has the highest modulus of 17.

THERMAL PROPERTIES

The intense heating rates and the high gas temperatures found in advanced hypersonic engines require materials that can withstand high thermal transients and require minimal active coolant. A material's thermal diffusivity, which is the ratio of conductivity to the material's density and heat capacity is a measure of the rate at which the heat applied to the seal's exposed surface is diffused through the body. As can be seen by Figure 4.1, a narrow band of the seal wafer surface is subjected to the high heat flux. Enhancing the rate at which the heat applied to the exposed surface diffuses through the wafer and into adjacent cooled engine surfaces lowers the thermal stresses at the material's surface. The thermal loads dominate the structural loads so high diffusivity is key.

Thermal diffusivity is plotted in Figure 4.5 at room temperature and at 2200 °F. At both temperatures, the sintered-alpha silicon carbide has the highest thermal diffusivity because of its high thermal conductivity. It

is noted that from Table 4.1 that the thermal conductivity for all of the ceramics drops with increasing temperature resulting in lower thermal diffusivity at temperature. It is noted from Figure 4.5 that the differences in thermal diffusivity at higher temperatures is considerably less than at low temperatures.

Under steady state heat transfer conditions, the material's thermal conductivity plays a key role. The high (>5000 °F) gas temperatures expected in the engine requires that some form of active cooling be used. In the analysis conducted in Reference 4.4, supplying ambient temperature (70 °F) helium pressurized at 15 psi above engine chamber pressure was sufficient to maintain maximum seal temperatures below the 2500 °F limit of silicon carbide. Materials with lower thermal conductivity at temperature would require proportionately more coolant.

THERMAL SHOCK RESISTANCE OF BRITTLE MATERIALS

Common to everyday experience with glass, brittle materials are susceptible in varying degrees to damage due to thermal shock. The fundamental mechanism of thermal shock is that an applied temperature difference causes thermal strain in materials with a finite thermal expansion rate, which can lead to high local stresses and subsequent fracture. If either the applied temperature or heating rate are high enough, stresses will result that upon encountering a flaw will lead to fracture or degradation of mechanical strength. Hasselman (Ref. 4.8) has recommended several parameters that provide a measure of the brittle material's resistance to thermal shock damage. The two parameters (Refs. 4.5 and 4.8) that apply to the heating conditions of hypersonic engine seals are given below. The resistance parameter R' in Equation (1) is proportional to the sudden temperature difference required to cause an initiated crack to continue propagating.

$$R' = \left(\frac{\gamma}{\alpha^2 E}\right)^{1/2}$$
$$\gamma = \frac{K_{1c}^2 (1-\nu^2)}{2E} \qquad (1)$$

R' is calculated using room temperature properties since these are typically known. In these relations, E is the elastic modulus; γ is the fracture energy; K_{1C} is the material's fracture toughness; α is the material's coefficient of thermal expansion; and ν is Poisson's ratio.

The R' parameter is calculated for all of the ceramic materials and are shown in Figure 4.6. The Kyocera SN-251 material had the highest calculated resistance due to its excellent fracture toughness, low coefficient of thermal expansion and relatively low modulus.

The resistance parameter R'' in Equation (2) is proportional to the maximum allowable rate of surface heating.

$$R'' = \frac{\sigma(1-\nu)\alpha_{TH}}{\alpha E} \qquad (2)$$

R'' is conservatively calculated using the material's high temperature (2200 °F) properties where the strength σ and thermal diffusivity α_{TH} are lowest. (Note: The

tabulated flexural strength was used in place of the tensile strength in Eq. (2).)

The R'' parameters are calculated for each of the ceramic materials and are shown graphically in Figure 4.7. The Garrett GN-10 material exhibits the highest value due to the material's excellent flexural strength at 2200 °F. Though the silicon carbide material is not as strong as the SN-251 material, silicon carbide's high thermal diffusivity can quickly diffuse the heat through the seal wafer and gives this material a relatively high R'' resistance.

THERMAL EXPANSION EFFECTS ON SEAL LEAKAGE

In successfully applying ceramics to advanced heat engine applications, one must account for the potential impact of the difference in the coefficient of thermal expansion (CTE) of the ceramic and the surrounding materials. Typically CTE mismatches pose problems since one is attempting to bond the ceramic to relatively high expansion rate materials. Fortunately in the ceramic wafer seal application the wafers move in the seal channel and require no ceramic-to-metal joining. However the difference in CTEs enters the design process in a

second subtle way. As the engine heats up, the panel and the seal grow according to their respective thermal expansion rates, where the axial direction is of greatest concern. If the panel has a substantially higher CTE than that of the ceramic wafers, narrow inter-wafer gaps can open up between the wafers. If these inter-wafer gaps are too large, the seal will leak unacceptably. Earlier in this work (also Ref. 4.3), a model was developed to predict the leakage flow per unit length ($\dot{m}/L$) past the seal, as a function of: the difference in the squares of the upstream (P_s) and downstream (P_o) pressures; the effective leakage gaps at the top and nose seal contacts ($h_{1,v}$, $h_{2,v}$); the seal contact dimensions (H_1 , H_2); the inter-panel gap width (g); the number of wafer interfaces (N); and the gas properties (μ = gas viscosity; R = universal gas constant; and T = gas temperature):

$$\dot{m}/L = \frac{(P_s^2 - P_o^2)}{24\mu RT}\left(\frac{h^3_{1,v}}{H_1} + \frac{h^3_{2,v}}{H_2} + \frac{Ngh^3_{CTE}}{LH_2}\right) \qquad (3)$$

In this equation the effective inter-wafer spacing is found from:

$$h_{CTE} = (\alpha_{engine\ panel} - \alpha_{wafers}) \frac{L\Delta T}{N} \qquad (4)$$

where N is the number of wafer interfaces (e.g., the number of wafers minus 1), L is the seal length and ΔT is the temperature rise.

From Equations (3) and (4) it is clear that the leakage is dependent on difference in the expansion rates of the wafer seal and the engine panel to the cubed power. Hence this simple material parameter can considerably effect the leakage rates if the difference in the wafer and the engine panel CTEs is too great.

Rearranging Equation (3) one can formulate a leakage flow resistance parameter where leakage flow resistance is defined similar to the electrical analog as the ratio of the driving potential and the resulting flow as:

$$R_F = \frac{P_s^2 - P_o^2}{\dot{m}/L} \qquad (5)$$

specifically:

$$R_F = \frac{24\mu RT}{\left(\frac{h^3_{1,v}}{H_1} + \frac{h^3_{2,v}}{H_2} + \frac{Ngh^3{}_{CTE}}{LH_2} \right)} \qquad (6)$$

Using a tentative leakage flow limit in Equation (5) combined with the maximum anticipated pressure drop of 100 psi across the seal, one can calculate a minimum flow resistance, $R_{F,\min}$. As described in Reference 4.3, the tentative leakage flow limit established for the panel edge seals was 0.004 lb/s-ft of seal length. Substituting these values into Equation (5) results in a minimum flow resistance of:

$$R_{F,\min} = 6.7 \times 10^{10} \frac{lb\ s}{ft^3}$$

Leakage flow resistances were calculated for two candidate high temperature superalloy engine materials at a temperature of 1400 °F. Final engine material selection has not yet been made, so two materials with widely different expansion rates were considered for these calculations to cover the range of possible

expansion rates. For the purposes of this example, it was assumed that the gas temperature, the wafer temperature and the engine panel temperature were all equal to 1400 °F. It is recognized that engine gas temperature and hence the seal temperature can be substantially higher than this. If they were higher, however, the calculated resistances would be even higher than that calculated herein.

The first superalloy material considered is a relatively high expansion alloy HS-188. HS-188 is a cobalt-based alloy that has excellent high temperature ultimate and creep strengths, good oxidation resistance, and is resistant to hydrogen embrittlement (Ref. 4.9). From an expansion-rate point of view, HS-188 (CTE = 9.0×10^{-6} in./in. °F at 1400 °F) is representative of the high CTE materials under consideration for the hypersonic engine panels.

The second engine panel material considered was Incoloy 909, (Ref. 4.10). Incoloy 909 is a nickel-based superalloy but is formulated without chromium to specifically have low expansion rates. The absence of the chromium limits its high temperature oxidation resistance to temperatures below 1200 °F. Above these

temperatures some form of oxidation resistant coating is required and the strength is somewhat limited. Incoloy 909 is also resistant to hydrogen attack. From an expansion-rate point of view Incoloy 909 (CTE = 6.1×10^{-6} in./in. °F at 1400 °F) is representative of the low CTE materials under consideration for the engine panels, including titanium alloys.

Flow resistances for wafer seals made of each of the four candidate ceramics "mounted" in each of these engine materials were calculated and are graphically shown in Figure 4.8. The dashed horizontal line in the figure is the minimum flow resistance calculated using Equation (6) above. High expansion rate aluminum oxide meets the flow resistance parameter for both engine materials. Aluminum oxide wafers 0.125 in. thick were successfully tested earlier in this work (see also Ref. 4.3) in an Inconel X-750 test fixture simulating the engine. (Note: For reference Inconel X-750 and HS-188 have nearly identical thermal expansion rates, so the difference in wafer and panel CTEs and hence leakage flow resistances would be similar). The leakage flow rates were below the tentative leakage limit at 100 psi at 1350 °F.

The low expansion rate silicon carbide and silicon nitride ceramics fell below the minimum resistance by 18 and 23 percent respectively when "mounted" in the high expansion rate HS-188 simulated engine material. However, the flow resistances of each of these ceramics exceeded the minimum resistance by considerable margins when "mounted" in the low expansion rate Incoloy 909 engine material.

Final selection of the engine material will not be made for some time in the future. If a high expansion rate material is used for the engine panels, there are several kinematic approaches that can be considered to overcome the differential axial thermal expansion between the ceramic and the engine panels. One approach invented by the author is depicted in Figure 4.9. In this approach, the wafer pieces are manufactured in wedge shaped pieces and are loaded in the seal channel in an alternating fashion. The wafers are designed with appropriate dimensions so that as the engine panel and seal heat up, the bellows pressing against the backsides of the wafers convert lateral motion into axial growth of the wafer stack to accommodate the thermal expansion mismatch. The wafers are designed with "truncated" tips so that as the expansion occurs the pin-hole size leakage

paths existing at room temperature seal at the design condition. The wafer wedge angles and solid film lubricants are selected such that the friction coefficients between the wafers is less than the tangent of the wedge angle so that the wedges disengage upon cool down.

FRICTION COEFFICIENTS

Another parameter requiring consideration in sliding seal design are friction coefficients and seal wear. For the wafer seal design there are two classes of sliding seal contact: ceramic-to-metal sliding as the seal is slid against the sidewall and actuated in its seal channel; and ceramic-to-ceramic sliding between the adjacent wafers as the wafers move relative to one another to accommodate engine sidewall distortions.

Unlike long-life face-seals, the seal sliding speeds are relatively slow. Using the high temperature pin-on-disk tribometer at NASA Lewis (Ref. 4.11), friction coefficients for low-speed sliding contacts were generated at room and elevated temperatures for the general classes of ceramics considered herein. In the tribometer shown in Figure 4.10, a hemispherically shaped

pin is held in sliding contact against the face of a spinning or oscillating disk depending on test conditions. The friction coefficients are determined as the ratio of the measured tangential and applied normal loads.

Ceramic friction coefficients were measured at room temperature and at 1650 °F sliding against either Inconel X-750, simulating the engine sidewall material, or against themselves. Maximum contact stresses were between 61 and 75 ksi for the ceramic-to-ceramic contacts and between 54 and 58 ksi for the ceramic-to-metal contacts.

The ceramic-to-ceramic friction coefficients were all quite high (see Table 4.2) ranging from 0.5 to 0.8. Advanced high temperature solid film lubricant approaches (Ref. 4.12) are under development to reduce these friction coefficients to acceptable levels (e.g., ≈0.4) to minimize the chances of binding between adjacent wafers. The ceramic-to-metal friction coefficients were high at room temperature but decreased to 0.3 to 0.35 at high temperature where the metal oxide begins to act as a solid film lubricant.

ENVIRONMENTAL EFFECTS

Seal materials considered for these hydrogen-fueled hypersonic engines must resist hot hydrogen and oxidation attack. Hydrogen embrittlement at temperature is a condition in which the small energetic H_2 molecule weakens the grain boundaries and degrades the parent material strength. Perhaps one of the most dramatic forms of hydrogen embrittlement is when the H_2 diffuses into a material and combines with free carbon. In this case methane is formed and if oxygen is present the mixture can combust locally within the material.

Limited testing has been conducted to assess the effects of hot hydrogen on these engineered ceramics. Strength tests and thermodynamic analyses recently performed at NASA Lewis have shed considerable light on this important issue. In this investigation (Ref. 4.13) the effects of moist hydrogen on the flexural strengths of silicon nitride, silicon carbide, and aluminum oxide amongst other ceramics were assessed from room temperature up to 2550 °F. As is indicated in Table 4.1 taken from Reference 4.13, the hydrogen had little if any effect on the strength of each of the three types of ceramics. The

noted loss in strength is no different than the strength loss simply due to the higher operating temperature.

The metal bellows and the seal backing strip which form the lateral preload system of the seal were both made of Inconel 718. This material shows only minor hydrogen weakening (Ref. 4.9) and is used extensively in the hydrogen-oxygen Space Shuttle Main Engines.

Oxidation Aluminum oxide being an oxide is typically stable in an oxygen or air environment at high temperature (Ref. 4.5). Therefore no variation in properties are anticipated due to the presence of oxygen.

The carbide and nitride classes of ceramic typically react with oxygen. The reaction with silicon, however, quickly forms a protective SiO_2 surface layer (Ref. 4.5) under partial pressures of oxygen of interest. This process is known as passive oxidation and under these conditions, further oxidation will be slow and be controlled by oxygen diffusion though the SiO_2 layer. Oxidation has been noted to reduce strength in Si_3N_4 at high temperatures but requires somewhat longer times than the few hundred hours of life for these seals. Conservatively, however, one should conduct tests in a

simulated environment to make the final assessment. Also prior to final selection the effects of steam on material properties should be assessed.

The Inconel 718 material used for the bellows preload system and seal backing strip have good mechanical properties in air environments and temperatures up to 1300 °F (Ref. 4.14).

SEAL WEIGHT

Because of the significant lengths (≈40 ft) of seal required per engine, designers must incorporate minimum weight materials and design concepts. Ceramics offer significantly lower weight densities 1/3 to 1/2 than those of superalloy metals, resulting in a low weight seal design.

The seal weights were determined by measuring the weight per linear foot of the half-inch seal wafers, 12 Inconel bellows and the thin 0.030 in. seal backing strip between the bellows and the wafers (see Fig. 4.1). The dry seal weights (e.g., without seal coolant) for all of the various ceramics considered are tabulated in Table 4.1. The seal weights varied from 0.61 lb/ft for silicon

carbide and one silicon nitride to 0.70 lb/ft for the aluminum oxide. For comparison purposes, the weight of a Inconel wafer seal (0.5-in. square) would be 1.12 lb/ft, 60 percent higher than the ceramic designs.

OBSERVED PERFORMANCE OF SiC AND Al_2O_3

To establish an understanding of the fabrication processes involved with high temperature ceramics and to measure leakage rates of the ceramic wafer seal concept, wafer specimens were made from the Greenleaf cold-pressed and sintered aluminum oxide, and the Carborundum sintered-alpha silicon carbide. Considerable leakage testing has already shown the successful leakage performance of the aluminum oxide wafer seal. Shown in Figure 4.11(a) are some aluminum oxide wafers after about 20 hr of accumulated high temperature (up to 1350 °F) and high pressure (up to 100 psi) testing. The wafers show only a slight change in color. Some of the blackening could be a result of being in contact with the Inconel X-750 rig that formed a greenish-black passivating oxide layer during the tests. There was no observed chipping of the wafer corners or sealing surfaces.

The silicon carbide wafers are shown in Figure 4.11(b) after a single test at room temperature at pressures up to 100 psi. Some of the wafer corners chipped or spalled-off during the tests. This result was a surprise since the wafers were subjected to relatively benign conditions. The leakage rates measured for these wafers were considerably higher than those measured for the aluminum oxide wafers. The wafer corner chipping problem allowed a considerable amount of air to leak past the seal.

Radiography of the seal wafers performed after the tests revealed inclusions and impurities in the wafers with some found near the corners. Some of the chips seemed to originate from minute chips left over form the wafer manufacturing process. These minute chips and material imperfections (e.g., crack initiation sites) combined with silicon carbide's low fracture toughness are believed to have led to the corner fracturing.

It is clear from this experience that silicon carbide's poor fracture toughness limits its application as a seal material for the hypersonic engines. It is noted however that considerable material improvements are underway at various manufacturers to overcome the noted limitations.

If these limitations are overcome, then designers can reconsider this material and potentially capitalize on the material's excellent thermal properties.

SEAL MATERIAL RANKING

The key mechanical, thermal, and leakage performance parameters discussed above were combined into an overall seal material ranking parameter to give an objective relative ranking of the materials. The material's thermal properties are well represented in the ranking parameter because of the severe thermal environment in which the seals must operate. In this study, each of the performance parameters were designed such that high values indicated good performance. Because each of the parameters play a near equal role in determining the materials performance in the final application, the overall material ranking parameter R_M was calculated as a simple sum of the elemental performance parameters according to the following equation:

$$R_M = \frac{\sigma_{flex,2200}}{\rho} + R' + R'' + K_{2200} + R_F + K_{1C} + m_{Weibull} \qquad (7)$$

where:

$\frac{\sigma_{flex,2200}}{\rho}$ = 2200 °F *Specific flexural strength*

R' , R'' = *Thermal resistance parameters*

K_{2200} = 2200 °F *Thermal conductivity*

R_F = *Flow resistance parameter*

K_{1C} = 70 °F *Fracture toughness*

$m_{Weibull}$ = 70 °F *Weibull modulus*

In this expression, the elemental parameters are all of different order of magnitudes. To allow each parameter to enter the basis with equal weight, the elemental parameters had to be normalized before summing them. The elemental parameters were normalized with respect to the values of the elemental parameter for the strongest ceramic considered, GN-10. It is also noted that the lead term was the material's specific strength (e.g., strength-to-density ratio) which emphasizes the need for strong and light-weight seal structures. The material friction coefficients were not included in the ranking parameter because their nearly equal magnitudes would not help discriminate between the materials.

Plotted in Figure 4.12 are the results of these studies. Since the flow resistance parameter depends on the engine panel material in which the seal is mounted, two ranking parameters are given for each of the ceramics, as noted. The study shows that the silicon nitride material as a material class outperforms the aluminum oxide and the silicon carbide for this seal application. This assumes however that the seal is mounted in an engine material with a relatively low expansion material such as Incoloy 909 or a titanium alloy. If the seal is to be mounted in the high expansion rate material then the noted shortfall in seal flow resistance can be addressed through methods discussed. As shown in Figure 4.12, the high fracture toughness, high Weibull modulus silicon nitride SN-251 had the highest overall ranking. Repeating the calculations of R_M using the toughest material (e.g., SN-251) as the normalizing basis as opposed to the strongest material (e.g., GN-10) resulted in the same highest ranking material, SN-251.

A designer choosing between the two silicon nitrides for the final engine application would have to consider such things as: wafer reliability; long term material properties; detailed thermal-stress analyses, as

conducted in Reference 4.4; and finally material cost and availability.

Furthermore, ceramic materials are continuously evolving and improving. Hence over the typical design cycle, designers must monitor material developments (e.g., whisker-toughened ceramics, etc.) to optimize the end product. Also, working closely with the material manufacturers, the seal designer and manufacturers may be able to slightly change the material chemistry or sintering aids to improve material performance for the final specific application.

SUMMARY AND CONCLUSIONS

An overview has been presented of the key mechanical, thermal, and chemical properties of several engineered ceramics as they apply to the design of high temperature seals for advanced hypersonic engines, including those for the National Aerospace Plane (NASP). Ceramics offer high operating temperatures, excellent strength at temperature, and low weight density (1/3 to 1/2 that of superalloy metals) resulting in a low weight seal design. The ceramic materials considered resist H_2 attack and have limited oxidation at high temperature.

The ceramic materials reviewed included: a high purity cold-pressed and sintered aluminum oxide (Greenleaf Technical Ceramics, 99 percent grade); a sintered-alpha silicon carbide (Carborundum Co., SA); a hot-isostatically-pressed silicon nitride (Garrett Ceramic Components, GN-10); and a competing cold-pressed and sintered silicon nitride (Kyocera Engineering Ceramics, SN-251).

The key mechanical properties important to engine seal design were examined and compared. The four-point flexural strengths of each of these materials were

reviewed at room temperature and 2200 °F, and in order of increasing strength were aluminum oxide, silicon carbide, SN-251 and GN-10 silicon nitrides. Room temperature fracture toughnesses, a measure of the materials resistance to crack growth, were reviewed and in order of increasing toughness included aluminum oxide, silicon carbide, GN-10 and SN-251 silicon nitrides. Weibull modulii which indicate the amount of data scatter in material strength were reviewed and in order of decreasing data scatter include silicon carbide, aluminum oxide, and GN-10 and SN-251 silicon nitrides.

Because of the severe thermal environment of advanced hypersonic engines, good thermal properties such and thermal diffusivity and thermal conductivity are key for good thermal performance of the seal. Thermal diffusivity, a measure of the rate at which the seal material can diffuse sudden thermal transients, were presented for room temperature and 2200 °F and in increasing order included aluminum oxide, GN-10 and SN-251 silicon nitrides, and silicon carbide. The thermal conductivity, a measure of amount of active coolant required to maintain seal temperatures, follows the same order.

Two thermal shock resistance parameters were examined for relative ranking amongst the ceramic materials. The first parameter measured the ceramic's resistance to crack growth and is proportional to the material's fracture toughness and inversely proportional to the material's modulus and expansion coefficient. Because of silicon nitride's excellent fracture toughness, low expansion rate, and relatively low modulus, silicon nitrides have the highest resistance to crack growth followed by silicon carbide and aluminum oxide.

Localized thermal stresses caused by localized heating anticipated in the wafer seals can also lead to thermal fracture. A parameter measuring the material's resistance to sudden intense heating was calculated for each of the materials and is proportional to the material's strength and thermal diffusivity and inversely proportional to the elastic modulus and expansion coefficient. In order of increasing resistance to intense heating induced fracture the ceramics included aluminum oxide, silicon carbide, and SN-251 and GN-10 silicon nitrides.

For optimal performance the seal must virtually eliminate leakage. Mounting the relatively low expansion rate

ceramic materials in relatively high expansion rate engine panels without seal axial preload raises the possibility of opening small inter-wafer gaps between the wafers as the seal and panels heat to operating temperature. Using a leakage flow resistance parameter, the effects of relative differences in seal and engine panel expansion coefficients were examined and compared to a minimum flow resistance. Mounting the wafer seal in a relatively high expansion rate engine material (e.g., HS-188) only the aluminum oxide ceramic met the minimum leakage flow resistance, with the other ceramics about 33 percent below the minimum. However, mounting the wafers in a relatively low expansion rate engine material (e.g., Incoloy 909) comparable to several of the engine materials under consideration, the calculated flow resistance was considerably above the minimum for all of the ceramics considered.

Based on these findings the following results were obtained:

1. Though sintered-alpha silicon carbide ceramics have excellent thermal properties, their limited strength and fracture toughness limit there application in hypersonic engine seals.

2. The superior strength, toughness and moderate thermal properties of advanced silicon nitride ceramics such as SN-251 show great promise for application as hypersonic engine seals if mated with low to moderate expansion rate engine materials.

REFERENCES FOR CHAPTER 4

4.1 Steinetz, B.M., DellaCorte, C., and Sirocky, P.J., "On The Development of Hypersonic Engine Seals," NASA TP-2854 (1988).

4.2 Steinetz, B.M., "A Test Fixture for Measuring High-Temperature Hypersonic-Engine Seal Performance," NASA TM-103658 (1990).

4.3 Steinetz, B.M., "High Temperature Performance Evaluation of a Hypersonic Engine Ceramic Wafer Seal," NASA TM-103737 (1991).

4.4 Tong, M., and Steinetz, B.M., "Thermal and Structural Assessments of a Ceramic Wafer Seal in Hypersonic Engines," NASA TM-103651 (1990).

4.5 Richerson, D.W., Modern Ceramic Engineering, Marcel Dekker, New York (1982).

4.6 Hecht, N., "Mechanical Properties Characterization of High Performance Ceramic," 27th Automotive Technology Development Contractors Coordination Meeting, Society of Automotive Engineers (1990). (Also to be published in Ceram. Eng. Sci. Proc., no. 7-8, 1991.)

4.7 Weibull, W., "A Statistical Distribution Function of Wide Applicability," J. Appl. Mech., vol. 18, no. 3, pp. 293-297 (1951).

4.8 Hasselman, D.P.H., "Thermal Stress Resistance Parameters for Brittle Refractory Ceramics: A Compendium," Bull. Am. Ceram. Soc., vol. 49, no. 12, pp. 1033-1037 (1970).

4.9 Chandler, W.T., "Hydrogen-Environment Embrittlement and Its Control in High Pressure Hydrogen/Oxygen Rocket Engines," Advanced Earth-to-Orbit Propulsion Technology Conference, NASA CP-2437-VOL-2, R.J. Richmond and S.T. Wu, eds., pp. 618-634 (1986).

4.10 Incoloy 909 Product Catalog, Publication No. IAI-18, Inco Alloys International, Inc. (1987).

4.11 Sliney, H.E. and DellaCorte, C., "A New Test Machine for Measuring Friction and Wear in Controlled Atmospheres to 1200 °C," NASA TM-102405 (1990).

4.12 Steinetz, B.M., DellaCorte, C., and Tong, M., "Seal Concept and Material Performance Evaluation for the NASP Engine," NASA CP-7045, Vol. VI, Structures, pp. 39-58 (1989).

4.13 Herbell, T.P., Eckel, A.J., Hull, D.R., and Misra, A.K., "Effect of Hydrogen on the Strength and Microstructure of Selected Ceramics," NASA TM-103674 (1990).

4.14 Manson, S.S., "Inconel 718," Aerospace Metals Handbook, Article 4103 (1974). (Also see, Kattus, J.R., "Inconel 718," Aerospace Metals Handbook, Article 4103, 1986.)

Table 4.1. Comparison of monolithic ceramic properties

PROPERTY	Temp.	Al_2O_3 99%pure[7]	SiC SA[10]	Si_3N_4 GN-10[12]	Si_3N_4 SN-220[6]	Si_3N_4 SN-251[8]
Mechanical Properties:						
Poisson's Ratio	R.T.	0.30[7]	0.14[10]	0.27[12]	0.28[6]	0.27[13]
Modulus of Elasticity (Msi)	R.T.	54[7]	62[2]	44[12]	43[6]	43
	2200 F	47[7]	58[2]	41	NA	41[14]
4 Point Flexural Strength (ksi) Air Environment	R.T.	50[7]	58[2]	107[11]	86[6]	94[1]
	2200 F	40	58[2]	87[11]	44[6]	73[1]
4 Point Flexural Strength (ksi) at R.T. after 100 hr H_2 exposure at 2200 °F	R.T. after 2200 F expos.	40	58[5]	87[5,11]	NA	73
Fracture Toughness K_{1c} (ksi $\sqrt{in.}$)	R.T.	3.8[7]	2.7[3,15]	5.1[11]	5.2[6]	6.3[1]
Weibull Modulus (m)	R.T.	10	5.1[2]	12[12]	11	17[13]
	As Noted	NA	11.5[2] 2550 F	NA	NA	13[13] 2500 F
Thermal Properties:						
Max Use Temperature (°F)	°F	3000	2500	2200	1650	2500
Thermal Expansion Coefficient (μin./in. °F)	R.T.-2200 F	4.5[7]	2.2[10]	1.7[12]	1.8[6]	1.7[13]
Thermal Conductivity (Btu/h-ft-°F)	R.T.	16[7]	73[10]	25[12]	12[6]	37[1]
	2200 F	3.9[7]	20[9]	11[12]	7[6]	12[13]
Specific Heat (Btu/lb °F)	R.T.	0.18[7]	0.17[9]	0.14[12]	0.16[6]	0.15[13]
	2200 F	0.31[7]	0.31[9]	0.30[12]	NA	0.30[4]
Material Properties:						
Material Density ($lb/in.^3$)	R.T.	0.14[7]	0.11[10]	0.12[11]	0.11[6]	0.12[1]
Seal Dry Weight (lb/linear ft) Includes: Wafers bellows; Inconel strip	R.T.	0.70	0.61	0.64	0.61	0.64

Table 4.1. Continued.

[1] Yoshida, M, Kokaji, A., and Koga, K, "Silicon Nitride for Automotive Applications," SAE Paper 890424 (1989).

[2] Hecht, N., "Mechanical Properties Characterization of High Performance Ceramic," 27th Automotive Technology Development Contractors Coordination Meeting, SAE (1990). (Also to be published in Ceram. Eng. Sci. Proc., no. 7-8, 1991.)

[3] Measured in author's laboratory by Micro-Indentation method Fracture toughness method using Evans calculation method.

[4] Kyocera Corporation Central Research Laboratory Internal Report, Entitled "Properties of SN-260, Table 1."

[5] Herbell, T.P., Eckel, A.J., and Misra, A.K., "Effect of Hydrogen on the Strength and Microstructure of Selected Ceramics," NASA TM-103674 (1990).

[6] Kyocera Engineering Ceramics catalog Information. Catalog No. 4T8912THA. 1989.

[7] Greenleaf Technical Ceramics 99% Purity Alumina. Greenleaf Technical Ceramics Product Catalog Information, Hayward, CA, 94545.

[8] Kyocera Corporation Central Research Laboratory Internal Report No. K41-0003.

[9] DOE report prepared by Garrett AirResearch Manufacturing Co. of America, DOE report page 31-3559.

[10] Carborundum Silicon Carbide Hexoloy SA Grade Catalog Form A12025, May, 1985.

[11] Choi, S.R., and Salem, J.A., "Strength Toughness and R-Curve Behavior of SiC Whisker Reinforced Composite Si_3N_4 with Reference to Monolithic Si3N4," Submitted to Journal of Materials Science (1991).

Table 4.1. Concluded.

[12] Garrett Ceramic Components GN-10 Product Catalog, SPLA-1086A, Torrance, CA, 90509, 1990.

[13] Salem, J.A., Manderschied, J.M., Freedman, M.R., and Gyekenyesi, J.P., "Reliability Analysis of a Structural Ceramic Combustion Chamber," NASA TM-103264 (1990).

[14] Kyocera Corporation Central Research Laboratory Internal Report, "Typical Properties of SN-251 and SN-252."

[15] Dannels, C.M., and Dutta, S.: "Effect of Processing on Fracture Toughness of Silicon Carbide as Determined by Vickers Indentations," NASA TM-101456 (1989).

Table 4.2. Ceramic average friction coefficients

Sliding Condition	Temp.	Silicon Carbide	Silicone Nitride	Aluminum Oxide
Slid against self:	R.T.	0.53	0.70	0.6-0.8
	1650 °F	0.65	0.80	0.6-0.8
Slid against Inconel X-750:	R.T.	0.70	NA	0.5
	1650 °F	0.35	NA	0.3

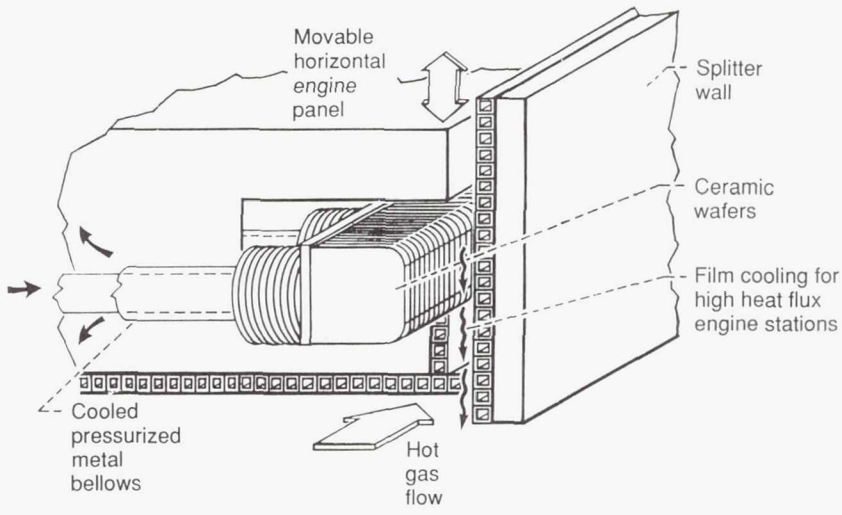

Figure 4.1.—Isometric of ceramic wafer seal installed in the movable engine panel.

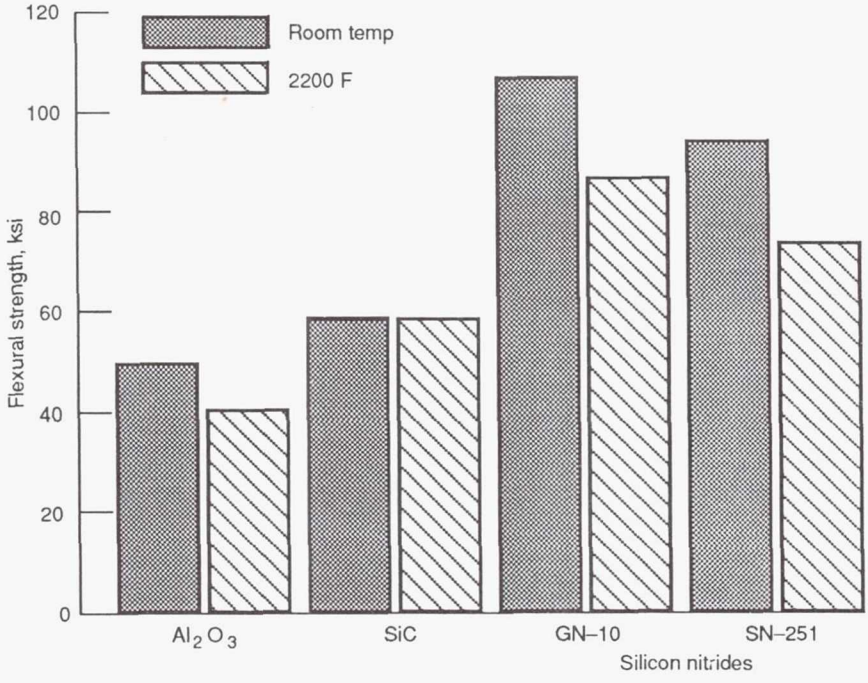

Figure 4.2.—Flexural strengths (four-point bend) of selected ceramics at room temperature and 2200 °F.

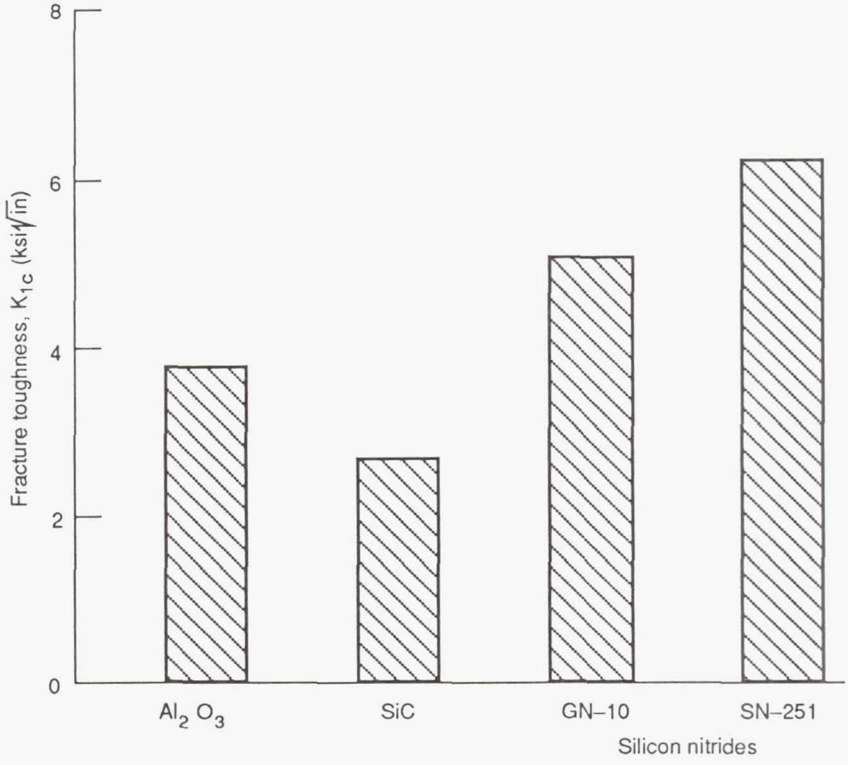

Figure 4.3.—Ceramic material room temperature fracture toughness.

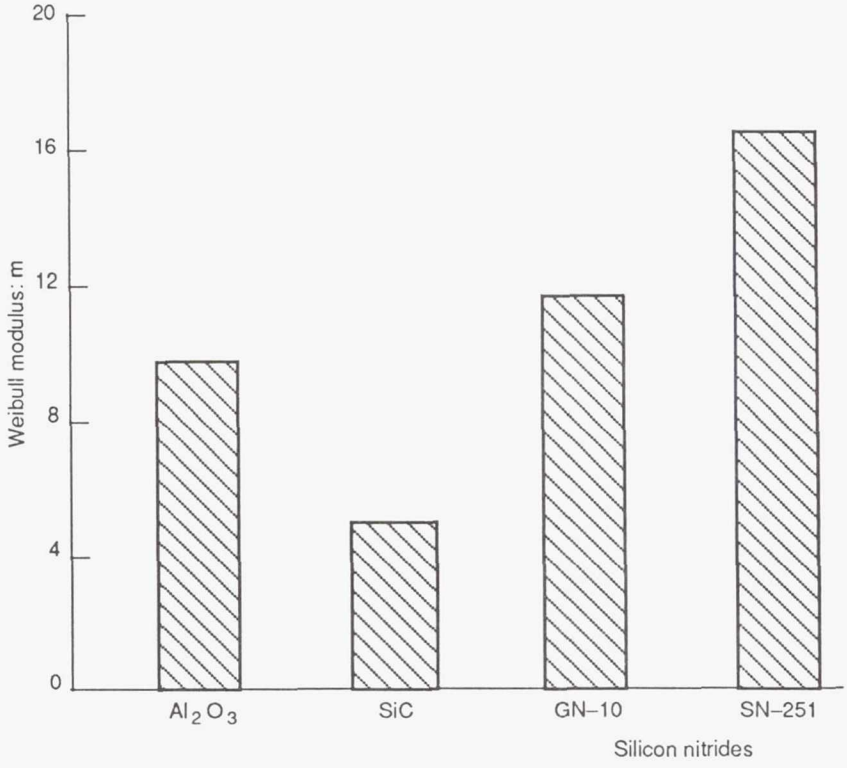

Figure 4.4.—Ceramic material room temperature Weibull modulus.

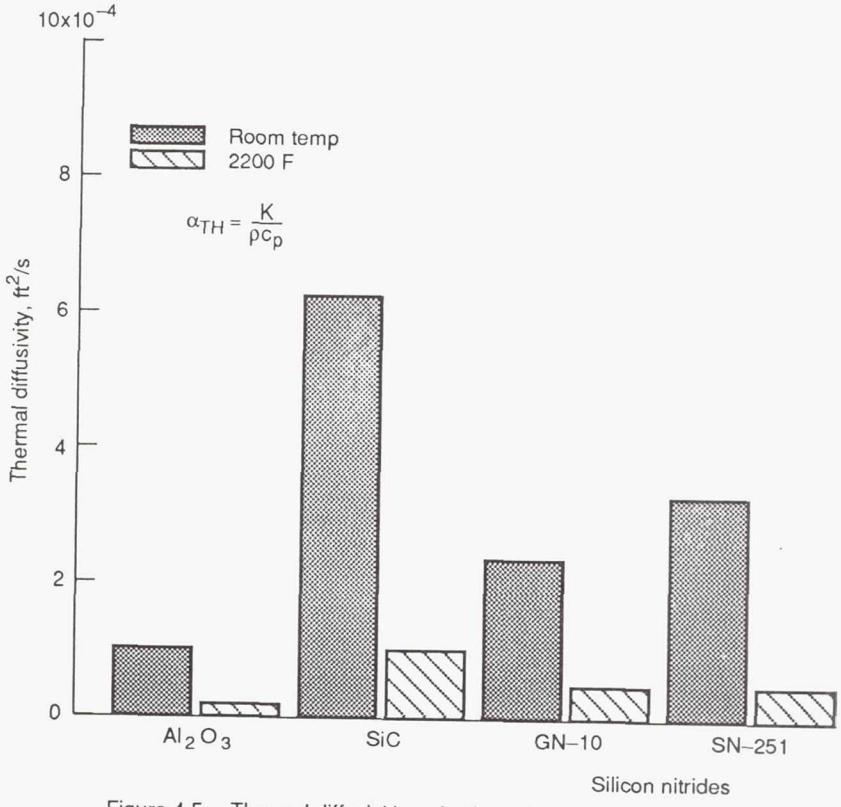

Figure 4.5.—Thermal diffusivities of selected ceramic materials at room temperature and 2200 °F.

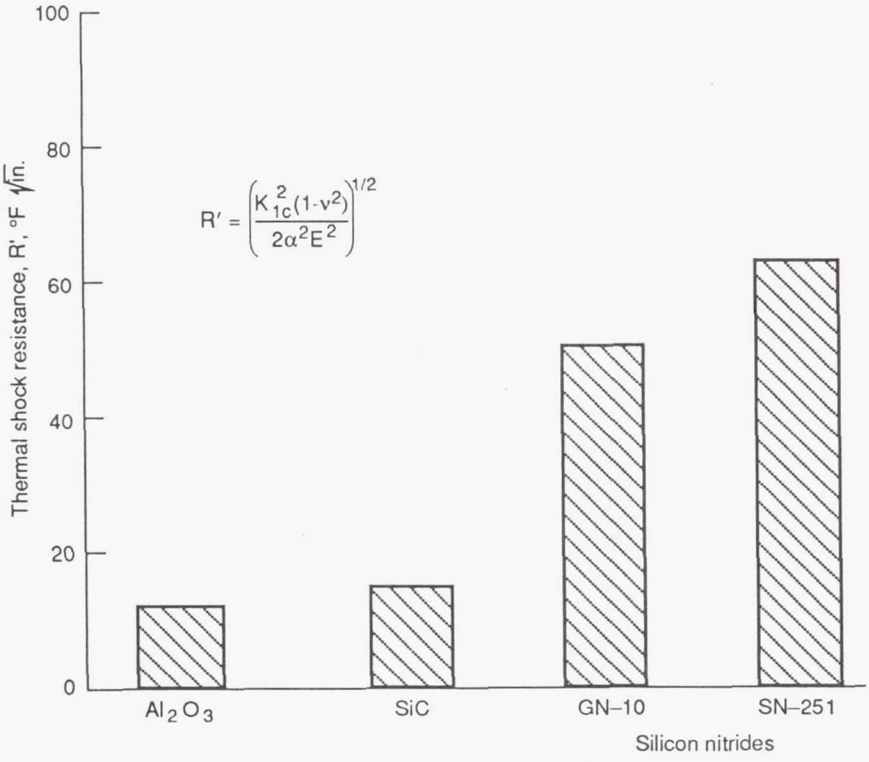

Figure 4.6.—Material resistance to thermal shock induced crack growth.

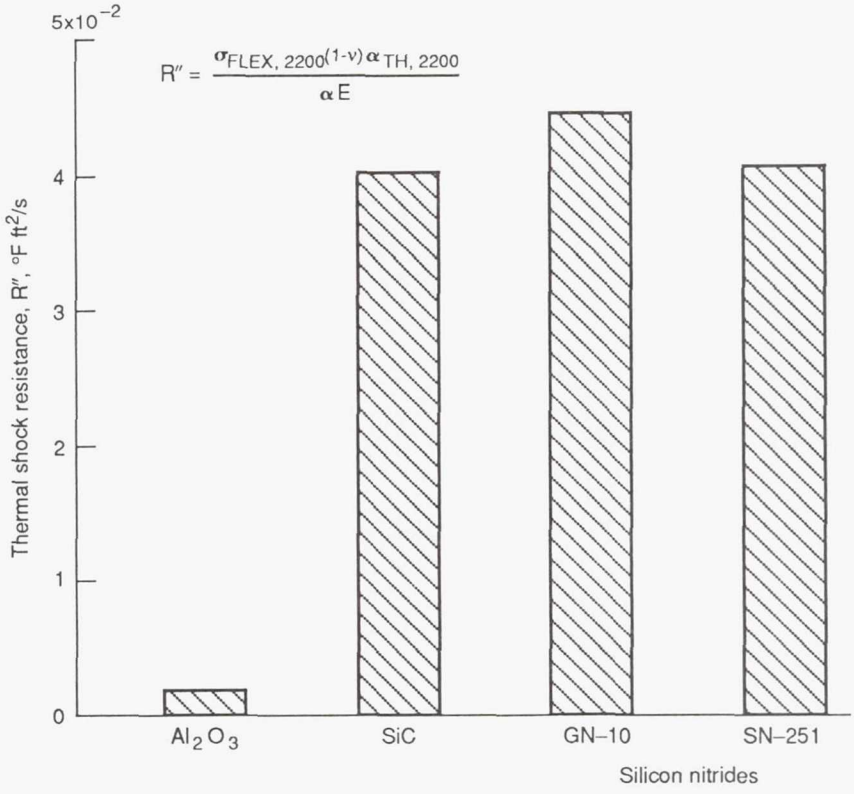

Figure 4.7.—Material resistance to high surface heating rates.

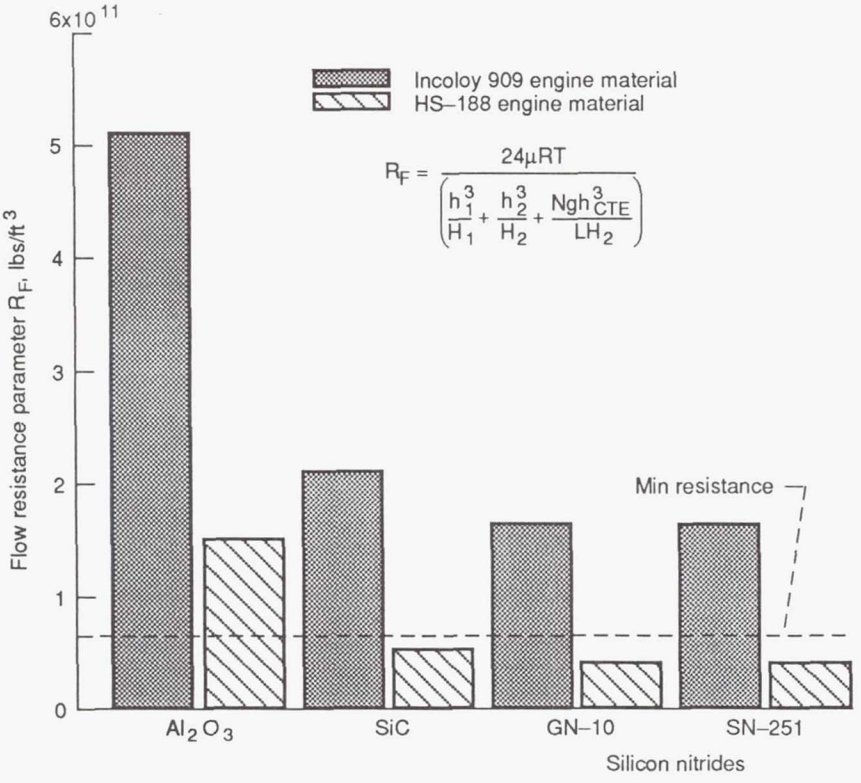

Figure 4.8.—Seal flow resistance parameter for each of the ceramic materials "mounted" in either a high expansion rate (HS–188) or low expansion rate (Incoloy 909) engine panel material.

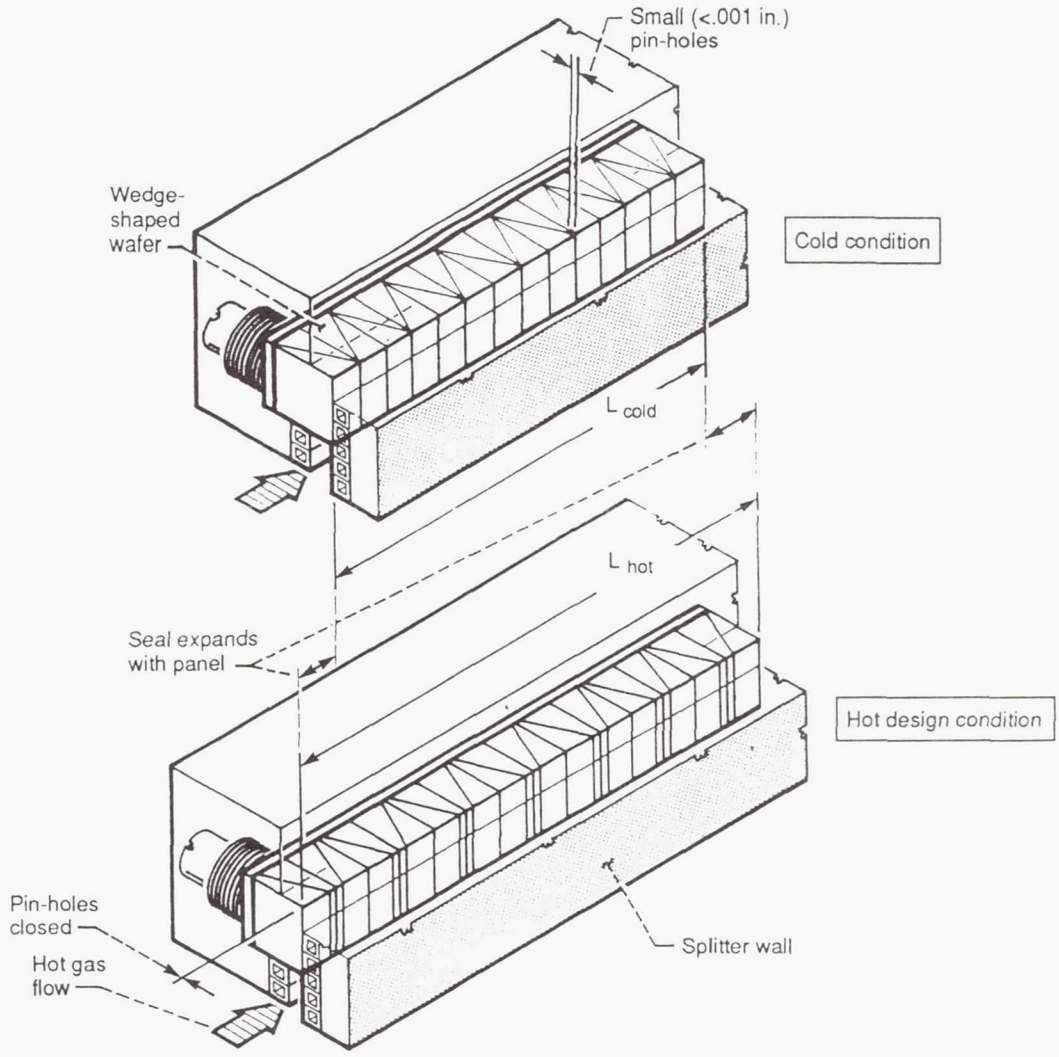

Figure 4.9.—Wedge-shape wafer concept to overcome mismatch in axial thermal expansion rates of the wafer seal and engine materials.

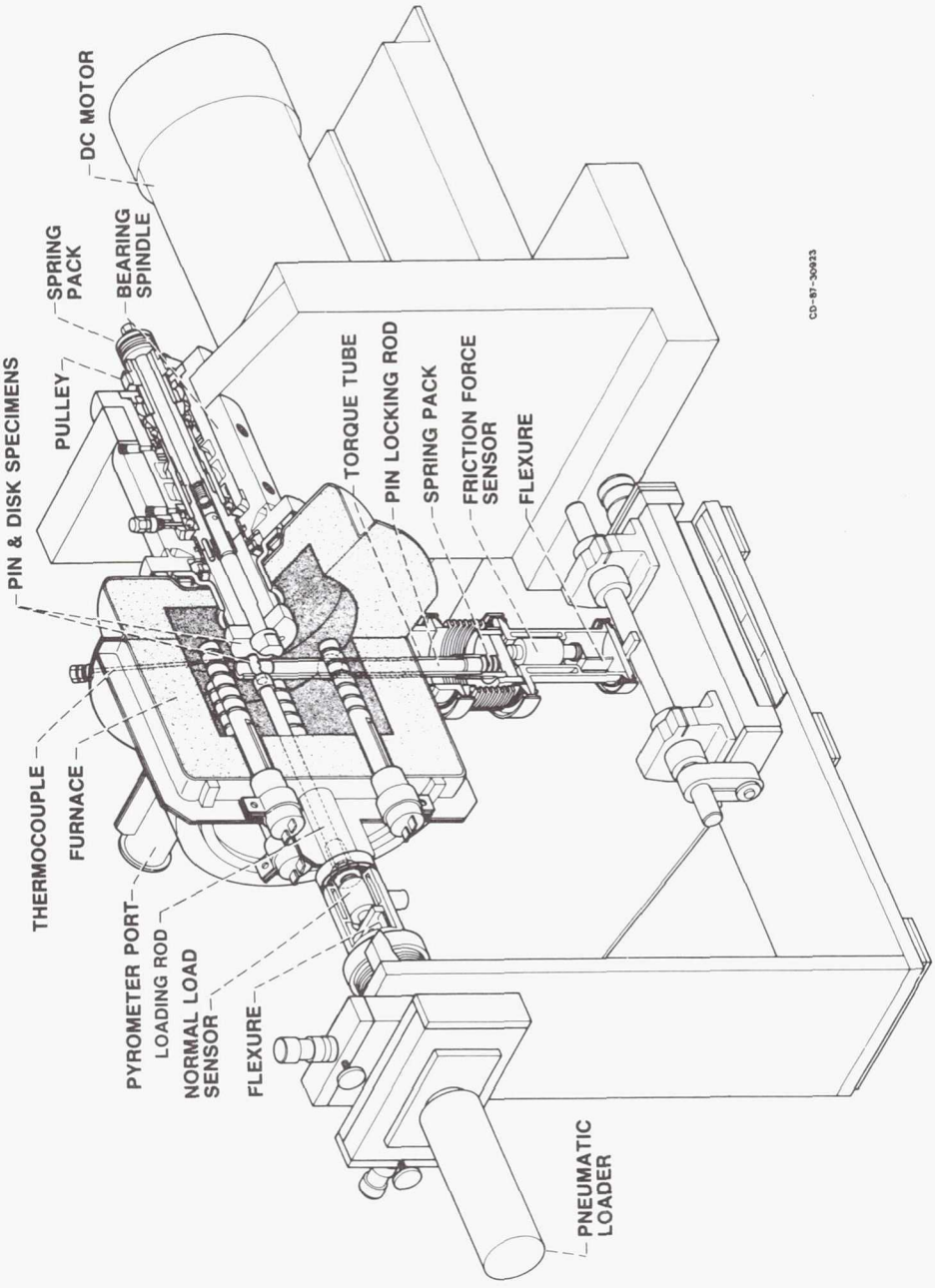

Figure 4.10.—High temperature pin-on-disk tribometer for measuring seal material friction coefficients at temperature.

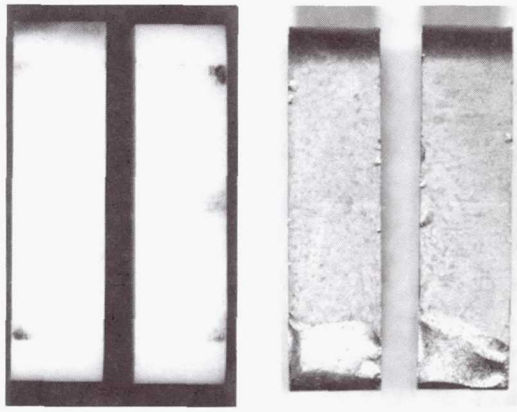

1/8 in.

(a) Aluminum oxide wafers. (b) Silicon carbide wafers.

Figure 4.11.—Photograph of ceramic wafer elements: (a) aluminum oxide wafers after high temperature (1350 °F) testing; (b) silicon carbide wafers with chipped corners after room remperature tests.

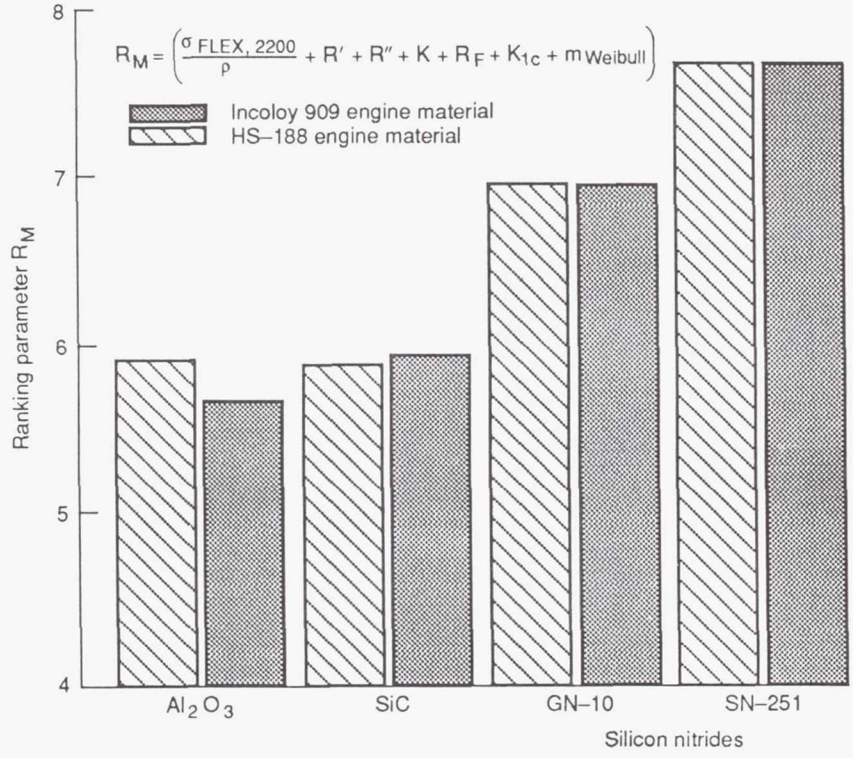

Figure 4.12.—Ceramic wafer material overall ranking.

CHAPTER 5

5. SUMMARY AND RECOMMENDATIONS

In the present research, the performance of a new high temperature ceramic wafer engine seal was examined. The seal shows promise of minimizing the leakage of high temperature, high pressure gases past the movable panels of advanced hypersonic engines. The seal is made of high temperature ceramic wafers that can operate at temperatures up to 2500 °F. The seal's flexibility derived through relative sliding between adjacent wafers can accommodate and seal the significant wall distortions anticipated in the engine splitter walls.

A specially designed test fixture was developed to assess the leakage rates of the ceramic wafer seal as a function of engine simulated pressures, temperatures and adjacent wall conditions. The fixture was fabricated from high temperature Inconel X-750 material to accommodate the required high test temperatures (up to 1500 °F) and pressures (up to 100 psi) without loss of structural integrity. Several important high temperature testing issues were successfully overcome in the implementation of the test rig including accommodation of differences in thermal expansion rates, virtual elimination of parasitic end-leakage of these linear seals, and qualification of

an acceptable high temperature thread antiseize compound. In the case of the mismatch in thermal expansion rates, for instance, design calculations made of a critical heater-to-rig joint avoided a potentially dangerous mismatch in metal expansion rates. Left unchecked these high thermal stresses could have resulted in a potentially dangerous heater pipe failure.

Using the seal fixture, general leakage flow trends were established for the wafer seal. At a constant temperature, leakage rates increased somewhat-parabolically with increasing engine pressure differential. At a constant engine pressure differential, the engine seal leakage rate decreased with increasing temperature for temperatures up to 1000 °F at which point leakage rates began to increase. A leakage flow model developed herein predicted the leakage trends noted for increasing pressure and temperature. The leakage model predicted leakage rates with little or no discrepancy at low and moderate pressures, across the full temperature range considered. Under the combined high engine pressure and high temperature conditions some discrepancies were noted and are believed to have been caused by thermally-induced nonuniform changes in the leakage gap conditions.

Using the flow model developed and the leakage data base collected, one can estimate the leakage flow rates for other gases of interest such as inert helium cooling gas. According to the flow model developed, leakage flow rates for the second gas is estimated by multiplying the measured air leakage rates by the ratio of the gas molecular weights (e.g., MW_2/MW_{air}) and by the ratio of the gas viscosities (e.g., μ_{air}/μ_2).

A material ranking scheme has been developed that allows designers to select between commercially available ceramic seal materials. The method objectively accounts for the many key high temperature material properties to arrive at the best balance of seal properties relative to the seal design criteria. The materials are numerically scored according to their combined high temperature specific flexural strength; high temperature thermal conductivity (providing a measure of the amount of active cooling required); resistance to crack growth; resistance to high heating rates; fracture toughness; Weibull modulus; and finally according to their resistance to leakage flow, where materials having coefficients of thermal expansion closely matching the engine panel material resist leakage flow best. Using the material ranking scheme developed, silicon nitride ceramic has

been shown to be the best monolithic seal material amongst the silicon carbide, silicon nitride, and aluminum oxide ceramics considered.

Based on the research conducted herein, the following specific results were obtained:

1. The feasibility of the ceramic wafer seal to accommodate and seal engine simulated gas and wall conditions has been established.

2. The ceramic wafer seal performed well meeting an industry established leakage-rate limit for all combinations of engine simulated pressures (up to 100 psi), and gas temperatures (up to 1350 °F) sealing well against flat and engine simulated distorted wall conditions where wall distortions were up to 0.15 in. in only an 18 in. span.

3. A seal leakage flow model has been developed based on the theory of externally pressurized gas film bearings and predicts seal leakage flow rates with good agreement for all but the highest combined temperatures and pressures.

4. Of the competing silicon nitrides considered, the Kyocera SN-251 material has the best overall properties assuming the wafer seal is mounted in a low expansion engine material or that the leakage resistance goal can be met using the alternate means described.

Recommendations for Future Work: In this report, baseline concept feasibility has been established. However, prior to costly hypersonic engine tests, it is recommended that the following remaining issues be addressed:

1. Assessment of the seal's sliding seal performance under simulated engine sliding conditions, and the assessment of effects of dust particles of anticipated size on wafer seal performance.

2. Assessment of the seal's high heat flux performance determining survivability under rocket nozzle heating rates.

3. Definition of transient heating and high acoustic (up to 185 dB) effects on the structural integrity of the seal wafers.

4. Definition of seal film-coolant effectiveness under supersonic engine flow conditions with the potential of shock waves impinging and disrupting the coolant boundary layer.

5. Validation of design concepts described herein including: the centrally-purged, dual-seal coolant approach; and the wedge-shaped wafer approach for accommodating axial mismatches in ceramic wafer and metal engine-panel expansion rates.

MASTER REFERENCE LIST

Chapter 1

1.1 "Advanced V/STOL Propulsion Component Development: Nozzle Deflector Final Report," R77AEG441-VOL-1, General Electric, Aug. 1977. (Avail. NTIS, AD-B021511L.)

1.2 Kuchar, A.P., "Variable Convergent-Divergent Exhaust Nozzle Aerodynamics," Aircraft Propulsion Systems Technology and Design, Oates, G.C. editor, American Institute of Aeronautics and Astronautics, Inc., Washington, DC, pp. 301-338 (1989).

1.3 Holowach, J. and Lee, G.D., "Bimetallic Air Seal for Exhaust Nozzles," U.S. Patent 4,813,608 (1989).

1.4 Dursch, H.W., Nedervelt, P.D. Newquist, C.W., and Burns R.A., "National Aerospace Plane (NASP) Airframe Technology Option Five, Sealing Concepts," D180-31720-1, Boeing Advanced Systems, July 21, 1989.

1.5 Steinetz, B.M., DellaCorte, C., Sirocky, P.J., "On The Development of Hypersonic Engine Seals," NASA TP-2854 (1988).

1.6 Tong, M., and Steinetz, B.M., "Thermal and Structural Assessments of a Ceramic Wafer Seal in Hypersonic Engines," NASA TM-103651 (1990).

Chapter 2

2.1 Steinetz, B.M., DellaCorte, C., and Sirocky, P.J., "On The Development of Hypersonic Engine Seals," NASA TP-2854 (1988).

2.2 Boiler and Pressure Vessel Code, Section VIII, Division 1. American Society of Mechanical Engineers (1980).

2.3 Boiler and Pressure Vessel Code, Section VIII, Division 2. American Society of Mechanical Engineers (1980).

2.4 Kattus, J.R., "Inconel X-750," Aerospace Structural Metals Handbook, Metals and Ceramics Information Center, Battelle Labs, Columbus, OH, Vol. 4, Article 4105 (1990).

Chapter 3

3.1 Steinetz, B.M., DellaCorte, C., and Sirocky, P.J., "On The Development of Hypersonic Engine Seals," NASA TP-2854 (1988).

3.2 Steinetz, B.M., "A Test Fixture for Measuring High-Temperature Hypersonic Engine Seal Performance," NASA TM-103658 (1990).

3.3 Steinetz, B.M., DellaCorte, C., and Tong, M., "Seal Concept and Material Performance Evaluation for the NASP Engine," NASA CP-7045, Vol. VI, Structures, pp. 39-58 (1989).

3.4 Tong, M., and Steinetz, B.M., "Thermal and Structural Assessments of a Ceramic Wafer Seal in Hypersonic Engines," NASA TM-103651 (1990).

3.5 White, F, Fluid Mechanics, McGraw-Hill, New York (1979).

3.6 Ausman, J.S., "Gas Lubricated Bearings," Advanced Bearing Technology, NASA SP-38, E.E. Bisson and W.J. Anderson, eds., pp. 109-138 (1964).

3.7 Constantinescu, V.N., Gas Lubrication, American Society of Mechanical Engineers, New York (1969).

3.8 Licht, L., "Extension of the Conducting Sheet Analogy to Externally Pressurized Gas Bearings," Journal of Basic Engineering, vol. 83, no. 2, pp. 209-212 (1961).

Chapter 4

4.1 Steinetz, B.M., DellaCorte, C., and Sirocky, P.J., "On The Development of Hypersonic Engine Seals," NASA TP-2854 (1988).

4.2 Steinetz, B.M., "A Test Fixture for Measuring High-Temperature Hypersonic-Engine Seal Performance," NASA TM-103658 (1990).

4.3 Steinetz, B.M., "High Temperature Performance Evaluation of a Hypersonic Engine Ceramic Wafer Seal," NASA TM-103737 (1991).

4.4 Tong, M., and Steinetz, B.M., "Thermal and Structural Assessments of a Ceramic Wafer Seal in Hypersonic Engines," NASA TM-103651 (1990).

4.5 Richerson, D.W., Modern Ceramic Engineering, Marcel Dekker, New York (1982).

4.6 Hecht, N., "Mechanical Properties Characterization of High Performance Ceramic," 27th Automotive Technology Development Contractors Coordination Meeting, Society of Automotive Engineers (1990). (Also to be published in Ceram. Eng. Sci. Proc., no. 7-8, 1991.)

4.7 Weibull, W., "A Statistical Distribution Function of Wide Applicability," J. Appl. Mech., vol. 18, no. 3, pp. 293-297 (1951).

4.8 Hasselman, D.P.H., "Thermal Stress Resistance Parameters for Brittle Refractory Ceramics: A Compendium," Bull. Am. Ceram. Soc., vol. 49, no. 12, pp. 1033-1037 (1970).

4.9 Chandler, W.T., "Hydrogen-Environment Embrittlement and Its Control in High Pressure Hydrogen/Oxygen Rocket Engines," Advanced Earth-to-Orbit Propulsion Technology Conference, NASA CP-2437-VOL-2, R.J. Richmond and S.T. Wu, eds., pp. 618-634 (1986).

4.10 Incoloy 909 Product Catalog, Publication No. IAI-18, Inco Alloys International, Inc. (1987).

4.11 Sliney, H.E. and DellaCorte, C., "A New Test Machine for Measuring Friction and Wear in Controlled Atmospheres to 1200 °C," NASA TM-102405 (1990).

4.12 Steinetz, B.M., DellaCorte, C., and Tong, M., "Seal Concept and Material Performance Evaluation for the NASP Engine," NASA CP-7045, Vol. VI, Structures, pp. 39-58 (1989).

4.13 Herbell, T.P., Eckel, A.J., Hull, D.R., and Misra, A.K., "Effect of Hydrogen on the Strength and Microstructure of Selected Ceramics," NASA TM-103674 (1990).

4.14 Manson, S.S., "Inconel 718," Aerospace Metals Handbook, Article 4103 (1974). (Also see, Kattus, J.R., "Inconel 718," Aerospace Metals Handbook, Article 4103, 1986.)

REPORT DOCUMENTATION PAGE

Form Approved
OMB No. 0704-0188

1. AGENCY USE ONLY (*Leave blank*)	2. REPORT DATE	3. REPORT TYPE AND DATES COVERED
	February 1992	Technical Memorandum

4. TITLE AND SUBTITLE

Evaluation of an Innovative High Temperature Ceramic Wafer Seal for Hypersonic Engine Applications

5. FUNDING NUMBERS

WU-505-63-5B

6. AUTHOR(S)

Bruce M. Steinetz

7. PERFORMING ORGANIZATION NAME(S) AND ADDRESS(ES)

National Aeronautics and Space Administration
Lewis Research Center
Cleveland, Ohio 44135-3191

8. PERFORMING ORGANIZATION REPORT NUMBER

E-6048

9. SPONSORING/MONITORING AGENCY NAMES(S) AND ADDRESS(ES)

National Aeronautics and Space Administration
Washington, D.C. 20546-0001

10. SPONSORING/MONITORING AGENCY REPORT NUMBER

NASA TM-105556

11. SUPPLEMENTARY NOTES

Report was submitted as a dissertation in partial fulfillment of the requirements for the Degree of Doctor of Philosophy, Case Western Reserve University, Cleveland, Ohio in 1991. Responsible person, Bruce M. Steinetz, (216) 433-3302.

12a. DISTRIBUTION/AVAILABILITY STATEMENT

Unclassified - Unlimited
Subject Category 37

12b. DISTRIBUTION CODE

13. ABSTRACT ***(Maximum 200 words)***

A critical mechanical system in advanced hypersonic engines is the panel-edge seal system that seals gaps between the articulating engine panels and the adjacent engine splitter walls. Significant advancements in seal technology are required to meet the extreme demands placed on the seals, including the simultaneous requirements of low leakage, conformable, high temperature, high pressure, sliding operation. In this investigation, the design, development, analytical and experimental evaluation of a new ceramic wafer seal that shows promise of meeting these demands will be addressed. A high temperature seal test fixture was designed and fabricated to measure static seal leakage performance under engine simulated conditions. Ceramic wafer seal leakage rates are presented for engine-simulated air pressure differentials (up to 100 psi), and temperatures (up to 1350 °F), sealing both flat and distorted wall conditions, where distortions can be as large as 0.15 in. in only an 18 in. span. Seal leakage rates are low, meeting an industry-established tentative leakage limit for all combinations of temperature, pressure and wall conditions considered. A seal leakage model developed from externally-pressurized gas film bearing theory is also presented. Predicted leakage rates agree favorably with the measured data for nearly all combinations of temperature and pressure. Discrepancies noted at high engine pressure and temperature are attributed to thermally-induced, non-uniform changes in the size and shape of the leakage gap condition. The challenging thermal environment the seal must operate in places considerable demands on the seal concept and material selection. Of the many high temperature materials considered in the design, ceramics were the only materials that met the many challenging seal material design requirements. Of the aluminum oxide, silicon carbide, and silicon nitride ceramics considered in the material ranking scheme developed herein, the silicon nitride class of ceramics ranked the highest because of their high temperature strength; resistance to the intense heating rates; resistance to hydrogen damage; and good structural properties. Baseline seal feasibility has been established through the research conducted in this investigation. Recommendations for future work are also discussed.

14. SUBJECT TERMS

Seal; High temperature; Leakage modelling; Ceramic; Hypersonic engine; Design; Testing; Pressure; Ramjet; Scramjet

15. NUMBER OF PAGES

194

16. PRICE CODE

A09

17. SECURITY CLASSIFICATION OF REPORT	18. SECURITY CLASSIFICATION OF THIS PAGE	19. SECURITY CLASSIFICATION OF ABSTRACT	20. LIMITATION OF ABSTRACT
Unclassified	Unclassified	Unclassified	